Development of high β^*-optics for ALICE

Pascal Dominik Hermes

-Masterarbeit-

Westfälische Wilhelms-Universität Münster

Institut für Kernphysik

April 2013

Contents

Abstract

This thesis describes a feasibility study for a special optical configuration in Insertion Region 2 (IR2) of the Large Hadron Collider (LHC), which is host of the ALICE detector. This configuration allows the study of elastic and diffractive scattering during LHC high-intensity proton operation, in parallel to the nominal physics studies in all LHC experiments at the design energy of $7\,\mathrm{TeV}$ per beam. Such measurements require the installation of additional Roman Pot (RP) detectors in the very forward region, at longitudinal distances of $150\,\mathrm{m}$ to $220\,\mathrm{m}$ from the Interaction Point (IP). Apart from being adjusted for a specific betatron phase advance between the IP and the RP detectors, such a configuration must be optimized for the largest possible β^*-value, to be sensitive for the smallest possible four-momentum transfer $|t|$. A value of $\beta^* = 18\,\mathrm{m}$ is compatible with a bunch spacing of $25\,\mathrm{ns}$, considering the LHC design emittance of $\epsilon_N = 3.75\,\mu\mathrm{m\,rad}$, and a required bunch-bunch separation of $12\,\sigma$ at the parasitic bunch encounters. An optical configuration with $\beta^* = 18\,\mathrm{m}$ and a matched betatron phase advance between IP and RP ($\Delta\psi_{x,y} = 0.34$) has been calculated. The optics are studied for their compatibility with the constraints imposed by the LHC. A crossing angle of $\theta_C = 300\,\mu\mathrm{rad}$ is matched for the optical configuration. The adjustment of the IP-RP phase advances leads to a significant reduction of the phase advance across the IR, so external compensation methods must be applied. In high-intensity operation of the LHC, the phase advance compensation must be applied between IP1 and IP5. However, detailed strategies on these compensations must still be worked out. The detector acceptance for scattered protons is calculated, based on different assumptions for the measurement parameters. The 50% acceptance threshold for the measurement of elastic events is moved from $|t|_{50\%} = 13\,\mathrm{GeV}^2$ with the nominal ALICE optics, to a value of $|t|_{50\%} = 0.44\,\mathrm{GeV}^2$ with the matched $\beta^* = 18\,\mathrm{m}$ optics. The most optimistic boundary conditions lead to an acceptance threshold of $|t|_{50\%} = 0.24\,\mathrm{GeV}^2$, whereas the most pessimistic scenario leads to $|t|_{50\%} = 0.78\,\mathrm{GeV}^2$. Remaining studies are outlined, and scenarios with different beam conditions are discussed.

1. Introduction

Already the presocratic philosophers asked questions about the constituents of matter and the origin of the world. Today, more than 2500 years later, natural sciences have achieved a huge improvement in our understanding of the universe and on the elementary particles and their interactions. Particle accelerators and the ensuing analysis of the collision data have been a very important tool in these achievements.

Despite the huge amount of information which was collected in the last century, there are still many unanswered questions in elementary particle physics. The Large Hadron Collider (LHC) at CERN[1], close to Geneva (Switzerland) was built to enhance our understanding of the creation and constitution of the universe, and of the elementary interactions of matter.

After the start-up in 2009, the LHC was operating and producing particle collisions in four Insertion Regions (IR). In April of 2012, the energy in proton operation increased to $4\,\mathrm{TeV}$ per beam, corresponding to more than $50\,\%$ of the design energy, and surpassing the largest energy reached at the former highest energy accelerator Tevatron by a factor of approximately four [CER12, Fer09]. The beam energy is intended to be further increased after an upgrade phase (Long Shutdown 1, LS1), scheduled for 2013-2015 [For12].

The LHC has a large flexibility in terms of its energy range and the type of the accelerated particles. Besides the nominal high-intensity proton operation, the machine has been used to perform heavy-ion and asymmetric proton-lead collisions [ALI13].

In the high-intensity proton collision scheme with the largest possible number of bunches, the particle beams are squeezed to $\beta^* = 0.55\,\mathrm{m}$ in the Interaction Points (IP) of the ATLAS and CMS experiments (the β^*-value is proportional to the square of the beam size at the IP).

On the other hand, dedicated optical configurations with very large β^*-values of up to $\beta^* = 1000\,\mathrm{m}$ have been implemented in these two regions, for the study of elastic scattering and diffractive events [B$^+$12b]. The study of these processes requires the measurement of very forward scattered particles with special particle detectors, which are installed at longitudinal distances of 150-240 m from the corresponding IP.

---

[1]Conceil Européen pour la Recherche Nucléaire (European Organization for Nuclear Research).

Besides the large β^*-values, such configurations obey specific constraints on the betatron phase advance[2] and require a reduced number of circulating bunches (156 instead of 2808) [BW10]. Since priority is given to high-luminosity operation, the time available for these measurements is very limited and totals only some days per year [CER11].

The performance of ALICE during proton operation is not depending on high collision rates, because the Time Projection Chamber in the ALICE central barrel is a comparably slow detector, due to the long drift time of the ionization charge [Mor01]. Therefore, ALICE could have the chance to implement an optical configuration with high β^*-value, under the premise of compatibility to the high-intensity mode of the LHC, with a bunch spacing of 25 ns (2808 bunches per beam). This would allow the tagging of very forward protons[3] over very long periods of time, in parallel to the nominal physics studies in the remaining LHC experiments, and without performance loss for the regular ALICE physics program.

In the diffractive interactions, central systems of particles with low transverse momentum are produced by the fusion of two or more Pomerons [D$^+$02]. ALICE is particularly suited for the detection of such central systems, thanks to the detector layout in the central barrel with the low p_T-threshold and the good particle identification capability. If very forward detectors were installed in the region around ALICE, and if the beam optics in IR2 would be optimized for the very forward measurements, coincidence measurements of the forward particles and the centrally produced systems could be realized. Additional physics topics which could be studied are the identification of diffractive topologies, the search for the odderon, the study of central production of non-q$\bar{\text{q}}$ states, Bose-Einstein correlations and small-x-Gluon behaviour [HS13].

This thesis describes the development and evaluation of an optical configuration in the region around ALICE, which combines the measurability of very forward particles with the compatibility to high-intensity operation in the remaining LHC collision points. Chapter 2 describes the theoretical background on particle accelerator physics. The LHC with its different Insertion Regions, in particular IR2 hosting the ALICE detector, is elaborated in Chapter 3. The following Chapter 4 provides further information on diffractive physics and soft-QCD which is the main interest of a high β^*-configuration. After this, the details of the optics development are outlined and the proposed optical configurations are analyzed (Chapter 5). In Chapter 6, acceptance simulations with the given optics are discussed for different scenarios. Chapter 7 presents an outlook, and the final section summarizes the thesis.

---

[2]The phase of the transverse quasi-harmonic betatron oscillations which particles perform because of the magnetic fields in a particle accelerator.

[3]Very forward means here, that the detection can not take place within the cavern of the ALICE detector.

2. Particle Accelerator Physics

Introduction

The history of particle accelerators reaches back to the 30s of the 20th century [Kul01]. Since that time, a large number of accelerators has been designed and used. Nowadays, the highest beam energy can be reached by synchrotron accelerators which synchronously ramp the magnet currents and the beam energy. Examples for such synchrotron accelerators are Tevatron, HERA, LEP and LHC. The objective of this chapter is the introduction and discussion of some aspects of modern synchrotron physics.

2.1 Transverse Particle Dynamics of Single Particles

2.1.1 Coordinate System

Every particle accelerator has an ideal trajectory which is usually situated in the centre of the vacuum pipes and magnets (there is, however, an exception in the regions around the Interaction Points, where two beams move in a common beam pipe, see Chap. 3.4.3). It is useful to introduce an accelerator specific coordinate system for the mathematical treatment of transverse beam dynamics, schematically illustrated in Fig. 2.1. An ideal particle moves exactly along the ideal trajectory having the design momentum p. The longitudinal position of the ideal particle is described by the value s, indicating the integrated path with respect to a defined starting point [Hin08]. The transverse position of a real particle is represented by its deviation from the reference trajectory, while the origin of the coordinate system is moving with s. A priori, the transverse particle movement is symmetric with respect to x and y and can therefore be described by a generalized transverse coordinate $u = x, y$. This allows a general description of the transverse particle dynamics which is valid for both directions. Eventual asymmetries can be taken into account by the parameters which describe the magnet configuration.
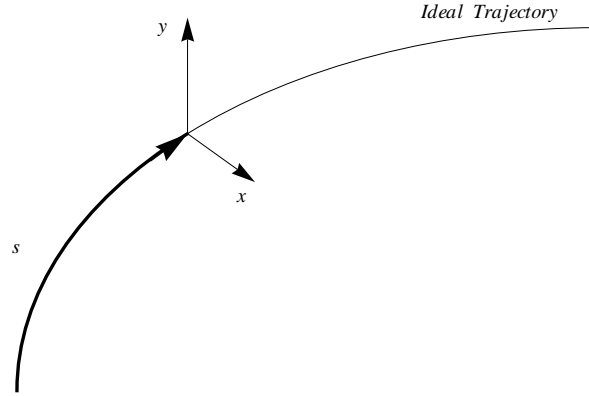
Figure 2.1: Coordinate system for mathematical treatment of transverse beam dynamics. The origin of the transverse axes moves with the longitudinal variable s. Figure based on [Hin08].

Apart from the transverse position, there is a particular interest in the transverse momentum, in order to be able to characterize the particle in phase space. The normalized transverse momentum is the derivative of u with respect to s

$$u'(s) = \frac{\mathrm{d}u}{\mathrm{d}s} \,. \tag{2.1}$$

A full set of parameters specifying the particle position in transverse phase space is

$$\mathbf{p_T}(s) = (x(s), x'(s), y(s), y'(s))^T \,. \tag{2.2}$$

2.1.2   Magnets

The particle beams in a storage ring[1] can circulate for several hours. It is therefore essential to have focusing elements in the machine, in order to keep the beam dimensions small and to avoid collisions with the vacuum pipes or magnets. Furthermore, the configuration of the focusing elements should be optimized for the intended measurement. Apart from the focusing elements, bending elements must be used, in order to keep the particle beams on a circular trajectory.

In principle, bending and focusing can be achieved by using either electric or magnetic fields. The Lorentz force, acting on a particle of charge q, moving with velocity $\mathbf{v}$, in presence of a magnetic field $\mathbf{B}$ and electric field $\mathbf{E}$, is described by the equation [GM10]

$$\mathbf{F} = q\left(\mathbf{E} + \mathbf{v} \times \mathbf{B}\right) \,. \tag{2.3}$$

---

[1]A storage ring is a circular accelerator which accelerates and stores particle beams to finally bring them into collision or to inject them into another machine.

In a high energy machine like the LHC, the stored particles are highly relativistic (protons at the LHC injection energy have $\gamma = 479.6$ [B$^+$04]). The absolute value v of the velocity will therefore be very close to c. Since **v** is in cross product with **B** but not with **E**, the force on a particle in a magnetic field of $1\,$T corresponds to an electric field of approximately $300\,$MV/m. Magnetic fields in this order of magnitude are much easier to create than the corresponding electric field, so magnetic fields should be used whenever it is possible. For bending and focusing, dipole and quadrupole magnets are used, respectively. Higher order magnets (sextupoles, octupoles,...) are used as well, e.g. for chromaticity corrections, but are not subject of this thesis.

Dipole Magnets

Particle accelerators are usually built in the horizontal plane and the bending forces are therefore purely horizontal [Tur95]. The magnetic dipole field is applied in vertical direction and should be as homogeneous as possible. In the LHC, the reachable energy is limited by the largest strength of the superconducting dipole magnets. By equalizing the centrifugal force and the Lorentz force, the following relation can be deduced [Wie99]

$$B\,\rho = \frac{p}{q}\,, \qquad\qquad (2.4)$$

where ρ denotes the bending radius of a particle with momentum p and charge q in the magnetic field B. If the particle momentum is increased, the required magnetic field for a given bending radius rises linearly. The quantity $B\,\rho$ is the so-called magnetic rigidity. To make the magnet configurations comparable at different momenta, it is useful to consider the magnetic field, normalized by the momentum-to-charge ratio [Wie99]

$$\frac{1}{\rho} = \frac{B}{p/q}, \qquad\qquad [\rho^{-1}] = \mathrm{m}^{-1}\,. \qquad\qquad (2.5)$$

Since the bending is purely horizontal, the transverse bending radius can be described by

$$\frac{1}{\rho_u} = \begin{cases} \frac{1}{\rho_x} & \text{for } u = x \\ 0 & \text{for } u = y \end{cases}, \qquad\qquad (2.6)$$

which takes into account the horizontal arrangement of the accelerator.

Quadrupole Magnets

For the focusing of charged particle beams, an element with lens-like behavior is aimed. Particles with large deviations from the ideal trajectory should be in a larger magnetic field than those with small amplitudes. The magnetic field should be orthogonal and linearly rising with u [Hin08]

$$B_y = g\,x\,, \qquad B_x = g\,y\,, \tag{2.7}$$

where g is the magnetic gradient. This property can be obtained by a magnetic quadrupole (see Fig. 2.2). It can be characterized by the magnetic gradient g and the effective length L. The effective length takes into account the fringe fields of the magnet and is therefore larger than the geometrical length. Similar to the previously introduced normalized dipole field, the magnetic gradient can be normalized by p/q, in order to be able to compare quadrupole gradients at different particle momenta [Wie99]

$$k = \frac{g}{p/q}\,, \qquad\qquad [k] = \mathrm{m}^{-2}\,. \tag{2.8}$$

As shown in Fig. 2.2, the quadrupole magnet is always focusing in one and defocussing in the other transverse direction. Effective focusing in both transverse directions can be reached by an arrangement of multiple quadrupoles (see Chap. 2.3).
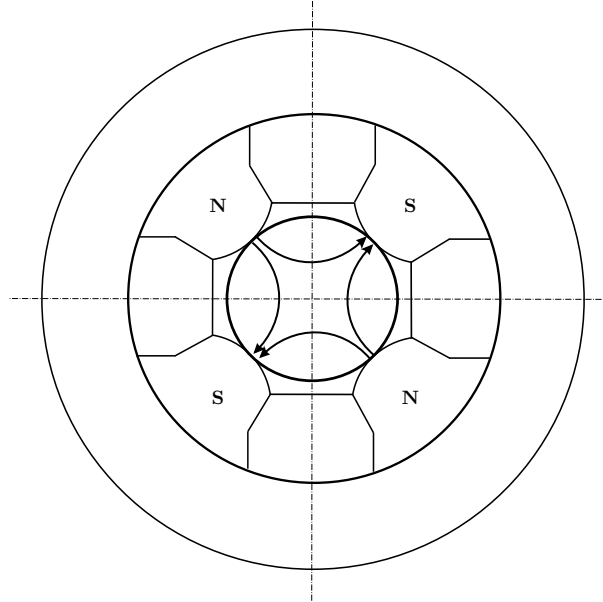

Figure 2.2: Transverse profile of a quadrupole magnet with magnetic field lines [Hin08].

2.1.3 Equation of Motion

The expansion of the magnetic field of a dipole and of a quadrupole in a Taylor's series leads to the equation of motion in the approximation of very small u, which is given by (a detailed derivation can be found in [Hin08, Tur95, Wie99])

$$u'' - \left(k_u(s) - \frac{1}{\rho_u^2(s)} \right) u = -\frac{1}{\rho_u(s)}\, \xi \,, \tag{2.9}$$

where $\xi = \frac{p - p_p}{p} = \frac{\Delta p}{p}$ is the relative deviation[2] of the particle momentum p_p from the design momentum p. Eq. 2.9 is a non-homogeneous differential equation of second order. Solving this equation requires first a solution of the homogeneous equation. Therefore, a particle with ideal momentum is considered ($\xi = 0$). Using the substitution $K_u(s) = \left(k_u(s) - \frac{1}{\rho_u^2(s)} \right)$ finally leads to the simple homogeneous equation [Tur95]

$$u'' - K_u(s)\, u = 0 \,. \tag{2.10}$$

Obviously, K_u is a periodic function with the period C (circumference of the machine)

$$K_u(s) = K_u(s + C) \,. \tag{2.11}$$

Thus, Eq. 2.10 is of the type of Hill's differential equation [Hin08]. It can be solved by using Floquet's theorem. A detailed approach for the solution of the Hill equation can be found in [Wie99]. One way of denoting the general solution in terms of u and the slope u' is

$$u\,(s) = C_u(s)\, u_0 + S_u(s)\, u_0' \,, \tag{2.12}$$

$$u'(s) = C_u'(s)\, u_0 + S_u'(s)\, u_0' \,, \tag{2.13}$$

where u_0 and u_0' are the initial conditions. For convenience, this can be expressed in terms of a matrix-vector product

$$\begin{pmatrix} u\,(s) \\ u'(s) \end{pmatrix} = \begin{pmatrix} C_u\,(s) & S_u\,(s) \\ C_u'(s) & S_u'(s) \end{pmatrix} \begin{pmatrix} u_0 \\ u_0' \end{pmatrix} = \mathcal{M}_u(s)\, \mathbf{u_0} \,. \tag{2.14}$$

Thus, the transformation of the initial $\mathbf{u}(s_0) = (u_0, u_0')^T$ vector can be described by a transfer matrix $\mathcal{M}_u(s)$, only depending on type and strength of the magnetic element between s_0 and s. The matrix elements $C_u(s)$ and $S_u(s)$ represent cosine and sine-like functions, respectively.

---

[2]Compared to the literature [Hin08, Wie99], this definition is unusual. However, within the framework of this thesis, this definition is used, because the dispersion functions calculated by MAD-X are negative with respect to the usual definition (see Chap. 2.1.6 and [MADb]).

A general way of expressing C and S, is for the case of $K_u > 0$ (the absolute values in this case are only shown for convenience) [Hin08]

$$C_u(s) = \cos \ \left(\sqrt{|K_u|} \, s \right) \qquad S_u \, (s) = \frac{1}{\sqrt{|K_u|}} \, \sin \ \left(\sqrt{|K_u|} \, s \right) \,, \tag{2.15}$$

and for the case of $K_u < 0$

$$C_u(s) = \cosh \left(\sqrt{|K_u|} \, s \right) \qquad S_u \, (s) = \frac{1}{\sqrt{|K_u|}} \, \sinh \left(\sqrt{|K_u|} \, s \right) \,. \tag{2.16}$$

The corresponding quantities for $C'_u(s)$ and $S'_u(s)$ can be obtained by deriving the expressions given in Eq. 2.15 and Eq. 2.16 [Hin08]. If the transformation of the $\mathbf{u}_0$ vector by n magnets and/or drift spaces is considered, the total transfer matrix is the product of the transfer matrices of the individual elements in between s_0 and s [Wie99]

$$\mathcal{M}_u^{\mathrm{tot}} = \mathcal{M}_u^n \cdot \mathcal{M}_u^{n-1} \cdots \mathcal{M}_u^2 \cdot \mathcal{M}_u^1 \,. \tag{2.17}$$

2.1.4   Betatron Motion

Another way of expressing the general solution to Hill's equation is [Wie99]

$$u(s) = a_u \, \sqrt{\beta_u(s)} \, \cos \left(2 \, \pi (\psi_u(s) + \phi_u) \right) \,, \tag{2.18}$$

where a_u and ϕ_u are integration constants. Here, the equation for $u(s)$ describes a quasi-harmonic oscillation, modulated by a position dependent function $\sqrt{\beta_u(s)}$ with an amplitude defined by a_u, which is a constant for each individual particle in both transverse planes. The position-dependent quantities $\psi_u(s)$ and $\beta_u(s)$ are coupled by the integral [Hin08]

$$\psi_u(s) = \frac{1}{2 \, \pi} \int_0^s \frac{\mathrm{d}\tilde{s}}{\beta_u(\tilde{s})} \,. \tag{2.19}$$

$\psi_u(s)$ is a relative quantity which is defined with respect to a starting position $s_0 = 0$. The quasi-harmonic oscillation around the reference orbit is called betatron oscillation with betatron phase ψ_u. The wavenumber of these oscillations changes with s. Corresponding to Eq. 2.19, the local oscillation wavenumber at the position s is the inverse of $\beta_u(s)$

$$2 \, \pi \frac{\mathrm{d}\psi_u(s)}{\mathrm{d}s} = \frac{1}{\beta_u(s)} \,. \tag{2.20}$$

$\beta_u(s)$ is the central function in the description of transverse beam dynamics, and is called the betatron function. It varies with s and depends on the magnetic elements in the accelerator. By deriving u in Eq. 2.18, it can be shown that [Wie99]

$$a_u^2 = \gamma_u u^2 + 2\alpha_u u u' + \beta_u u'^2 \,. \tag{2.21}$$

This expression is the parametric definition of an ellipse with surface $\pi \, a_u^2$, which is known as the Courant-Snyder Invariant.

The shape and the orientation of this ellipse are defined by the so-called Twiss parameters, which are pure functions of the magnet configuration [Tur95]

$$\beta_u(s), \qquad \alpha_u(s) = -\frac{1}{2}\frac{\partial\beta_u(s)}{\partial s}, \qquad \gamma_u(s) = \frac{1+\alpha_u^2(s)}{\beta_u(s)}. \tag{2.22}$$

A physical interpretation of Eq. 2.21 is that at the position s, the accessible points of the particle in phase space u, u' lie on the border of an ellipse, defined by the Twiss parameters and a_u. For every turn through the circular machine, the particle's position on the border of this ellipse is different and depends on the betatron phase advance over one full turn. Following Eq. 2.18, the largest amplitude in u is obtained if the cosine equals 1, thus

$$u_{\max}(s) = a_u\,\sqrt{\beta_u(s)}. \tag{2.23}$$

In the same way, the largest possible slope is given by

$$u'_{\max}(s) = a_u\,\sqrt{\gamma_u(s)}. \tag{2.24}$$

The basic quantities are now derived. For simplicity, the index u will not be used any more from now on. However, all of the following considerations are still valid for both transverse directions. The matrix in Eq. 2.14 can also be deduced inversely, if the initial Twiss parameters $\beta_0, \alpha_0, \gamma_0$, the final parameters β, α, γ and the betatron phase advance $\Delta\psi = \psi - \psi_0$ between the concerning positions are known. Using the general solution to Hill's equation, the initial conditions for $C(s)$ and $S(s)$ and the definition $\varphi = 2\pi\psi$, the transfer matrix is deduced to [Hin08]

$$\mathcal{M} = \begin{pmatrix} \sqrt{\frac{\beta}{\beta_0}}\,(\cos\Delta\varphi + \alpha_0\,\sin\Delta\varphi) & \sqrt{\beta_0\,\beta}\,\sin\Delta\varphi \\ \frac{\alpha-\alpha_0}{\sqrt{\beta\,\beta_0}}\cos\Delta\varphi - \frac{1+\alpha\,\alpha_0}{\sqrt{\beta\,\beta_0}}\sin\Delta\varphi & \sqrt{\frac{\beta_0}{\beta}}\,(\cos\Delta\varphi - \alpha\,\sin\Delta\varphi) \end{pmatrix}. \tag{2.25}$$

Since the ellipse of accessible u, u' states is transformed as well, it is of particular interest how this transformation can be quantified. It can be shown that the transfer matrix $\tilde{\mathcal{M}}$ for the $(\beta, \alpha, \gamma)^T$ vector of the Twiss parameters is in a simple relation with the matrix elements of the matrix $\mathcal{M}$ for the transformation in phase space [Tur95]

$$\begin{pmatrix} \beta(s) \\ \alpha(s) \\ \gamma(s) \end{pmatrix} = \begin{pmatrix} C^2 & -2\,S\,C & S^2 \\ -C\,C' & S\,C' + S'\,C & -S\,S' \\ C'^2 & -2\,S'\,C' & S'^2 \end{pmatrix} \begin{pmatrix} \beta(s_0) \\ \alpha(s_0) \\ \gamma(s_0) \end{pmatrix} = \tilde{\mathcal{M}}\,(\beta(s_0), \alpha(s_0), \gamma(s_0))^T. \tag{2.26}$$

2.1.5   Betatron Tune

In circular accelerators, the variable Q denotes the number of betatron oscillations which are performed by a particle that moves once along the whole ring of circumference C [Hin08]

$$Q = \frac{1}{2\pi} \int_{s}^{s+C} \frac{\mathrm{d}\tilde{s}}{\beta(\tilde{s})} \,. \tag{2.27}$$

The stability of the beams strongly depends on the value of the tune. Since magnet misalignments are unavoidable in a real machine, it is essential to design the machine configuration in such a way that the tune does not coincide with a resonance. Resonances occur, for example, if the tune is an integer (first order resonance), half integer (second order resonance), and so on. Furthermore, there are coupling resonances which forbid to choose $Q_x = Q_y$ in first order. The resonance conditions, summarizing the tunes which have to be avoided, are given by [Wie99]

$$p = n\,Q_u \,, \tag{2.28}$$
$$p = l\,Q_x + m\,Q_y \,,$$

where $p, l, m, n \in \mathbb{Z}$, and $|l| + |m| = n$ is the order of the resonance. All resonance conditions can be graphically represented in a tune diagram where the fractional parts q_x and q_y of the tune are represented on the two axes. Such a tune diagram up to the order of 7 is shown in Fig. 2.3.
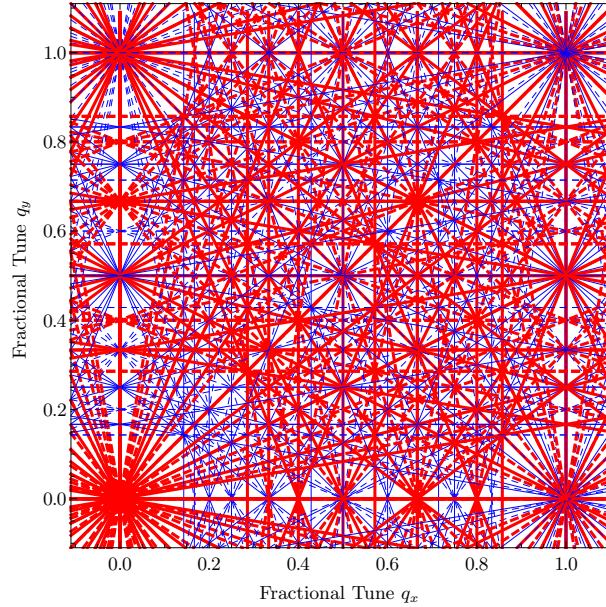

Figure 2.3: Tune diagram up to 7th order [Fit12]. Only the fractional part of the tune is shown.

In the LHC, resonances up to 12th order must be considered, so the accessible ranges for the tune are very narrow. The tune, used for both beams in the LHC (at collision) is [B$^+$04]

$$Q_x = 59.31 \,, \qquad Q_y = 64.32 \,. \tag{2.29}$$

These values have to be kept constant, even if the magnet configuration is locally changed. If the phase advance over one part of the ring is modified, the difference in phase will have to be compensated in other parts of the machine.

2.1.6 Periodic Dispersion

The general solution of the equation of motion is the sum of the solution of the homogeneous part and one particular solution of the inhomogeneous equation [Wie99]

$$u(s) = u_h(s) + u_i(s) \,. \tag{2.30}$$

The following particular solution of the inhomogeneous equation can be deduced [Hin08]

$$u_i(s) = \eta(s)\,\xi \,, \tag{2.31}$$

where $\xi = \frac{p - p_p}{p}$ is the relative momentum deviation from the design momentum. The function $\eta(s)$ is periodic with period C, and is referred to as the periodic dispersion function

$$\eta(s) = \eta(s + C) \,. \tag{2.32}$$

Like the Twiss parameters, the periodic dispersion is a function of the machine configuration. The physical meaning of Eq. 2.31 is that particles with non-zero momentum deviation have an additional amplitude which is proportional to the relative momentum deviation ξ and the value of the dispersion function. At a given position s, the periodic dispersion is a function of $\beta(s)$, the bending elements and β-functions in the entire machine, and of the machine tune [Hin08]

$$\eta(s) = -\frac{\sqrt{\beta(s)}}{2\sin(\pi Q)} \int_s^{s+C} \frac{\sqrt{\beta(\tilde{s})}}{\rho(\tilde{s})} \cos\left[2\pi\left(\psi(\tilde{s}) - \psi(s) - \frac{Q}{2}\right)\right] d\tilde{s} \,. \tag{2.33}$$

Besides the definition of the periodic dispersion function, Eq. 2.33 elegantly describes the first order tune constraint $(Q \neq n)$, since the denominator goes to zero for integer tunes. Later-on, the local dispersion is introduced, occurring if formerly ideal particles lose momentum in consequence of a particle interaction at the IP (see Chap. 4.2.1).

2.2   Transverse Dynamics of Particle Beams

In a real accelerator, the beams consist of a large number of particles. From that fact, a lot of new physics arises, compared to a single particle description. The following chapter, however, concentrates on the aspects which are important for the high β^*-optics development.

2.2.1   Transverse Emittance

In the description of a particle beam, one very important parameter is the transverse beam size at any given position s. The particle density in transverse phase space is (in an idealized model) a Gaussian for both, u and u', as shown in Fig. 2.4. Since the Twiss parameters are defined by the machine configuration, the orientation of the phase ellipses with the accessible states are the same for all particles. The only individual parameter for every particle is a, which is related to the area of the individual phase space ellipse. Furthermore, Eq. 2.23 shows that the largest possible amplitude of $u(s)$, for a given machine configuration at a fixed position s, is a pure function of a. To determine the beam size, the root mean square a_{RMS} can be considered. The square of this quantity is defined as the RMS emittance of the particle beam [Tur95].

$$\epsilon = \langle a \rangle_{\mathrm{RMS}}^2 \,. \tag{2.34}$$

In consequence, for one transverse direction, the RMS beam size of the particle beam is
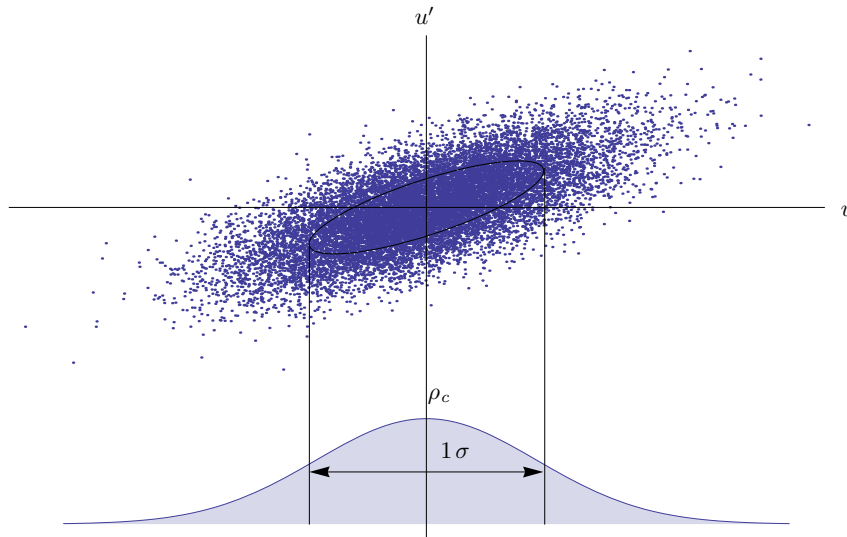
$$\sigma(s) = \sqrt{\epsilon\,\beta(s)} \,. \tag{2.35}$$

Figure 2.4: Schematic illustration of the particle distribution in phase space with the $1\,\sigma$ ellipse. The particle density can be described by a Gaussian for either of the canonical coordinates.

In the framework of the description by Hill's equation, a is a constant for every particle, so $a_{\mathrm{RMS}}^2 = \epsilon$ is not changing while the beam moves in the machine (Liouville's Theorem), if the acting forces are purely conservative [Hin08]. However, there are non-conservative effects which change the beam emittance. Examples for such processes are intra-beam scattering, beam-beam interaction or synchrotron radiation [Wie99]. A drastic change of the emittance occurs during the ramp of a beam. While ramping, the emittance shrinks as $\beta\gamma$ rises (relativistic β-value and Lorentz factor γ), so ϵ is a momentum dependent quantity. In order to be able to compare emittances at different beam energies, the normalized emittance is defined as [Hin08]

$$\epsilon_N = \beta\,\gamma\,\epsilon\,. \tag{2.36}$$

Since the beam size is directly related to $\sqrt{\epsilon}$, the available aperture in the vacuum pipes, in terms of the beam size σ, is much larger top energy than at injection energy.

2.2.2 Beam Size

Also the longitudinal particle density can be described by a Gaussian. The RMS-value of the squared relative momentum spread is defined by [B$^+$04]

$$\langle \delta^2 \rangle = \left\langle \left(\frac{p - p_p}{p} \right)^2 \right\rangle_{\mathrm{RMS}}, \tag{2.37}$$

where p is the ideal momentum and p_p is the momentum of the individual particle. Thus, the total RMS beam size is given by [Hin08]

$$\sigma(s) = \sqrt{\epsilon\,\beta(s) + \eta^2(s)\,\langle \delta^2 \rangle}\,, \tag{2.38}$$

where $\eta(s)$ is the periodic dispersion function at the position s.

2.3   Beam Optics

The matrix formalism, describing transformations of the $(u, u')^T$ vector, is similar to the formalism of ray transfer matrices, used for the description of photon beams in presence of lenses [Trä07]. The magnet configuration in an accelerator is therefore referred to as an optical configuration. In the following, a general description is given for the transformation of the $(u, u')^T$ vector, but once the transfer matrix $\mathcal{M}$ is known, the generalization to the transfer matrix $\tilde{\mathcal{M}}$ of the Twiss vector $(\beta, \alpha, \gamma)^T$ can easily be done by means of Eq. 2.26.

2.3.1   Drift Spaces

The most simple case for a transfer matrix is obtained for the drift space with $k = \rho^{-1} = 0$, so if there are no magnetic forces acting at all [Wie99]

$$\mathcal{M}_{\text{drift}} = \begin{pmatrix} 1 & d \\ 0 & 1 \end{pmatrix} . \tag{2.39}$$

Particles in a drift space just move linearly, while keeping the initial divergence. The betatron function is proportional to the square of the RMS beam size, so the evolution of the β-function in a drift space is a parabolic function with respect to s (see Chap. 2.3.4).

2.3.2   Quadrupoles in Thin Lens Approximation

A focal length f can be assigned to a quadrupole of effective length L and strength k [Hin08]

$$f = (k\,L)^{-1} . \tag{2.40}$$

If the focal length of the quadrupole is much larger than the effective length, the matrix in Eq. 2.14, defined by Eq. 2.15 and Eq. 2.16 can be approximated by the simple form [Hin08]

$$\mathcal{M}_{\text{Q}} = \begin{pmatrix} 1 & 0 \\ \frac{1}{f} & 1 \end{pmatrix} . \tag{2.41}$$

This is the transfer matrix of a thin lens in geometrical optics [Trä07]. The focal length in horizontal direction is the negative of the focal length in vertical direction and vice versa

$$f_x = -f_y . \tag{2.42}$$

If $f < 0$, the quadrupole is focusing in the respective plane, if $f > 0$ it is defocusing. The thin lens approximation allows the analysis of different arrangements of quadrupoles in a very simple way. It is used in the following for the calculation of different quadrupole lattices.

2.3.3 FODO Lattice

The FODO lattice is a periodic arrangement of focusing and defocusing quadrupoles, used for the transport of particle beams, while maintaining the transverse beam dimensions small. Considering quadrupoles of focal length $\pm f$, placed at a distance d from each other, the total transfer matrix for one period, starting at the centre of a focusing quadrupole, is given by [Tur95]

$$\mathcal{M}_{\text{FODO}} = \begin{pmatrix} 1 & 0 \\ -\frac{1}{2f} & 1 \end{pmatrix} \begin{pmatrix} 1 & d \\ 0 & 1 \end{pmatrix} \begin{pmatrix} 1 & 0 \\ \frac{1}{f} & 1 \end{pmatrix} \begin{pmatrix} 1 & d \\ 0 & 1 \end{pmatrix} \begin{pmatrix} 1 & 0 \\ -\frac{1}{2f} & 1 \end{pmatrix}. \tag{2.43}$$

If $u'_0 = 0$, the transformation by the matrix $\mathcal{M}_{\text{FODO}}$ leads to a periodically modulated $(u, u')^T$ vector with period $2\,d$. Corresponding to this, a particle beam which is matched to $\alpha = 0$ at the centre of the first FODO quadrupole, will have an oscillating β-function with the same period . The betatron phase advance per period $\Delta\psi_p$ can be deduced to [Hin08]

$$\Delta\psi_p = \frac{1}{\pi}\,\sin^{-1}\left[\pm\frac{d}{2\,f}\right]. \tag{2.44}$$

The β-functions of a matched beam for some FODO periods of the LHC arcs are shown in Fig. 2.5. The magnetic elements of the LHC beam line are shown on top of the figure. In the following, representations of beam parameters are shown with the beam line layout on top, to facilitate the assignment of the quantity to the magnetic elements in the machine. The blue and red boxes indicate focusing and defocusing quadrupoles, respectively.
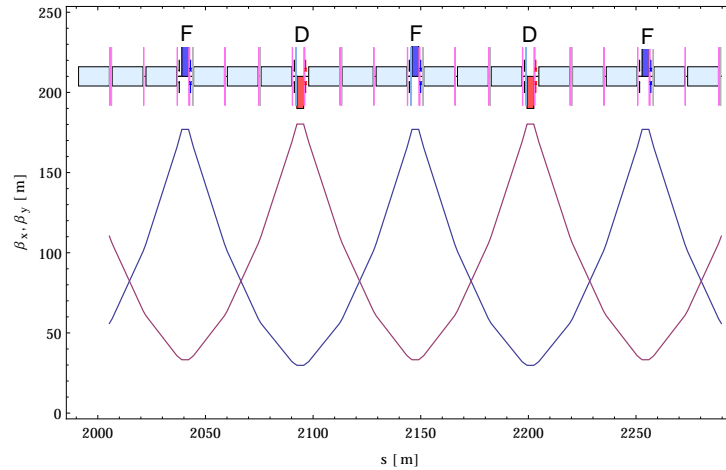

Figure 2.5: Betatron functions in the FODO cells of the LHC arcs (blue for horizontal, red for vertical). The quadrupoles which are focusing/defocusing in x-direction are labeled with F and D, respectively. Two successive quadrupoles are separated by three cells of bending dipoles.

2.3.4   Quadrupole Triplet and β^*-Value

The particle beams are squeezed at the Interaction Point, in order to have the same beam size in both transverse directions. Focusing in both directions can be achieved by means of a quadrupole triplet. The triplet consists of three quadrupoles, where two successive magnets are placed at a distance d from each other. The negative focal length f_c of the quadrupole in the centre is approximately half of the focal length f_o of the outer quadrupoles [Wie99]

$$f = f_o \approx -2\,f_c\,. \tag{2.45}$$

The resulting transfer matrices are different in the two planes x and y

$$\mathcal{M}_{x/y} = \begin{pmatrix} 1 - 2\frac{d^2}{f^2} & 2\,d\left(1+\frac{d}{f}\right) \\ -2\frac{d}{f^2}\left(1-\frac{d}{f}\right) & 1 - 2\frac{d^2}{f^2} \end{pmatrix}, \quad \mathcal{M}_{y/x} = \begin{pmatrix} 1 - 2\frac{d^2}{f^2} & 2\,d\left(1-\frac{d}{f}\right) \\ -2\frac{d}{f^2}\left(1+\frac{d}{f}\right) & 1 - 2\frac{d^2}{f^2} \end{pmatrix}. \tag{2.46}$$

However, in the approximation of large focal lengths $d \ll f$, these two matrices become identical. Both can be expressed as a matrix of a single thin lens, with a focal length of [Hin08]

$$f_{x/y} = \frac{f+d}{2}\,. \tag{2.47}$$

Ideally, the beam dimensions after the triplet should reach a minimum at the Interaction Point, thus $\alpha^* = 0$ (parameters at the collision point are denoted by a * in superscript). Starting at the beam waist, the transition to any point before the triplet is described by the matrix of a drift space (see Eq. 2.39). If $\alpha^* = 0$, the β-function at any position s is given by [Hin08]

$$\beta(s) = \beta^* + \frac{(s-s^*)^2}{\beta^*}\,, \tag{2.48}$$

describing a parabola with minimum at s^*, which is shown for different β^*-values in Fig. 2.6. Besides the β^*-value, the beam divergence at the collision point is of particular interest. The general expression for the divergence is given in Eq. 2.24

$$u'_{\mathrm{RMS}} = \sqrt{\epsilon}\,\sqrt{\gamma}\,, \tag{2.49}$$

which is in the special situation of $\alpha^* = 0$

$$u'_{\mathrm{RMS}}(s^*) = \sqrt{\frac{\epsilon}{\beta^*}}\,. \tag{2.50}$$

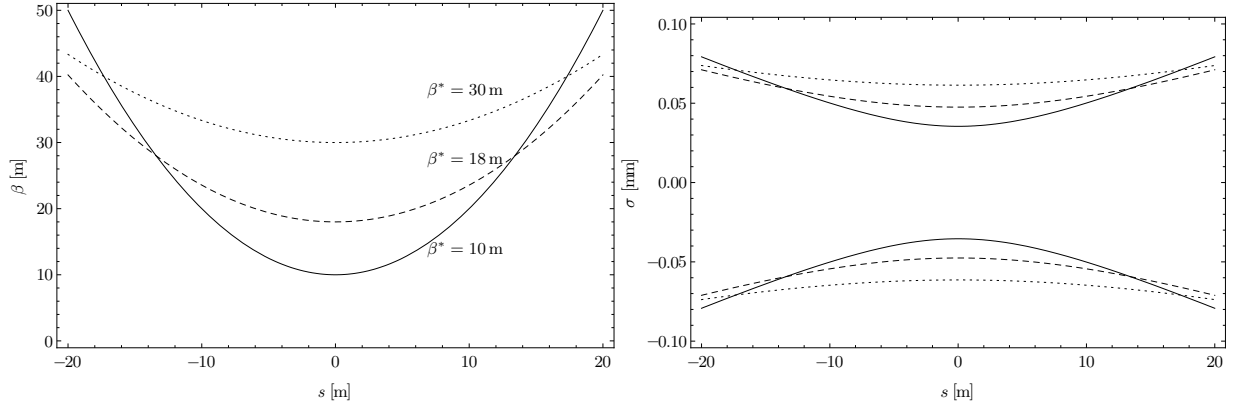This means that the divergence at the collision point decreases as $\sqrt{\beta^*}$ rises.

Figure 2.6: Left: β-functions around a beam waist for different β^*-values. Right: Beam dimensions around a beam waist for different β^*-values ($\epsilon_N = 3.75\,\mu\text{m}\,\text{rad}$ at $7\,\text{TeV}$, no dispersion).

2.4 Phase Space Matching

The actual machine configuration is determined by $k(s)$ and $\rho(s)$, while the lengths of the drift spaces and the magnetic elements are fixed with the configuration of the accelerator. Every machine configuration possesses specific eigenfunctions of the Twiss transfer matrix $\tilde{\mathcal{M}}$ of either a specific section or the entire machine [Hin08]. Colliders like the LHC have different regions with experiments or functional units (Insertion Regions, IRs) which are separated by the regions with periodic FODO lattices (see Chap. 3.2). At every transition between two successive sections (1) and (2), the optical functions $\alpha, \beta, \eta, \eta'$ must be matched [Wie99]

$$(\alpha, \beta, \eta, \eta')_{(1)} = (\alpha, \beta, \eta, \eta')_{(2)}. \tag{2.51}$$

If the local optical configuration is changed in one region, the optical functions at the end of the region must be matched to the requirements of the following section [Wie99]. Mismatched optics in a part of a circular accelerator will negatively affect the betatron functions in the whole machine.

2.5   Beam-Beam Effects

2.5.1   Crossing Angle

In the collision regions, where the two counter-rotating beams share a common vacuum pipe, the bunched particle beams usually have more than one potential bunch encounter. Besides the Interaction Point, where two bunches should meet, there are many parasitic bunch encounters, where interactions could take place. If the beams are not supposed to collide at all, for example when a beam is stored or ramped, the two beams are fully separated by a separation bump (see Chap. 3.4.3). To bring the beams into collision, the separation bump is switched off [B$^+$04].

However, in the collision mode, the two beams must still have a sufficiently large separation at every potential encounter except at the Interaction Point, in order to avoid secondary collisions and strong beam-beam perturbations. Such secondary interactions can be avoided if a crossing angle is applied [Cha99] (see Fig. 2.7 and Fig. 2.8). The separation at the parasitic bunch-bunch encounters depends on the bunch spacing and on the crossing angle of the two beams.

Due to the crossing and separation schemes, the actual orbit of the two beams is not in the centre of the magnets. The orbit is characterized by the transverse positions x and y of the beam centre in the transverse coordinate system. The angle which is enclosed by the ideal trajectory (which is defined by the magnets) and the axis through the beam pipe centre at the IP location is defined as $\theta_C/2$. The full crossing angle is the angle between the ideal orbits of the two beams, so θ_C if the two beam orbits are symmetric [Cha99].
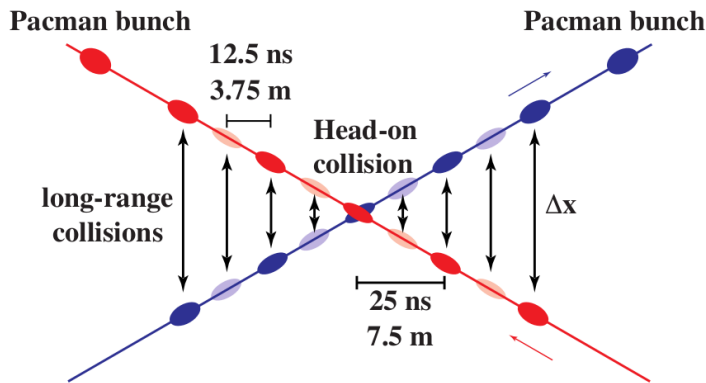

Figure 2.7: Bunch structure of two colliding beams with parasitic encounters. The separation Δx depends on the bunch spacing and on the crossing angle θ_C. Graphics taken from [B$^+$12a].

$(1\sigma_x, 1\sigma_y, 1\sigma_t)$ envelope for $\epsilon_x = 5.02646 \times 10^{-10}$m, $\epsilon_y = 5.02646 \times 10^{-10}$m, $\sigma_p = 0.000111$
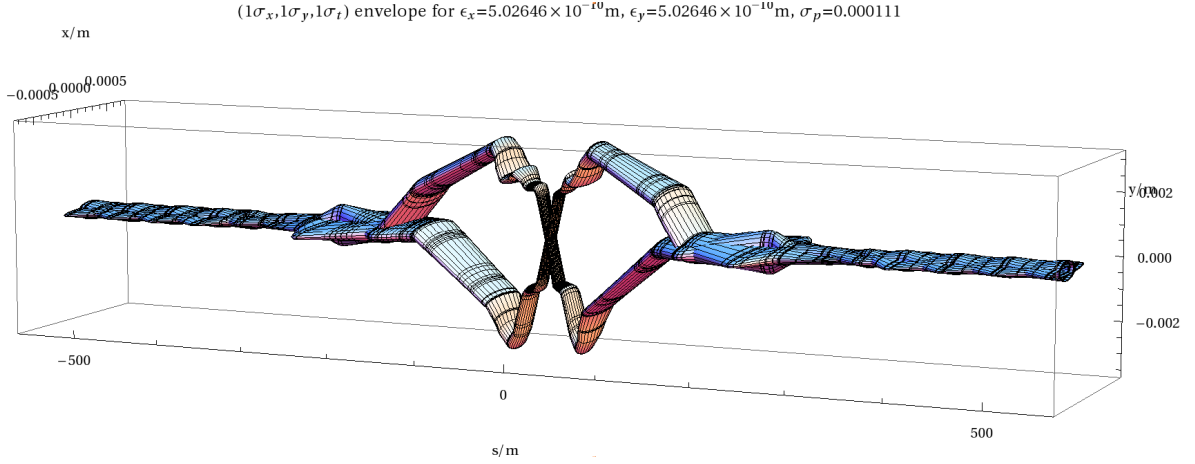
Figure 2.8: Three dimensional $1\,\sigma$ beam envelopes in collision mode at IR2 of the LHC.

2.5.2 Long-Range Beam-Beam Interaction

One of the most limiting factors for luminosity (see Chap. 2.6) is the beam-beam interaction [CAS06]. The dense particle bunches are carrying large amounts of electric charge. In the regions of a particle accelerator where two counter-rotating beams share a common vacuum pipe, these bunches interact while passing by each other. At every bunch encounter, the electromagnetic force acts on the other bunch and gives a radial kick, which leads to a tune change of the corresponding particles [CAS06]. For very large separations, this tune shift can be quantified by means of the so-called long range beam-beam tune shift parameter [Cha99]

$$(\xi_x^{bb}, \xi_y^{bb}) = \frac{1}{2\,\pi} \frac{Z\,N\,r_0}{\gamma} \frac{(\beta_x^*, -\beta_y^*)\,((\Delta x)^2 - (\Delta y)^2)}{((\Delta x)^2 + (\Delta y)^2)^2} \,, \tag{2.52}$$

where Z is the charge of the particles, N is the number of particles per bunch, r_0 is the classical proton radius, γ is the Lorentz factor, β_u^* is the betatron function at the collision point, and Δx and Δy are the separations in the two respective planes. The long range beam-beam tune shift parameter can be used to quantify the strength of the beam-beam interaction, and to compare different machine configurations or accelerators. A simple criterion for adequate separation is that the beam-beam separation at the first parasitic encounter is larger than $5.5\,\sigma$ to $7\,\sigma$ and the tune shift parameter is smaller than $10^{-3} - 10^{-4}$ [Cha99]. However, this criterion is not exclusive and not respecting all aspects of the interaction (e.g. nonlinearities).

2.6   Luminosity

The two most important quality factors for a collider are the top energy and the luminosity. The latter is a quantitative approach to the number of interactions per time, which take place if a certain beam configuration is applied. In particular, the luminosity $\mathcal{L}$ (in units of $\mathrm{cm}^{-2}\,\mathrm{s}^{-1}$) is related to the average number of interactions per time unit by [Hin08]

$$\frac{\mathrm{d}N_i}{\mathrm{d}t} = \mathcal{L}\,\sigma\,, \tag{2.53}$$

where σ is the cross section for the respective interaction. For frontal collisions ($\theta_C = 0$) of round beams ($\beta^* = \beta_x^* = \beta_y^*$, and $\epsilon = \epsilon_x = \epsilon_y$), the luminosity is given by the expression [Cha99]

$$\mathcal{L}_0 = f\,k_b\,\frac{N_1\,N_2}{4\,\pi\,\epsilon\,\beta^*}\,, \tag{2.54}$$

where f is the revolution frequency of the particles, N_1 and N_2 are the number of particles per bunch in Beam 1 and Beam 2, respectively, k_b is the number of bunches circulating in the machine, ϵ is the emittance and β^* is the betatron function at the collision point. A crossing angle reduces the luminosity, because the collisions are not frontal in this case. The total luminosity is then the product of the expression in Eq. 2.54 with a correction factor F_C

$$\mathcal{L} = \mathcal{L}_0\,F_C\,, \tag{2.55}$$

where the correction factor is a function of the crossing angle θ_C, the transverse RMS beam size $\sigma^* = \sigma_x^* = \sigma_y^*$ and the longitudinal RMS beam size σ_l [Hel10]

$$F_C = \frac{1}{\sqrt{1 + \left(\frac{\sigma^*}{\sigma_l}\tan\frac{\theta_C}{2}\right)}} \cdot \frac{1}{\sqrt{1 + \left(\frac{\sigma_l}{\sigma^*}\tan\frac{\theta_C}{2}\right)}}\,. \tag{2.56}$$

For very small angles θ_C and $\sigma^* \ll \sigma_l$, the expression in Eq. 2.56 can be approximated by

$$F_C \approx \frac{1}{1 + \left(\frac{\sigma_l}{\sigma^*}\frac{\theta_C}{2}\right)^2}\,. \tag{2.57}$$

2.7 MAD - Methodical Accelerator Design

2.7.1 MAD-X

MAD (Methodical Accelerator Design) is an accelerator code which is developed at CERN since 1983 [MADa]. The current version, which is used for the calculations in this thesis, is MAD-X. The software allows the optics design and evaluation for various types of particle accelerators. The definitions of the accelerator sequence with specification on the different magnetic and non-magnetic elements can be loaded from external files. Such sequence files are available at the CERN servers for every machine of the CERN accelerator complex (see Chap. 3.1). A specific strength is assigned to every magnet in the sequence. Also, the strength values for the individual configurations which are regularly used in the LHC, are available on the CERN servers. After loading one strength file, the individual magnet strengths can be changed by loading a second strength file or by using the interactive shell. This allows modifying the magnet configuration in one region, while the unvaried optical configuration in the rest of the machine is used.

One very important tool for the optics development is the matching module. This module allows to find the corresponding magnetic strengths which are needed to fulfill defined constraints of the optical configuration. The matching is carried out numerically, by means of different selectable algorithms. The result depends on the number of variables, on the allowed ranges of the variables, and on the number and type of boundary conditions. For each matching, MAD-X calculates a penalty function which is the sum of the square of all the deviations from the quantities under constraint [MADa].

If the user provides a strength and a sequence file, the MAD Twiss module can calculate different beam parameters, such as the α, β, γ-functions, but also the beam orbit positions in horizontal and vertical direction x and y. Furthermore, specific functions of the beam parameters can be defined and calculated. Apart from this, the machine aperture with known tolerances can be loaded, which allows the calculation of n_1 (see Chap. 3.7). The output of a Twiss calculation is usually saved in an external file which can be loaded by other software. MAD provides a plotting module for the creation of postscript files with plots of the desired quantities in a specific region. A user's guide with the different functions can be found in [MADb].

2.7.2 Madtomma

Due to the history of the MAD development and because of the complexity of the LHC machine, the use of MAD-X is quite unhandy and the post-processing of the obtained data requires external software. An integrated environment for Wolfram Mathematica is developed by John M. Jowett and others to use MAD-X within Mathematica, and to read in files from external Twiss calculations [Jow97]. The software is a collection of packages which are under permanent development and can be modified by the user. The framework of Mathematica allows the user to automate the creation of MAD files and to follow up with an automated data analysis of the output. Furthermore, the graphical tools in Mathematica can be used to visualize the beam parameters. Most of the figures in this thesis, which show the evolution of beam parameters over a specific region, have been produced by means of Madtomma. In particular, the possibility to show a schematic drawing of the beam line in the region of interest is used for many figures.

3. The Large Hadron Collider

Introduction

The Large Hadron Collider (LHC) is the world's largest and most powerful particle accelerator, providing energies that have never been reached by any man-made accelerator before. The LHC is a circular proton-proton (pp) and heavy-ion (Pb-Pb) collider with a circumference of 26.7 km, designed for a centre of mass energy of $\sqrt{s} = Z{\cdot}14\,\text{TeV}$[1] [B$^+$04]. The collider was built at the CERN research centre for nuclear physics, close to Geneva/Switzerland. For the installation, the tunnel of the former Large Electron Positron Collider (LEP) was used, which is located at a depth of 50-150 m underground [Bac89]. At the end of 2009, the LHC outreached the until then highest proton energy of 1.05 TeV per beam, reached by the Tevatron collider at the Fermi National Accelerator Laboratory in the USA [CER09]. As yet, the highest centre-of-mass energy the LHC has reached is $\sqrt{s} = Z{\cdot}8\,\text{TeV}$ [CER12]. In 2012, until the end of pp operation before Long Shutdown 1 (LS1), the LHC delivered an integrated luminosity of 23.3 fb^{-1} to the experiments. During the first 4 years of data taking at the LHC, many new observations could be made, including the discovery of the new $\chi_b(3P)$ state [ATL11] and the observation a formely unknown boson with a mass of approximately 125 GeV/c^2, which could be the long sought Higgs particle [ATL12].

3.1 The CERN Accelerator Complex

The LHC is installed at the end of a complex injector chain, where the particle beams are accelerated to the LHC injection energy of 450 GeV [B$^+$04]. Apart from the LHC, other experiments and accelerators are served by the pre-injectors, e.g. the antiproton decelerator (AD), the isotope online detector (ISOLDE), and many more. In its entirety, the network of accelerators at CERN is referred to as the CERN accelerator complex. The whole complex (status end of 2012) is schematically illustrated in Fig. 3.1.
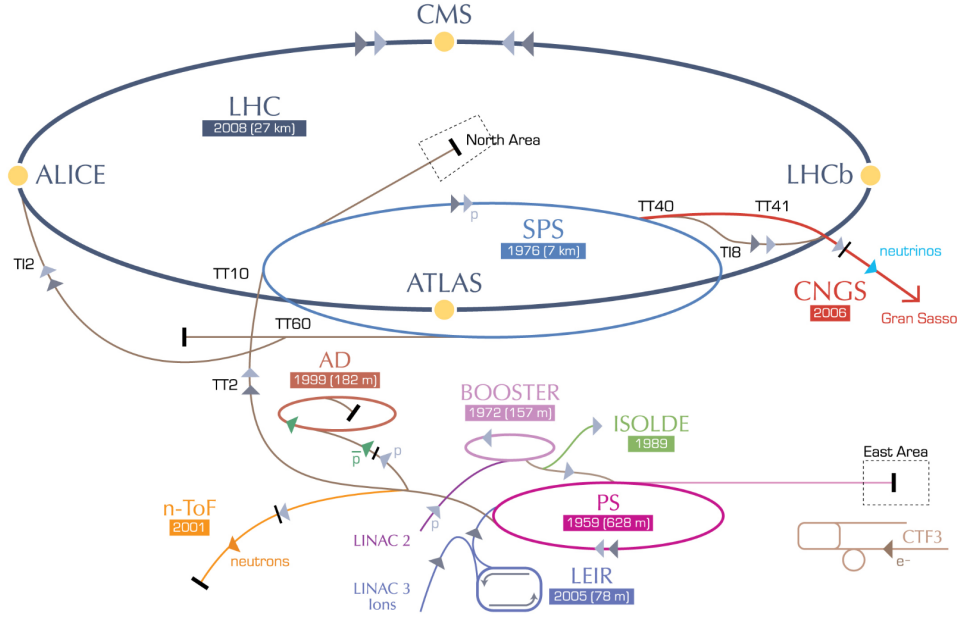
---

[1] Z indicates the ion charge.

Figure 3.1: The CERN accelerator complex [Lef08].

In proton operation, the beams start with a hydrogen source, connected to a linear accelerator (LINAC2), which accelerates the protons to a kinetic energy of 50 MeV. This is the injection energy of the Proton Synchrotron Booster (PSB) which increases the kinetic energy up to 1.4 GeV. After this, the protons are injected into the Proton Synchrotron (PS), where they are accelerated to 26 GeV. From the PS, the particles are injected into the Super Proton Synchrotron (SPS) which provides the acceleration to the LHC injection energy of 450 GeV.

Heavy-ions are initially accelerated to a kinetic energy of $Z \cdot 4.2$ MeV inside LINAC3. Then, the ions are injected into the Low Energy Ion Ring (LEIR) to reduce the beam emittance by electron cooling [LM93]. Once injected into the PS, the way to the LHC is the same as for protons.

3.2   LHC Layout

In the LHC, the two hadron beams move in distinct beam pipes in opposite directions (Beam 1 clockwise, Beam 2 counterclockwise). The particles are kept on a circular trajectory by 1232 superconducting dipole magnets which are operated at a temperature of 1.9 K and creating a magnetic field of up to 8.3 T [B$^+$04]. 474 quadrupole magnets, operated at either 1.9 K or 4.5 K (depending on the magnet type), are used for the beam focusing. Reaching the LHC design energies requires a pressure of less than 10^{-9} mbar inside the vacuum pipes [AW12].
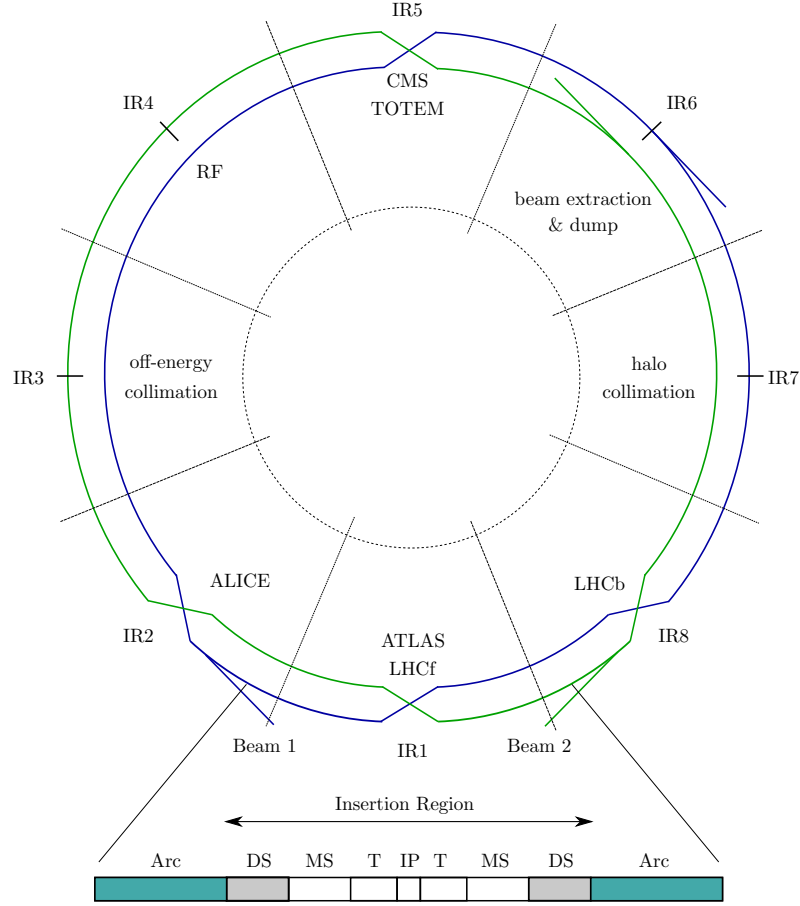
Figure 3.2: LHC and Insertion Region layout (based on [B$^+$12a] and [B$^+$04]).

The machine is divided into 8 octants, containing the Insertion Regions (IR), which host the different experiments and functional units [B$^+$12a]. The experimental IRs itself can be subdivided into different regions, depending on the functionality of the respective quadrupoles. From outer to inner, these regions are the dispersion suppressor (DS) region, a matching section (MS), a focusing triplet (T) section, and the magnet-free collision point region (IP), see Chap. 3.3 and Fig. 3.2. The inner part of the IR (starting from the MS) does not contain bending magnets, so the beam pipes are straight in these regions (this section is called Long Straight Section, LSS). Close to the four collision points of the LHC, both beam pipes are fused to a common vacuum pipe, so the beams can be brought into collision (see Fig. 3.4). Two successive IRs are separated by an arc, containing the bending dipoles and a periodic FODO lattice of quadrupoles [B$^+$12a]. The injection of the particle beams from the SPS into the LHC takes place at IR2 for Beam 1 and at IR8 for Beam 2 [B$^+$04].

3.3   Insertion Regions
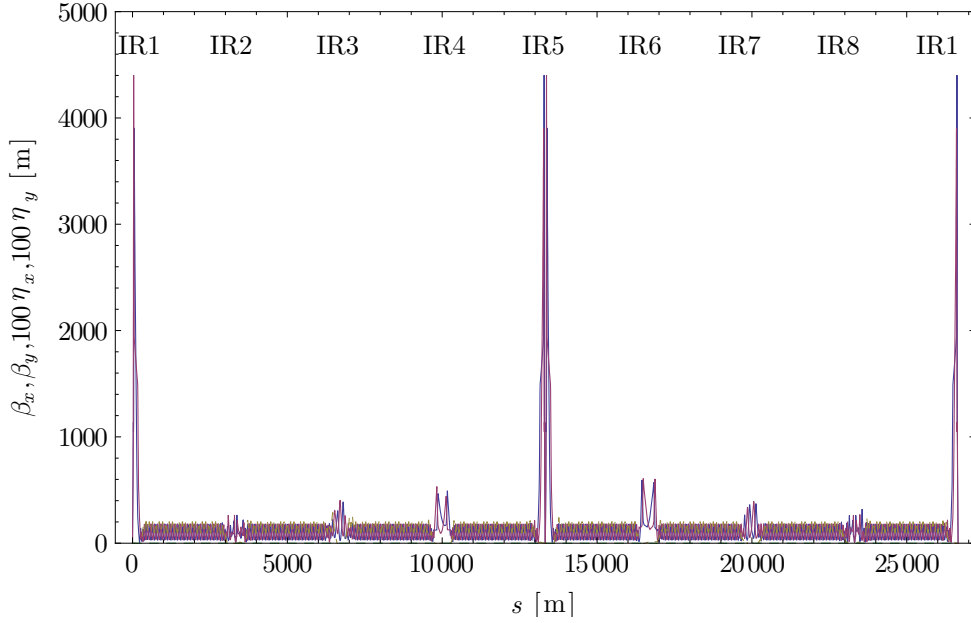
Figure 3.3: Optical configuration of the LHC in regular pp collision mode at LHC design energy. The periodic FODO structure in the arcs, and the matched optics in the different IRs are clearly visible. β_x in blue, β_y in red, $100\,\eta_x$ in green.

The quadrupoles in every octant are labeled by their type and their position with respect to the closest Interaction Point (IP). The IR quadrupoles are those from Q13 left to Q13 right of the IP [B+04]. The positions of all insertions in terms of the distance from IP1, which is called the global LHC s-variable, is given in Table 3.1. The optical configuration in the whole machine is shown in Fig. 3.3. Since IR2 is the region of interest in this thesis, this region is discussed in more detail in Chap. 3.5.

3.3.1   Layout

Due to the bending magnets in the arc regions, the horizontal dispersion function at the beginning of the IR is very large and must be reduced for the collision region. At the beginning of every experimental IR, the DS, a section of 4 quadrupoles and 2 dipoles, provides a first matching of the betatron functions and a reduction of the periodic dispersion function. This is reached by a so-called missing dipole structure [B+04].
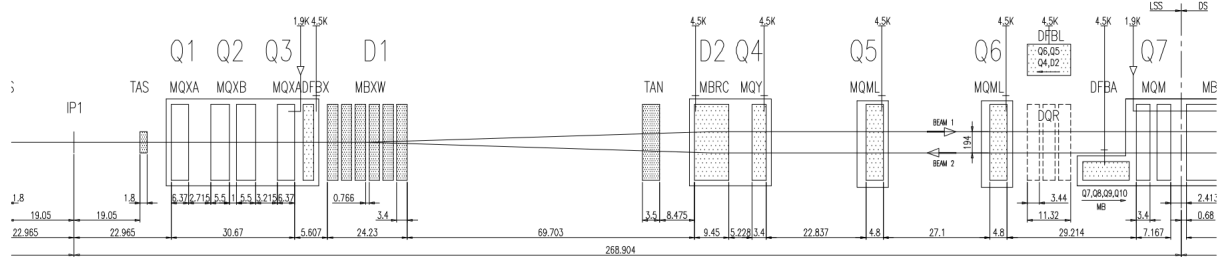
Figure 3.4: Layout of the right hand side of the IR1 Long Straight Section [B$^+$04].

Thanks to this initial reduction, the horizontal dispersion functions can be brought to zero at the IP, if all the bumps in the machine are switched off (see Chap. 3.4.3). Four independently powered quadrupoles are installed between the DS and the low β-triplet, composing the matching section. In this section, the optical functions are modified to match the requirements of the final focusing quadrupole triplet [B$^+$04, B$^+$12a]. Between the matching section and the triplet, a set of two dipoles is installed to guide the beams from the two separated pipes into the common vacuum pipe and vice versa. In the triplet, the two beams are already moving in the same pipe. The described properties apply to the four experimental regions IR1, IR2, IR5, and IR8. In the functional insertions IR3, IR4, IR6, and IR7, the beams are always moving in two distinct beam pipes and no triplets are installed (see Fig. 3.5 and Fig. 3.6), because no collisions take place.

Table 3.1: Locations of the eight IRs of the LHC in terms of the global LHC coordinate.

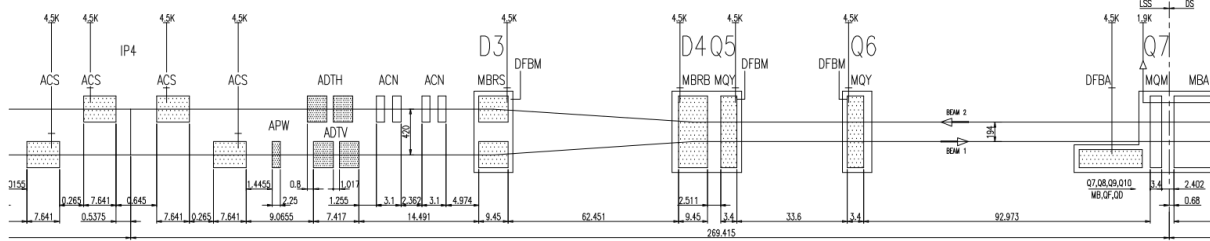|	Position s [m]		
Region	Start of DS	IP	End of DS
IR1	26111.7	0	547.2
IR2	2785.7	3332.4	3879.2
IR3	6117.5	6664.7	7211.9
IR4	9450.3	9997.0	10543.7
IR5	12782.1	13329.3	13876.5
IR6	16115.0	16661.7	17208.5
IR7	19447.0	19994.2	20541.4
IR8	22779.8	23315.4	23873.3

3.3.2 Experiments and Functional Units

Figure 3.5: Basic layout of the right hand side of IR4 [B$^+$04].

The regions IR1 and IR5 are host of the ATLAS[2] and CMS[3] experiments, respectively. Both are high luminosity insertions which have been optimized for smallest β*-values in proton runs (β* = 0.55 m at 7 TeV). Their layout in terms of the quadrupole positioning is very similar. In the pp high-luminosity mode, the β*-value at injection is 11 m for both regions. The two experiments are dedicated to the search of new physics, e.g. the Higgs particle and SUSY. Besides the CMS detector, the smaller TOTEM [4] Roman Pot detectors are located in IR5. This experiment is dedicated to the study of diffractive physics and to the measurement of the pp cross-section (see Chap. 4). For these studies, a dedicated optical configuration with a very large β*-value is necessary. The optics for these measurements have β*-values in excess of 1000 m. A similar setup is installed in IR1 with the ALFA[5] sub-detectors. The measurements in both regions, IR1 and IR5, are realized at the same time [B$^+$11].

The smallest experiment is the LHCf[6] experiment, hosted in IR1, which measures the forward energy and particle flow for an improved understanding of cosmic rays [LHC13].

The regions IR3 and IR7 contain beam collimation systems and are host of the primary and secondary collimators. There are no collisions in these two regions, so the optics are optimized for the collimation [B$^+$04].

IR4 serves for the acceleration of the particle beams and hosts radio frequency and feedback systems [B$^+$04]. The accelerating cavities are installed in the former ALEPH[7] cavern from the LEP accelerator [B$^+$04]. The region is not subject to serious optical constraints, but the dispersion function at the cavities should be matched to be zero [A$^+$08]. The current IR4 optics at top energy, having a phase advance of $\Delta\psi_x^{\mathrm{IR}}/\Delta\psi_y^{\mathrm{IR}}$ =2.143/1.870, are shown in Fig. 3.6.

---

[2] A Toroidal LHC ApparatuS

[3] Compact Muon Solenoid

[4] Total Cross Section, Elastic Scattering and Diffraction Dissociation at the LHC

[5] Absolute Luminosity For ATLAS

[6] Large Hadron Collider forward

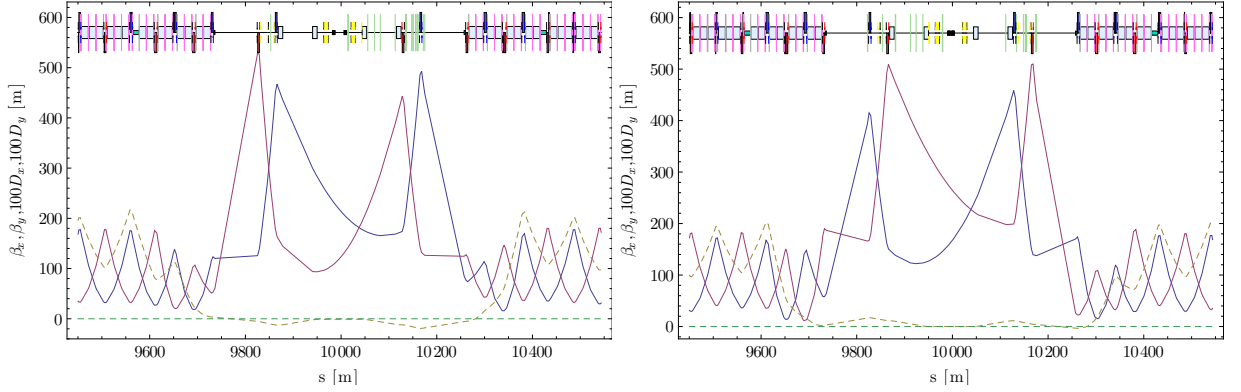[7] Apparatus for LEP PHysics at CERN

Figure 3.6: IR4 optics in the collision mode at top energy [B$^+$04](global LHC coordinates). The periodic dispersion is here denoted by D. Blue: β_x, red: β_y. Dashed lines represent the periodic dispersion (all bumps are switched off). Left: Beam 1, right: Beam 2.

IR6 is hosting the beam dumping system: In case of instabilities, or if the intensity of the beams has decreased below a certain level, the beams are kicked into a 7 m long segmented carbon cylinder in a specially shielded environment [B$^+$04].

The LHCb[8] experiment is hosted in IR8. Similarly to ALICE, the experiment houses a big spectrometer magnet and the injection magnets for one of the two LHC beams (Beam 2). The experiment is designed for the study of CP violation in charm and beauty particle decays.

---

[8]LHC beauty experiment

3.4   Beam Properties in the LHC

3.4.1   Beam Parameters

Table 3.2: Beam parameters of the LHC in different standard operational modes [B+04].

	Unit	Protons		Lead Ions	
		Injection	Collision	Injection	Collision
Energy	[GeV]	450	7000	36900	574000
Relativistic γ		479.6	7461	190.5	2963.5
Max. Luminosity[a]	[cm^{-2} s^{-1}]	$1.0 \cdot 10^{34}$		$1.0 \cdot 10^{27}$	
Num. of bunches		2808		592	
Bunch spacing	[ns]	24.95		118.58	
Part. per bunch		$1.15 \cdot 10^{11}$		$6.7 \cdot 10^{7}$	
Beam current	[A]	0.582		0.00612	
Norm. emittance	[μm rad]	3.50	3.75	1.40	1.50
Bunch length σ_l	[cm]	11.24	7.55	9.97	7.94
Momentum spread	[10^{-3}]	1.90	0.45	0.39	0.11
β^* at IP2	[m]	10	10	10	0.55

---

[a]In ATLAS and CMS for protons, in ALICE for heavy ions.

The LHC can be operated in a large number of different modes and has a large dynamic energy range (450 GeV $\leq E_{\text{Beam}} \leq$ 7000 GeV). An overview of basic properties at different beam configurations is given in Table 3.2. From injection mode to the collision mode (see Chap. 3.4.2), the normalized beam emittance slightly increases. In design configuration, it is foreseen to have 2808 bunches per beam circulating in the machine, which corresponds to a bunch spacing of 25 ns or 7.495 m. Up to now, these bunch spacings have only been realized in special machine development runs. The nominal filling scheme for pp operation in the past running period was using a bunch spacing of 50 ns or 14.9 m. The normalized emittances under real conditions were much smaller (as low as $\epsilon_N = 2.0 \, \mu$m rad [K+11] at 3.5 TeV), than those which are considered in the LHC Design Report, because the injectors were capable to deliver beams of a very good quality to the LHC.

3.4.2 LHC Cycle

During the LHC operation, specific conditions must be fulfilled for every step from injection to collision. One full operational cycle of the LHC in high-intensity pp operation is shown in Fig. 3.7. The different steps in one physics cycle are [B$^+$03]:

1. Filling of the machine: Injection of particle bunches from the SPS.

2. Ramping: Acceleration of the particle beams to the desired energy.

3. Squeeze: Transition from the injection to the collision optics.

4. Physics: Letting the beams collide in the Interaction Points.

5. Dump: Dumping of the particle beams in IR6.

6. Ramp down: Bringing the magnet currents down to zero.

7. Prepare Injection: Bringing the magnets to injection configuration.

This procedure is different if special running conditions are applied.
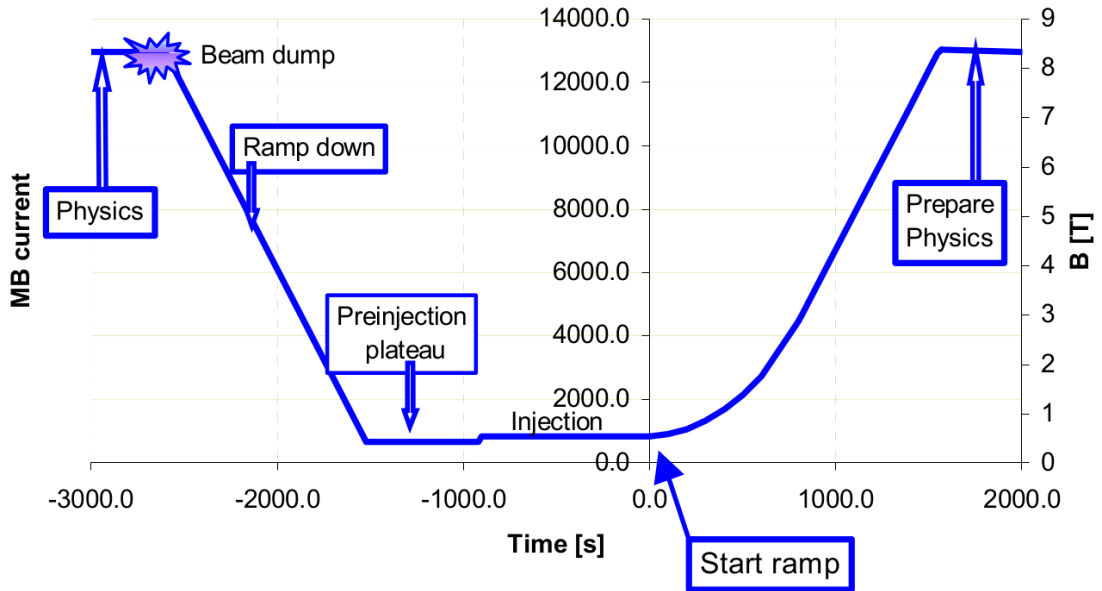
Figure 3.7: LHC cycle in the standard high intensity mode [B$^+$03].

3.4.3   Separation and Crossing Bumps
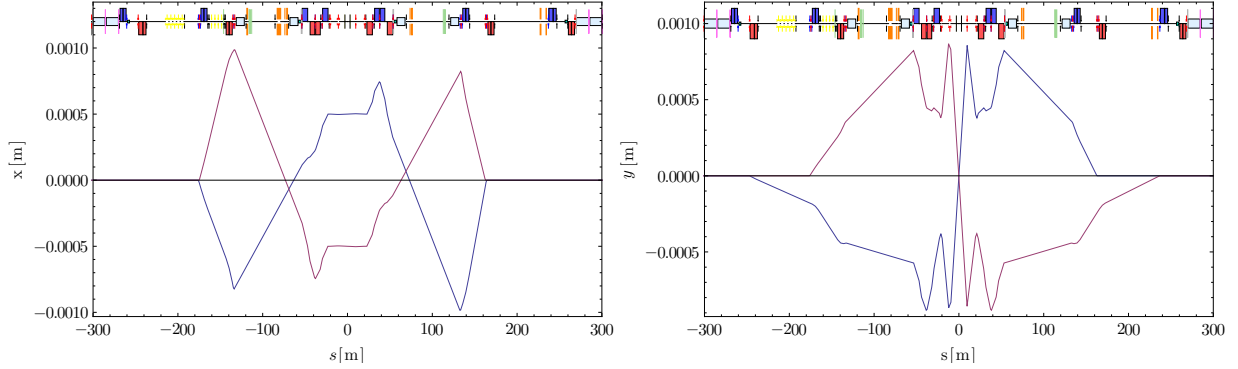
Figure 3.8: IR2 horizontal separation bumps (left) and vertical crossing bumps with spectrometer magnet switched on (right). Blue: Beam 1, Red: Beam 2.

In the central part of the experimental IRs, where the two beams move in a common vacuum pipe, separation and crossing schemes are applied to avoid unwanted interactions (see Chap. 2.5.1).

During all the stages of the cycle where no collision is supposed to happen, the two beams are fully separated by a separation bump which is created by the dipole corrector magnets (see Chap. 3.5.3). This bump can be either in the horizontal or in the vertical direction. In ALICE, a horizontal separation bump is applied, which leads to a separation of $5\,\sigma$ [B$^+$04].

In the collision mode, the bunch-bunch separation at the parasitic bunch encounters is provided by a vertical crossing bump, which is induced by the corrector dipoles and by the ALICE spectrometer magnet. The largest reachable crossing angle at LHC design energy is $\theta_C = 300\,\mu$rad. The IR2 crossing and separation schemes in pp mode at LHC design energy are shown in Fig. 3.8.

If the vertical bumps in the accelerator are switched on, the vertical periodic dispersion function in the machine is non-zero. Additionally to the bumps induced by the orbit corrector magnets, the spectrometer magnets in the two experiments ALICE and LHCb lead to deviations of the ideal orbit and of the horizontal and vertical dispersion functions. The impact of the ALICE muon spectrometer bump on the crossing angle is discussed in Chap. 3.6.

For the calculation of the dispersion function, the bump settings in all IRs must be taken into account. In the following, for every graphical representation of the periodic dispersion, the corresponding settings will be indicated.

3.5 Insertion Region 2
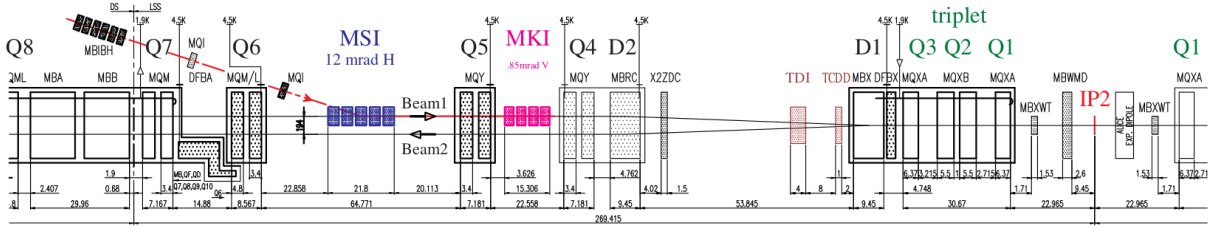
3.5.1 Layout

Figure 3.9: Layout of the left hand side of IR2 (without dispersion suppressor and arc) [B$^+$12a].

The inner part of IR2 is shown in Fig. 3.9. All quadrupoles, except the triplet magnets, are double bore magnets, with one quadrupole for each beam, installed in the same cryostat (see Fig. 3.10). The trim quadrupoles Q12 and Q13 are considered to be IR quadrupoles, but are installed before the DS. The dispersion suppressor reaches from Q11 to Q8, the matching section from Q7 to Q4, and the final focusing triplet from Q3 to Q1. The quadrupole positions, but not the quadrupole types, are the same on the left and right hand side of the Interaction Point. IR2 is an exceptional region because Beam 1 is injected between Q6 and Q5 on the left hand side of the region. Therefore, additional magnets, the injection septum MSI and the injection kicker MKI are hosted here. The aperture of Q5 on the left side is increased to provide more space for possibly mismatched beams [Brü99]. The separation/recombination dipole magnets D1 and D2 are installed between Q3 and Q4, in order to guide the beams from the common vaccum pipe to the separated beam pipes and vice versa. Before D2, the Zero Degree Calorimeter (ZDC) is installed, which is part of the ALICE detector (see Chap. 3.6).
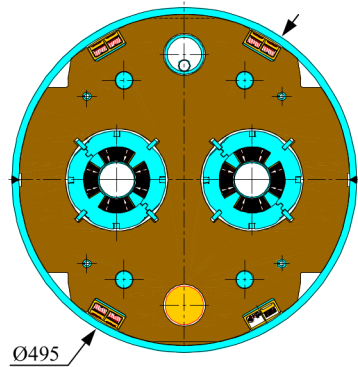
Figure 3.10: Profile of a LHC MQM double bore quadrupole [B$^+$04].

3.5.2   Quadrupole Magnets

Magnet Types and Properties

Table 3.3: Quadrupole magnet parameters in IR2 [B$^+$04, Brü99].

| | Long Straight Section | | | | | | Optical DS | | | | | |
| | Triplet | | | Matching Section | | | Dispersion Suppressor | | | | Arc Cell | |
Quad	Q1	Q2	Q3	Q4	Q5	Q6	Q7	Q8	Q9	Q10	Q11	Q12	Q13
Modules	1	2	1		2			1	2	1	1	1	1
MQ^a-	XL	L	XL	Y	Y/M^b	M	M	ML	M/MC^c	ML	TL	T	T
L [m]	6.3	5.5	6.3		3.4			4.8	3.4/2.4^b	4.8	1.15	0.32	
T [K]		1.9			4.5		1.9		1.9			1.9	
g [T/m]		215/220			160		200		200		110	110	

---

^{a}The prefix of the magnet denomination: MQXL, MQL, MQY,...
^{b}Left/right of IP2.
^{c}First and second module QA and QB.

Various types of magnets are used in the LHC, depending on the specific requirements in the corresponding region. Every magnet type has a particular nominal gradient (see Table 3.3). Some of the quadrupoles can be driven with both polarities, whereas others can only be operated with one given polarity. Depending on the expected beam sizes, some quadrupoles are designed as high aperture magnets (e.g. the MQY quadrupoles), but have a reduced nominal gradient. The quadrupoles in IR2 have some meters of length and are cooled down to a temperature of 1.9 K/4.5 K. Some of the magnets are installed twice in a very short distance from each other (referred to as one magnet split into two modules QA and QB). In the following, the magnet strengths are given in terms of k (see Eq. 2.8), in units of m^{-2}. In the LHC, each quadrupole strength is assigned to a specific denomination, indicating the quadrupole's type, position, and which beam it is acting on. For example, the expression KQTL11.R2B1 denotes the strength of the MQTL trim quadrupole Q11 right of IP2, for Beam 1. A complete table with all quadrupole strength denominations and the respective allowed ranges in terms of k is given in Table 7.1 in the Appendix. Details on the different quadrupole types can be found in [B$^+$04].
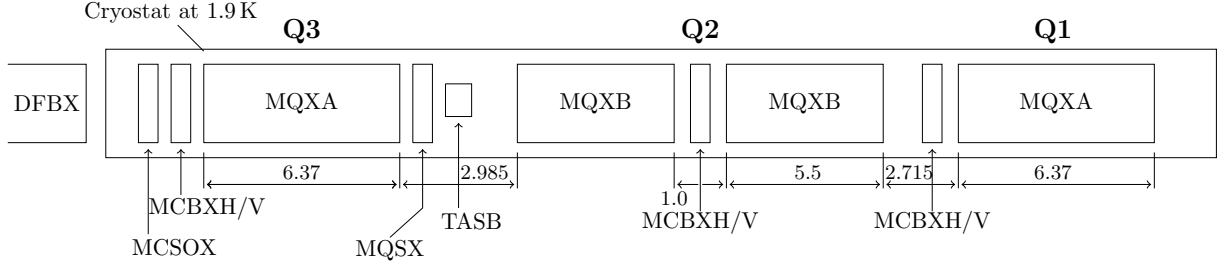
Triplet Quadrupoles

Figure 3.11: IR2 low β-triplet, schematic arrangement (original drawing in [B$^+$04]).

The triplet quadrupoles are special magnets designed at KEK[9] (MQXA, a single module magnet used for Q1 and Q3) and at FNAL[10] (MQXB, a two-module magnet used for Q2) [B$^+$04]. They are hosted in the same cryostat, together with corrector dipoles and skew quadrupoles, as shown in Fig. 3.11. The powering strength of the triplet quadrupoles is called KQX.L2 for the left side and KQX.R2 for the right side of the IP. The two strengths must obey the constraint

$$\mathrm{KQX.L2} = -\mathrm{KQX.R2}\,. \tag{3.1}$$

In addition to the main powering strength, which is related to the common current in the three quadrupoles, the currents of the individual magnets can be adjusted by two independent triplet trims with the strengths KTQX1.L2 and KTQX2.L2 (correspondingly .R2 for the right side).
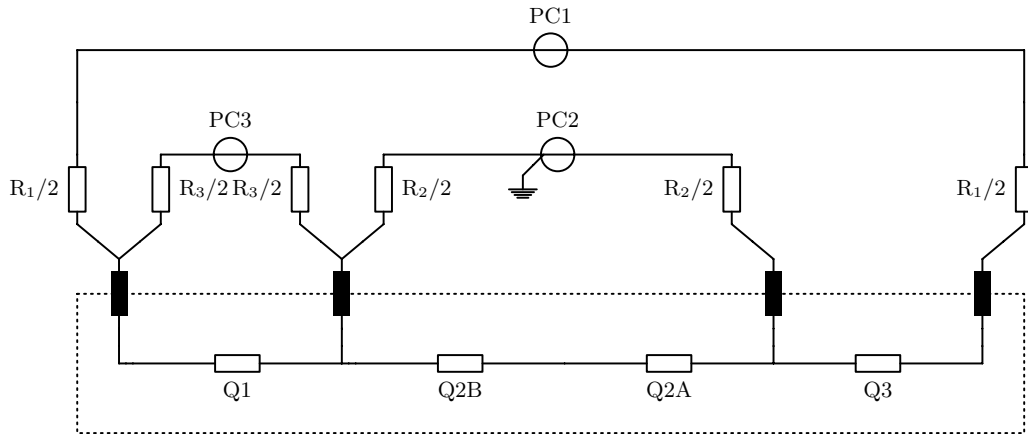
Figure 3.12: Powering scheme of the triplet quadrupoles with the trims [BT01].

---

[9]kō-energī kasokuki kenkyū-kikō research centre, Tokio, Japan.
[10]Fermi National Laboratory, Chicago, USA

Table 3.4: Circuit parameters of the three triplet power converters [BT01].

PC1	[8kA,8V]	PC2	[6kA,8V]	PC3	[$\pm$600 A,$\pm$10 V]
R_1	0.6 mΩ	R_2	0.8 mΩ	R_3	1.4 mΩ
τ_1	380 s	τ_2	50 s	τ_3	65 s

The powering scheme of the triplet magnets, including the triplet trims is shown in Fig. 3.12. Power converter 1 (PC1) provides the main supply of the triplet (KQX). PC2 is the trim supply for quadrupole 2 (KTQX2) and PC3 for Q1 (KTQX1). The circuit parameters of the power converters are given in Table 3.4. The arrangement of the triplet magnets with the shown cabling imposes constraints on the currents of the trims. The maximum current of PC2 is the difference $I_{PC2} = \Delta I = 4780$ A, between the maximum currents of MQXB and MQXA. The power converter for the trim of Q1 is independent and can produce a current of $I_{PC1} =$600 A [B$^+$04]. Also the KTQX strengths should be anti-symmetric on both sides of the IP.

Cabling

The double bore quadrupoles Q4-Q10 in the MS and the DS are imposed to an additional constraint, due to the present cabling. In Fig. 3.13, the cabling of the power converters for the two channels of the double bore magnets is shown. Since the two coupled power converter circuits have only one common return cable drawn back, the current in the left channel of the double bore magnet may only be twice as strong as in the right channel, and vice versa [Bur13].
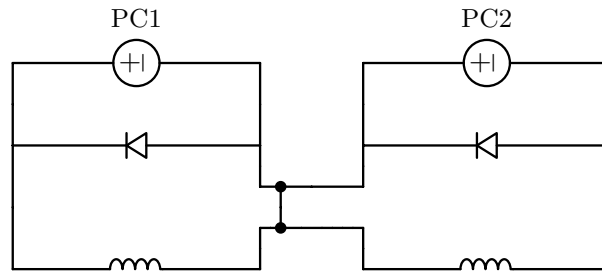
Figure 3.13: Cabling of the double bore quadrupoles [Bur12a]. Only one return cable is installed between the two power converter circuits, which limits the accessible current in one channel as a function of the current in the other channel.

If the current in the left channel is denoted by I_1 and the current in the right channel by I_2, the constraint can be summarized by

$$0.5 \leq I_1/I_2 \leq 2 \,. \tag{3.2}$$

The current ratio constraint limits the applicable optics in terms of B1/B2 symmetry, so the optics of Beam 1 may not be too different from the optics of Beam 2. This constraint has to be considered in the design of an optical configuration for the LHC. In principle, the ratio limit can be abolished, if an additional cable is installed in parallel to the existing cable [Bur12a].

3.5.3 Corrector Magnets

Table 3.5: Vertical orbit corrector magnet types in IR2 [B+04].

Magnet	Length [m]	$B_{\max}{}^a$ [T]
MCBYV	0.899	3.00/2.50
MCVCV	0.904	3.11/2.33
MCVXV	0.480	3.26

---

[a] At 1.9/4.5 K. The triplet corrector magnet MCVXV is always operated at 1.9 K.

Several dipoles are used as corrector magnets to control the orbits of the particle beams [B+04]. They are individually operated and significantly shorter than the bending dipoles, which are 14.3 m long [B+04]. An overview of the vertical corrector magnet types in IR2 is given in Table 3.5. Apart from orbit correction, they are used to create crossing angle and separation bumps. One exception of the shown corrector magnets is MCVXV. It is installed behind every triplet quadrupole (see Fig. 3.11), and is acting on both beams in the common vacuum pipe.

3.5.4 Beam Optics and Properties

Injection

Since the injection of Beam 1 takes place in IR2, the injection optics in this region are subject to many constraints. For example, the phase advances between the MKI and the TDI as well as between the TDI, and the two auxilliary collimators must be matched to specific values [B+04]. Besides the phase advance constraints, the optics must obey the constraint imposed by the available geometrical aperture. The β^*-value at injection is 10 m.
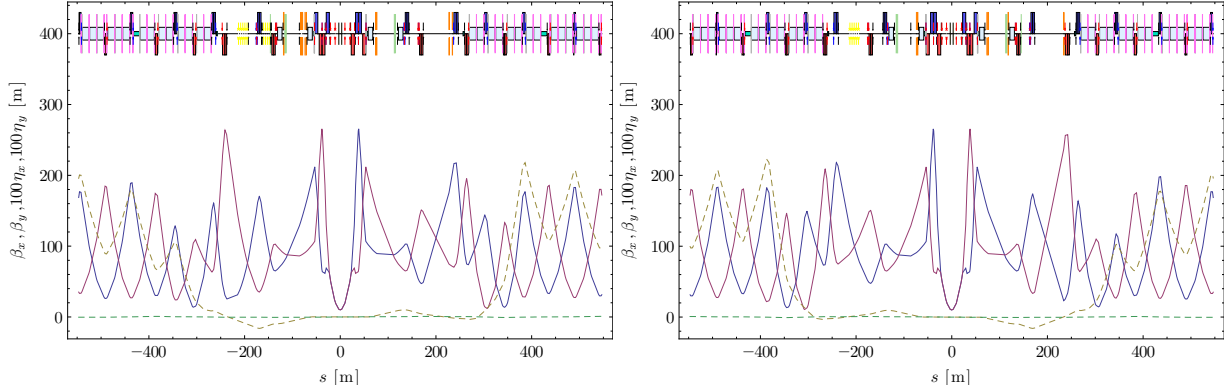
Figure 3.14: IR2 proton collision optics at LHC design energy. Red line: β_x, blue line: β_y, dashed orange line: $100 \cdot \eta_x$, dashed green line: $100 \cdot \eta_y$. All bumps in the machine are switched off. Left: Beam 1, right: Beam 2.

Collision

Since the optical configuration which is used at injection would imply a too large triplet current at top energy, the collision optics have different properties, even if the β^*-value is kept constant. The collision optics for IR2 are shown in Fig. 3.14. Since the ALICE detector can only handle a limited amount of luminosity, the β^*-value in nominal proton operation is not reduced to values below $\beta^* = 10\,\mathrm{m}$ [Mor01]. The total crossing angle in IR2 is the sum of the external bumps by the corrector magnets and a bump which is created by the ALICE spectrometer magnet and the compensating corrector bumps (see Chap. 3.6).

During nominal pp operation at LHC design energy, a total crossing angle of

$$\theta_C = 175.8\,\mu\mathrm{rad} \tag{3.3}$$

is going to be applied. The betatron phase advance over the whole IR is for both beams

$$\Delta\psi_x^{\mathrm{IR}}/\Delta\psi_y^{\mathrm{IR}} = 2.991/2.844\,. \tag{3.4}$$

The triplet trims are not used in the standard configuration.

3.6 ALICE - A Large Ion Collider Experiment
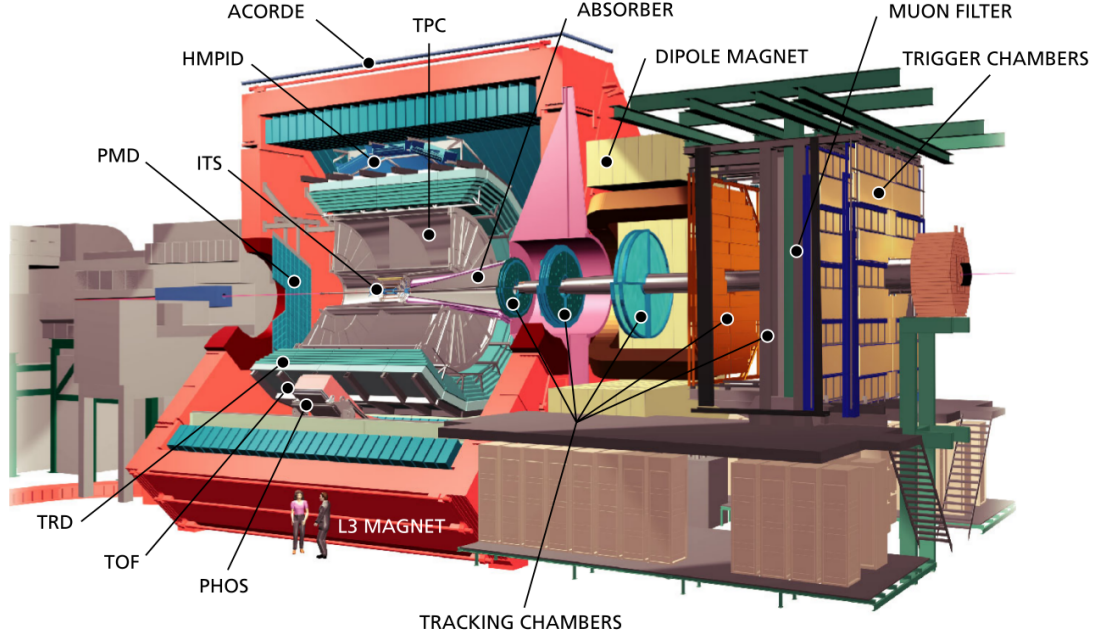
Figure 3.15: Schematic layout of the ALICE detector [ALI04a].

ALICE (A Large Ion Collider Experiment) is the experiment hosted in IR2. It is designed for the study of heavy-ion collisions but it is used to study collisions of protons, light-ions and p-Pb collisions as well. The main purpose of ALICE is the study of an extreme state of matter with deconfined quarks and gluons, the quark gluon plasma (QGP) [ALI08a]. For the identification and the analysis of the QGP, several signatures are studied [LA05]. To be able to reconstruct the properties of the QGP as well as possible, the detector was optimized for a good track reconstruction, a good primary and secondary vertex reconstruction, as well as a good particle identification capability. The detector is composed of 18 sub-detectors. The two sides (left and right of IP2) are called A-Side and C-Side respectively. In a generalized way, the sub-detectors can be subdivided into three groups, depending on the pseudo-rapidity[11] range which they cover:

- Central Barrel: Covering the pseudorapidity range of $-0.9 \leq \eta \leq 0.9$,

- Muon arm: Detection and identification of muons in the range $-4.0 \leq \eta \leq -2.5$,

- Forward detectors with a coverage of $1.7 \leq |\eta| \leq 5.1$.

---

[11]The pseudorapidity is given by $\eta = -\ln\left[\tan\left(\frac{\theta}{2}\right)\right]$, where θ is the polar angle between the particle's momentum vector and the beam axis [Par10].

The elements of the central barrel are installed in a solenoid which was already used for the L3 experiment at the LEP accelerator [L3 90]. It is an octogonal steel yoke with doors that can be opened for maintenance, but which are closed during operation [Bul02]. The solenoid magnet is operated at room temperature and creates a nearly homogeneous field of 0.5 T [Fab08] which allows momentum measurements of charged particles. The LHC beam pipe goes through the centre of the solenoid. The sub-detectors in the central barrel are arranged in a cylindrical structure around the beam pipe. A short description of the detectors in the central barrel is given in the following (from inner to outer).

The Inner Tracking System (ITS) is the innermost detector in the central barrel and comprises several types of silicon detectors. The main task of the ITS is the precise track reconstruction, down to transverse momenta of 150 MeV, the precise primary and secondary vertex reconstruction, as well as the identification of the charged particle [ALI10].

The Time Projection Chamber (TPC) is the main tracking detector in the central barrel [ALI00]. The TPC is used for the measurement of the momentum of charged particles and the particle identification at extreme particle multiplicities present in central heavy-ion collisions. It is the slowest detector of ALICE and therefore the limiting factor for the read-out frequency [ALI00].

The Transition Radiation Detector (TRD) allows for an excellent electron/pion separation and an improved tracking at high transverse momenta. It is also used to trigger on rare processes [ALI01].

The Time of Flight Detector (TOF) is the outermost detector with full azimuthal coverage. The detector provides particle identification by measuring the flight time. For this purpose, it consists of a multigap resistive plate chamber array with good time resolution [ALI04a].

While ITS, TPC, TRD and TOF have a full azimuthal coverage, the central barrel hosts also sub-detectors with limited azimuthal coverage [ALI08a]. The High Momentum Particle Identification Detector (HMPID) is a detector based on proximity focusing Ring Imaging Cherenkov counters, used to enhance the overall particle identification capability [ALI08b]. The covered pseudo-rapidity range is $0.6 \leq |\eta|$ and the covered azimuthal range is $\Delta\phi = 57.6°$. The PHOton Spectrometer (PHOS) is an electromagnetic calorimeter consisting of 17920 lead-thungstate cristal detection channels [ALI08b], covering $0.12 \leq |\eta|$ and $\Delta\phi = 100°$. The Electro-Magnetic Calorimeter (EMCal) is a Pb-scintillator sampling calorimeter in a range of $0.7 \leq |\eta|$ and $\Delta\phi = 107°$ [ALI08b]. In the forward region, the Forward Multiplicity Detector (FMD) and Photon Multiplicity Detector (PMD) are installed. The FMD covers a pseudo-rapidity range of $1.7 \leq |\eta| \leq 5.1$. It is installed on both sides of the central barrel and is used to measure charged particles which are emitted at small angles with respect to the beam axis [ALI08b]. The PMD measures photons in the pseudo-rapidity range $2.3 \leq \eta \leq 3.7$ [ALI08b].

To filter events which are based on cosmic showers, a muon trigger called ACORDE (ALICE COsmic Ray DEtector) is placed on top of the L3 solenoid magnet [ALI04a].

The Zero Degree Calorimeter (ZDC) is installed twice in a longitudinal distance of ± 115 m from the IP. It is used to measure neutrons and protons from the interaction to reconstruct the initial configuration of a collision [ALI08b]. In heavy-ion and p-Pb operation, the ZDC limits the reachable crossing angle in IR2 to $\theta_C = 60\,\mu$rad [VJ12]. In pp operation, a larger crossing angle must imperatively be applied, because more bunches are circulating in the machine.

The T0 detector is a trigger detector to supply main signals to the L0 trigger [ALI04b] and to deliver an early wake-up to the TRD. It provides also the start signal to the TOF detector. The V0 detector provides multiplicity information and luminosity control [ALI08b].

On the C-Side, right behind the central barrel (downstream, with respect to Beam 1), the muon arm is located. The muon arm is composed by an absorber, a spectrometer magnet, a tracking system, a muon filter, and trigger chambers [ALI08b].

The muon spectrometer magnet is always switched on [AF+12] and creates a permanent bump in the beam orbit, which is by default compensated by external corrector magnets. The spectrometer bump with the corresponding correcting bumps leads to a so-called internal crossing angle in ALICE, which is a function of the energy and the particle type, described by the relation [AF+12]

$$\theta_{\text{spec}}/2 = \pm \frac{490\,\mu\text{rad}}{Z \cdot E/\text{TeV}}\,, \tag{3.5}$$

where Z is the ion charge and E is the beam energy in TeV. The impact of the muon spectrometer magnet on the total crossing angle has to be considered in the crossing bump design. The total crossing angle can be written as the sum of the crossing angles by the external corrector magnets and the spectrometer bump

$$\theta_{\text{tot}} = \theta_{\text{spec}} + \theta_{\text{ext}}\,. \tag{3.6}$$

To keep the pile-up in the TPC and the silicon detectors in the ITS at low rates, the luminosity should not exceed a certain level. The acceptable luminosity during pp-operation is [Mor01]

$$\mathcal{L}_{\text{max}} = 5 \cdot 10^{30}\,\text{cm}^{-2}\,\text{s}^{-1}\,. \tag{3.7}$$

With $\beta^* = 10$ m, the luminosity in high-intensity pp runs with the largest number of bunches and the design parameters in Table 3.2 will be

$$\mathcal{L} = 5.5 \cdot 10^{32}\,\text{cm}^{-2}\,\text{s}^{-1}\,, \tag{3.8}$$

so techniques for additional luminosity reduction will have to be applied [Mor01].

3.7   Geometrical Acceptance of the LHC

The available aperture in the LHC is evaluated by means of an algorithm, which calculates a so-called n_1 function [JR96], which is related to the settings of the primary collimators. The n_x and n_y functions are normalized coordinates, defined by [JO97]

$$n_x = \frac{x}{(1 + k_{\beta,x})\,\sigma_x}\,, \qquad n_y = \frac{y}{(1 + k_{\beta,x})\,\sigma_y}\,, \tag{3.9}$$

where x, y are the transverse coordinates, k_β is the β-beating[12] and σ (see Eq. 2.38) is the RMS beam size. A large number of collimators is used to protect the machine from halos and secondary particles, in order to avoid magnet quenching due to the heating which is related to the energy loss of the particles in the cold magnets. The collimators can be subdivided into primary, secondary and tertiary collimators, where the primary and secondary collimators are installed in IR3 and IR7. Apart from the collimation in the two transverse directions, the primary collimators (TCP) provide skew collimation, leading in total to a collimation in form of a regular octagon. The TCPs are used to absorb the primary beam halo, whereas the secondary collimators absorb the hadronic showers from this interaction. The halo starting from the edge of the primary collimators is called secondary halo, whereas the one starting from the edge of the secondary collimators is called tertiary halo. Besides the secondary and tertiary halo, the hadronic showers move from the primary and secondary collimators. These particles are absorbed by the tertiary collimators which protect the triplet magnets of the experiments. By definition, the primary collimators are set to $n_1 = n_x = n_y = n_{skew}$, which defines the primary aperture [JR96]. The secondary aperture is defined by n_2. The ratio of the primary and secondary aperture is [JR96]

$$n_2/n_1 = 7/6\,. \tag{3.10}$$

The minimum tolerable setting of the TCPs, including an operational margin is [JR96]

$$n_1^{\text{spec}} > 7\,. \tag{3.11}$$

For each position in the ring, the required TCP settings for protection against the secondary halo can be calculated as a function of the beam pipe dimensions, including tolerances, the beam size and the offset. If the required TCP setting $n_1(s)$ at the position s is [B$^+$04]

$$n_1(s) > n_1^{\text{spec}}\,, \tag{3.12}$$

then the aperture is considered to be safe at this position. Aperture calculations in terms of the n_1-function are natively integrated into MAD-X.

---

[12]k_β is the relative difference between the measured and expected β-value $k_\beta = \frac{\Delta\beta}{\beta}$.

4. Diffractive Physics

Introduction

At high energy collisions in hadron colliders, interactions can be observed, where large rapidity gaps $\Delta\eta$ occur in the final state. Such interactions are proccesses of the strong force and are usually referred to as diffractive events. The particle which is expected to be exchanged during such interactions is called the Pomeron [D$^+$02]. At LHC energies, about $40\%-50\%$ of the cross section in hadron-hadron interactions is based on diffraction [HS13, BV09]. Historically, the Pomeron was introduced to explain the rising cross section at p$\bar{\text{p}}$-collisions, which could otherwise not have been explained by the Regge-theory. This theory describes the hadron-hadron cross section by the exchange of related families of mesons and predicts a cross section which decreases with $\approx s^{-0.45}$, where $\sqrt{s}$ is the centre of mass energy [Cou99]. Whereas the experimental data from different experiments (e.g. the UA8 experiment) indicate the existence of the Pomeron, there is so far no strong experimental evidence for the existence of the C-odd counter-part of the Pomeron, the so-called Odderon [Cou99]. The Pomeron is predicted to be charge- and colourless [D$^+$02].
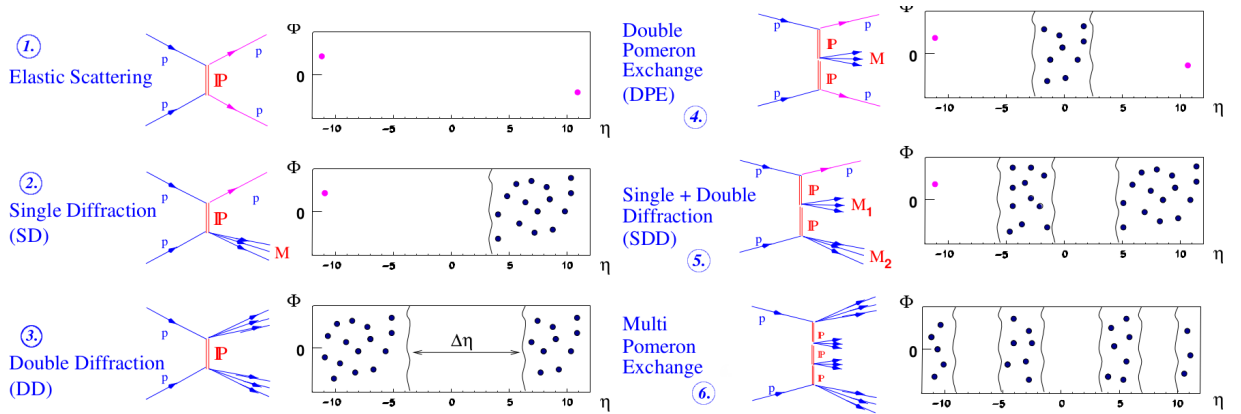
Figure 4.1: Event topologies of different diffractive events with the pseudo-rapidity and azimuthal distribution of the interaction products [BV09].

45

Some of the possible diffractive topologies are shown in Fig. 4.1. Single Pomeron exchange processes can be subdivided into elastic scattering ⓵, single diffractive dissociation ⓶ and double diffractive dissociation ⓷. Double Pomeron exchange processes can lead to central diffraction ⓸ and central diffraction with the break up of a proton ⓹. Higher order processes ⓺ involve more than two Pomerons.

Processes with the exchange of more than one Pomeron can lead to the production of a central system with new particles, which results in a momentum loss $\frac{\Delta p}{p} > 0$ of the interacting particles. Studies of the angular distribution of scattered particles can give information about the cross sections due to Pomeron exchange, as a function of the four-momentum transfer $|t|$. There are still many open questions in relation to these diffractive processes, which motivate measurements of soft collisions at LHC energies [HS13, BV09]. The main task in these measurements is the determination of $|t|$ and $\xi = \frac{\Delta p}{p}$, which are referred to as the diffractive parameters.

4.1 Diffractive Parameters

The four-momentum transfer is the square of the four momentum difference before and after the interaction. In the case of elastic scattering, this is the same for both particles (for processes with multi-Pomeron exchange, the t-values are in general different for the two protons) [Par10]

$$t = (p_1 - p_3)^2 = (p_2 - p_4)^2 . \tag{4.1}$$

In the approximation of very low ξ-values and very small scattering angles θ, the absolute value of t can be derived to be [Par10]

$$|t| \approx |p_1 \, p_3| \, \sin^2 \theta \approx p^2 \, \theta^2 . \tag{4.2}$$

The angle θ can be expressed in terms of its horizontal and vertical component

$$\theta^2 = \theta_x^2 + \theta_y^2 . \tag{4.3}$$

The scattering itself is azimuthally symmetric, so all the particles with a given $|t|$-value are located at the surface of a cone with an opening angle of $2\,\theta$, schematically shown in Fig. 4.3.
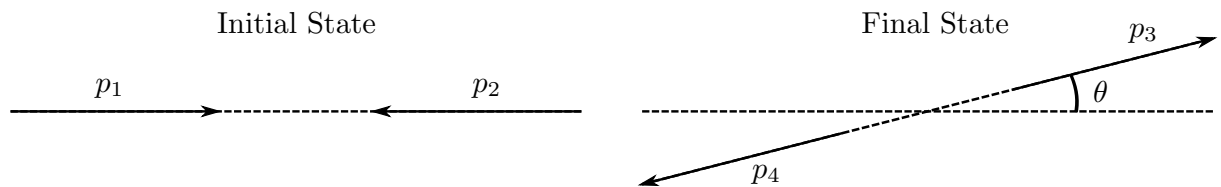
Figure 4.2: Particle momenta before and after an interaction.
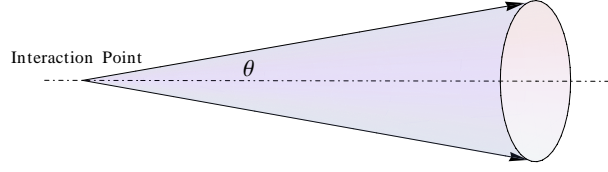
Figure 4.3: Azimuthal symmetry of the scattering at the IP. For a given $|t|$-value, a particle moves at the surface of a cone with opening angle $2\,\theta \approx 2\,\sqrt{\frac{|t|}{p^2}}$.

The second diffractive parameter is the fractional momentum loss

$$\xi = \frac{p - p_p}{p} = \frac{\Delta p}{p}\,, \tag{4.4}$$

where p_p is the real particle momentum, and p is the design momentum. By definition, elastic processes have $\xi = 0$, while inelastic interactions have $\xi > 0$.

4.2 High β^*-Optics

An effective measurement of diffractive events at a particle accelerator requires specifically adjusted beam optics with large β^*-values. Up to now, dedicated optics with $\beta^* = 90\,\text{m}, 500\,\text{m}$, and $1000\,\text{m}$ have been successfully implemented in IR1 and IR5, for the TOTEM and ATLAS-ALFA experiments (see Fig. 4.4). In these special configurations, no crossing angle is applied.

For such frontal collisions, the number of bunches in the machine is limited to 156. With this bunching scheme, the first potential bunch encounter after the IP is in a region where the two
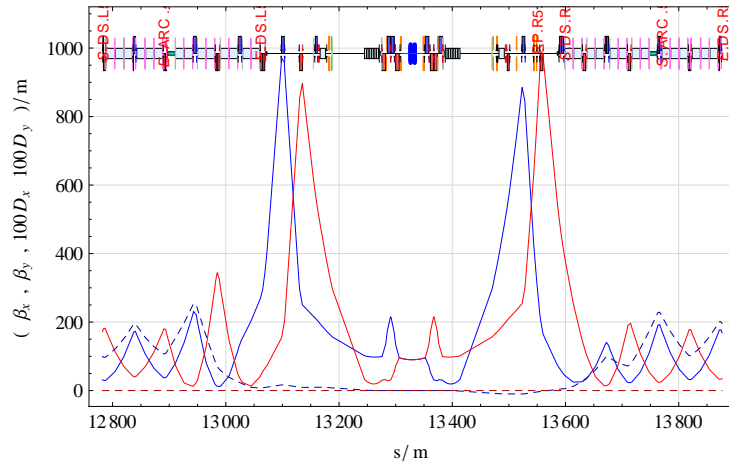
Figure 4.4: The TOTEM $\beta^* = 90\,\text{m}$ optics (Beam 1 in global LHC coordinates). The IP-RP phase advance to the second RP station is matched to $\Delta\psi_x/\Delta\psi_y = 0.5/0.25$.

beams are fully separated and moving in different beam pipes. Besides the large β^*-values, these configurations require specific phase advances between the IP and the very forward detectors. During the design of such a configuration, several approaches allow the optimization of the measurement at low $|t|$-values.

4.2.1 Measurement Optimization

The detection of the scattered particles will be realized by means of Roman Pot (RP) detectors which are described in the next chapter. This detector type measures the transverse position of the scattered particles very close to the beam centre. Two RP stations, labeled with the indices 1 and 2 are considered at different distances from the IP. Regarding Eq. 2.25 and taking into account the dispersion of the magnets between IP and RP, the total particle transfer from the IP to the two RP stations can be described by a 8×5 matrix

$$
\begin{pmatrix} x_1 \\ \theta_{x1} \\ y_1 \\ \theta_{y1} \\ x_2 \\ \theta_{x2} \\ y_2 \\ \theta_{y2} \end{pmatrix} = \begin{pmatrix} v_{x1} & L_{x1} & 0 & 0 & D_{x1}^{\text{loc}} \\ v'_{x1} & L'_{x1} & 0 & 0 & D_{x1}^{\text{loc'}} \\ 0 & 0 & v_{y1} & L_{y1} & D_{y1}^{\text{loc}} \\ 0 & 0 & v'_{y1} & L'_{y1} & D_{y1}^{\text{loc'}} \\ v_{x2} & L_{x2} & 0 & 0 & D_{x2}^{\text{loc}} \\ v'_{x2} & L'_{x2} & 0 & 0 & D_{x2}^{\text{loc'}} \\ 0 & 0 & v_{y2} & L_{y2} & D_{y2}^{\text{loc}} \\ 0 & 0 & v'_{y2} & L'_{y2} & D_{y2}^{\text{loc'}} \end{pmatrix} \begin{pmatrix} x^* \\ \theta_x^* \\ y^* \\ \theta_y^* \\ \xi \end{pmatrix} ,
\tag{4.5}
$$

where x_i/y_i are the horizontal and vertical positions at the RP station i, and θ_{xi}/θ_{yi} are the angles of incidence at the RP station i. The quantities which are labeled by a * are the parameters at the IP. The D^{loc}-functions are the local dispersion functions for the dispersion which occurs due to the magnets between the IP and the detector. This local dispersion is different from the periodic dispersion defined by Eq. 2.33, because it does not take the magnet configuration in the rest of the ring into account. This is visualized by the following scenario: Consider a particle moving towards the IP with design momentum p. Due to an interaction with another particle, the particle loses a fraction Δp of its momentum. After this, the particle moves towards the detector and is registered. Since the particle was not subject to any dispersive offset when it was at the IP, there is no reason to take into account the magnet configuration in other parts of the machine than between IP and detector.

For a given RP station, the particle position is then given by

$$x = v_x \, x^* + L_x \, \theta_x^* + D_x^{\text{loc}} \, \xi \,, \tag{4.6}$$

$$y = v_y \, y^* + L_y \, \theta_y^* + D_y^{\text{loc}} \, \xi \,. \tag{4.7}$$

The so-called optical length L and the parameter v are the essential parameters for the optimization of the measurement. Following Eq. 2.25, the elements L and v are defined for one transverse direction by the expressions

$$v = \sqrt{\frac{\beta}{\beta^*}} \cos\left(2\,\pi\,\Delta\psi\right) \,, \qquad L = \sqrt{\beta\,\beta^*} \, \sin\left(2\,\pi\,\Delta\psi\right) \,. \tag{4.8}$$

Here, β indicates the betatron function at the position of the RP, and $\Delta\psi$ is the betatron phase advance from the IP to the RP detector station. The measurements should be sensitive for very small $|t|$-values and there should be no dependence on the particle position at the IP. Since v is the component which projects the position at the IP to the position at the RP, this quantity should be zero. Furthermore, the dependence on the scattering angle θ^* should be very large, so the optical length L should be as large as possible. Both conditions are fulfilled if the β^*-value is as large as possible and if the IP-RP phase advance is matched to be $\Delta\psi = 0.25$. An optical configuration with this phase advance is parallel to point focusing. Besides the argument of maximizing L, the large β^*-value leads to a small beam divergence at the IP. For the measurement of small scattering angles, it is necessary to have as many particles in parallel to the beam line as possible, so the beam divergence should be minimized.

4.2.2 Detection - Roman Pot Detectors

The detection of the very forward particles requires not only a dedicated beam optics configuration, but also efficient and reliable detectors which can be brought as closely as possible to the beam centre. In the regions of ATLAS and CMS, Roman Pot detectors are used for the measurement of the very forward particles. This detector type was first used at ISR at CERN in the early 1970s [Cou08]. Modern RP detectors use very thin silicon detectors, the so-called edgeless silicon detectors [BV09], which can be individually steered around the beam centre (see Fig. 4.5 for the profile of the detector). A set of seven edgeless silicon detectors at three sides (two in vertical direction, one in horizontal direction) is installed in one Roman Pot (see Fig. 4.5 and Fig. 4.7). With the special conditions during the high-β^*-operation for TOTEM and ATLAS-ALFA, these detectors can be brought to a distance of $10\,\sigma$ to the beam centre. During high luminosity operation, the detectors have been moved to a distance of $14\,\sigma$ [Dei12].

One RP detector station consists of two units which are placed at a longitudinal distance of $4\,m$ from each other (see Fig. 4.6). In IR1, two detector stations are installed, one at a distance of $\pm 147\,m$, and one at a distance of $\pm 220\,m$ from the IP. The RP positions in IR5 are similar.

A second set horizontal detectors is not required for the ALFA and TOTEM detectors, because the horizontal phase advance is matched to $\Delta \psi_x = 0.5$. In this case, the horizontal particle distribution at the detector is not depending on the scattering angle. Since the particles can only lose longitudinal momentum during an interaction ($\xi > 0$) and the local dispersion is a property of the machine settings, the particles are always deviated in the direction of the installed horizontal detector on the outer side of the two beam pipes (see Chap. 6.1).

For the very forward measurements at ALICE, the RP positions have to be assumed, because the phase advance to the second detector station must be matched. This is discussed in Chap. 5.2.2.
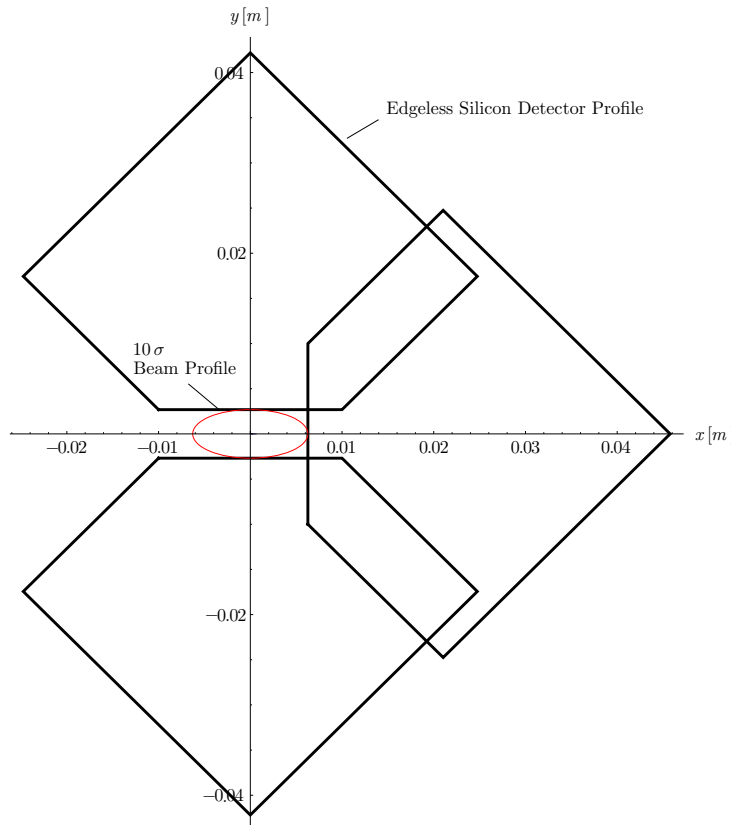
Figure 4.5: Profile of the edgeless silicon detectors in one module of a Roman Pot station. Here, the detector is at a distance of $10\,\sigma$ from the beam centre. Only one horizontal detector is installed on the outer side of the beam pipe. Figure based on [BV09].
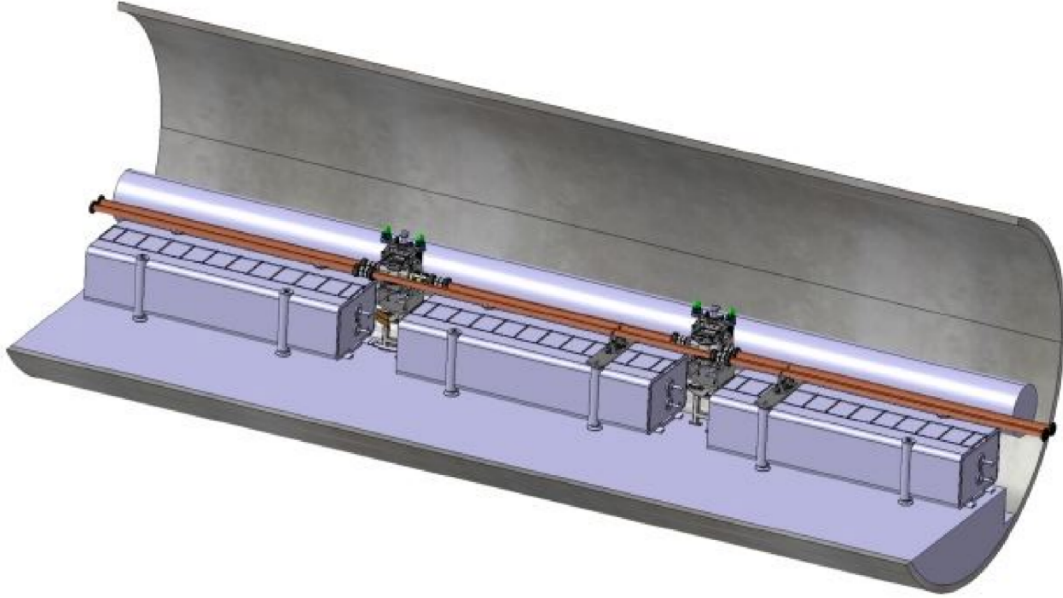
Figure 4.6: TOTEM Roman Pot station at 147 m distance from IP5. The two detector units are installed at a distance of 4 m from each other. Picture from [Hel10].
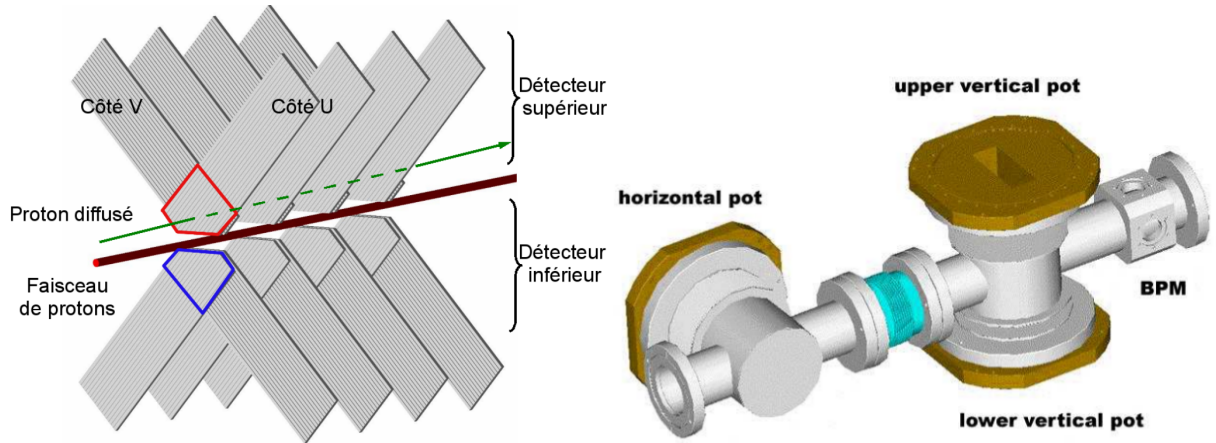
Figure 4.7: Left: Schematic view on the different layers of silicon edgeless detectors within one Roman Pot unit [Hel10]. In reality, seven layers are used. Right: Roman Pot detector unit, used in IR1 and IR5 with the two vertical pots and the horizontal pot [BV09].

5. High β^*-Optics at ALICE

Introduction

The implementation of the high β^*-configurations in ATLAS and CMS is only approved for very limited time scales, due to the reduction of luminosity in consequence of the larger β^*-value and the reduced number of bunches. For the same reason, a configuration with intermediate β^*-value, which would be compatible with the largest possible number of bunches, will also not be applied in the regions of ATLAS and CMS.

On the contrary, the ALICE detector requires a reduction of the luminosity in pp-operation. Therefore, ALICE would be capable to implement regular collision optics with a larger β^*-value, under the premise of compatibility with the high-luminosity mode of the LHC. Such a configuration will require a crossing angle, and many assumptions (e.g. the required bunch-bunch separation at the first parasitic encounter) will have to be made to determine which optical properties are possible.

The running time for such a configuration could possibly be more than 100 days/year. Another advantage of ALICE is the different detector design with respect to ATLAS and CMS. Thanks to the sensitivity of ALICE for low transverse momenta, and the good particle identification capability, the centrally produced systems of diffractive events could be fully detected and identified in the central barrel [Sch12, HS13]. The simultaneous detection of the central system in the ALICE central barrel and of the scattered protons in the very forward detectors could be used as a trigger for multi-Pomeron exchange events, leading to a very low background [S$^+$13]. This chapter describes the feasibility calculations for the β^*-value, the matching and refinements of the optical configuration, the evaluation of the boundary conditions and the matching of a crossing angle.

5.1   Boundary Conditions for the Optics Design

Besides the optimization of the measurement, many constraints imposed by the LHC in its current set-up will have to be respected in the beam optics design. Some of these constraints have been discussed in previous chapters, so only a brief summary will be given in the following. Apart from this, the conditions for an optimal measurement are briefly summarized.

5.1.1   LHC Constraints

1. The quadrupole strengths have to lie within the allowed range. In order to have a flexibility margin ($\pm10\%$) during LHC operation, the magnet design limitations must be tightened [B$^+$04]. A lower limit of 3% of the possible magnet strength is imposed by the power supply of the quadrupoles [B$^+$04]. In terms of the nominal strength k_{max} of a given quadrupole, the actual gradient k must fulfill the constraint [Gio12, Hol13]

$$0.03 \leq k/k_{max} \leq 0.90 \,. \tag{5.1}$$

   The individual gradient limitations for the different quadrupole types are listed in Table 7.1 in the Appendix.

2. As discussed in Chap. 3.5.2, the powering of the two channels in a double bore quadrupole is not independent from each other. The ratio I_1/I_2 of the quadrupole currents in the two channels must fulfill the constraint [Bur13]

$$0.5 \leq I_1/I_2 \leq 2 \,. \tag{5.2}$$

   However, the current ratio should not be pushed to the limit. Considering the required 10 % flexibility for each quadrupole, the limitation for operation is tightened to

$$0.56 \leq I_1/I_2 \leq 1.8 \,. \tag{5.3}$$

   For simplicity, not the current ratio itself, but a normalized parameter R_{12} is used in the following, which is defined as

$$R_{12} = \begin{cases} I_1/I_2 & \text{if } I_1 > I_2 \\ I_2/I_1 & \text{if } I_1 < I_2 \end{cases} \,. \tag{5.4}$$

   R_{12} is larger than one for all I_1 and I_2, which facilitates the comparison of different ratios. The considered currents I_1 and I_2 are the absolute values of the currents which normally have opposite sign with respect to each other. The current ratio constraint does not apply on the independent trim quadrupoles (MQT- and MQTL-) and on the single bore quadrupoles in the triplet region.

3. The beam-beam separation at the first parasitic beam encounter must be sufficient. As shown in previous chapters, beam-beam effects are non-linear and not yet fully understood. Even though simple rules for the required separation can be deduced, a clear statement on the required separation cannot be given. A conservative assumption for the required beam-beam separation in the crossing plane is $\Delta y = 12\,\sigma_y$ [Her12].

4. The beam dimensions must fit into the aperture of the LHC vacuum chambers. In addition to the beam dimensions, the orbit excursions due to crossing and separation bumps must be respected. The calculation of the available geometrical aperture is done by means of MAD-X, in terms of the LHC-specific n_1 function. This function must stay above the specified limit of $n_1 = 7$. For the presented calculations, the conservative estimation of $\epsilon_N = 3.75\,\mu$m rad, used in the LHC Design Report [B$^+$04], is taken as reference.

5. The LHC tune must be kept constant. Changes in the IR2 phase advance due to the calculated beam optics will have to be compensated in other parts of the ring. In high intensity operation, however, the phase advance between IP1 and IP5 should be matched to reduce the impact of beam-beam interactions [HK08]. Since the considered optics are intended to be implemented during high-intensity operation, not only the machine tune must be conserved, but also the phase advance between IP1 and IP5.

6. The optical functions α, β, η and η' at the beginning and the end of the IR must be matched to the boundary conditions imposed by the settings in the rest of the machine.

5.1.2 Requirements from the Measurement

1. To allow long time measurements, the optical configuration must be compatible with a bunch spacing of 25 ns at a beam energy of 7 TeV. This condition imposes a limitation on the achievable β^*-value. Hereby it must be considered that the achievable crossing angle is limited to $\theta_C = 300\,\mu$rad [B$^+$04].

2. The β^*-value should be as large as possible, in order to obtain the smallest possible beam divergence $\sigma^{*'} = \sqrt{\epsilon/\beta^*}$ at the Interaction Point and to be sensitive for the smallest possible $|t|$-values.

3. The betatron phase advance $\Delta\psi$ between the IP and the second RP station should be matched to a value as closely as possible to $\Delta\psi = 0.25$.

5.2   Prerequisites

Based on the considerations in the previous chapters, the basic approach for the design of the IR2 optics can be summarized in the following way:

1. Determine the largest possible β^*-value, as a function of the bunch spacing and emittance.

2. Determine the possible RP locations, in order to be able to match the IP-RP phase advance.

3. Define all matching constraints and variables.

4. Match optics with the desired β^*-value and IP-RP phase advance $\Delta\psi$.

5. Rematch for refinement: Reduction of the required phase advance compensation. Adjustments of specific quadrupole strengths. Optimization of the B1/B2 current ratio.

6. Check whether the LHC constraints are fulfilled by this optical configuration.

The first two steps are essential for preparing the matching and are discussed in this chapter.

5.2.1   Determination of β^*

Compared to the ALFA/TOTEM high β^*-optics, the achievable β^*-value for ALICE is rather limited, due to the small bunch spacing and the large required separation of $\Delta y = 12\,\sigma$. In order to determine the achievable β^*-value, certain assumptions must be made. A very important factor for the calculation of the beam separations is the beam emittance. For these calculations, the conservative emittance from the LHC Design Report is assumed [B$^+$04]. Hence, the calculated β^*-values are only lower limits. Since the protons at LHC energies are moving very closely to the speed of light, the distance of the potential bunch-bunch encounters as a function of the bunch spacing s_b (in units of time) can be approximated by

$$d_{bb}(s_b) \approx \frac{c}{2\,s_b}\,. \tag{5.5}$$

Using this relation, the potential bunch encounters are separated by

$$d_{bb}(50\,\text{ns}) = 7.48\,\text{m}\,, \qquad d_{bb}(25\,\text{ns}) = 3.48\,\text{m}\,. \tag{5.6}$$

Knowing that the relevant beam encounters lie inside the inner triplet region (after the triplet, the separation/recombination dipoles are installed), the β-function at the position of the first

beam encounter after the IP can be calculated using Eq. 2.48. If dispersive effects are neglected, the transverse beam dimensions at this encounter are given by

$$\sigma(d_{bb}) = \sqrt{\epsilon\,\beta(d_{bb})} = \sqrt{\epsilon}\,\sqrt{\beta^* + \frac{d_{bb}^2}{\beta^*}}\,. \tag{5.7}$$

At the first encounter, the crossing angle θ_C leads to a vertical beam-beam separation of

$$\Delta y(d_{bb}) = 2\,d_{bb}\,\tan\left(\pi\,\theta_C\right)\,. \tag{5.8}$$

With the required separation S_r (in terms of σ) at the first encounter, the following relation can be deduced

$$\frac{\Delta y(d_{bb})}{\sigma(d_{bb})} \geq S_r\,. \tag{5.9}$$

Finally, an implicit relation for the largest possible β^*-value as function of d_{bb}, the required separation S_r, the emittance and the available crossing angle is found

$$\beta^* + \frac{d_{bb}^2}{\beta^*} \leq \left(\frac{\Delta y(d_{bb})}{S_r\,\sqrt{\epsilon}}\right)^2\,. \tag{5.10}$$

Considering the required separation of $S_r = 12$, a normalized emittance of $\epsilon_N = 3.75\,\mu\text{m}\,\text{rad}$, an available full crossing angle of $\theta_C = 300\,\mu\text{rad}$, and the distance between the beam-beam encounters of Eq. 5.6, the following upper limits for the β^*-value are obtained

$$\beta^* \leq \begin{cases} 17.6\,\text{m} & \text{for } 25\,\text{ns}\,, \\ 56.0\,\text{m} & \text{for } 50\,\text{ns}\,. \end{cases} \tag{5.11}$$

Compatible optics with $\beta^* = 30\,\text{m}$ and $\beta^* = 18\,\text{m}$ have been derived for the two bunch spacings of 50 ns and 25 ns respectively. The slightly too large β^*-value for 25 ns compared to the value in Eq. 5.11 is chosen for convenience. However, both, the required separation and the emittance were chosen very conservatively, so the separation will most likely be sufficient. Nevertheless, the optics could be rematched if the value is considered to be too large. The impact on L, v, and $\Delta\psi$ due to such a rematch would be moderate.

In the following, the $\beta^* = 18\,\text{m}$ optics is discussed in detail, because it is compatible with the LHC design filling scheme with a bunch spacing of 25 ns. The $\beta^* = 30\,\text{m}$ optics are discussed only briefly.

5.2.2   Positioning of the Roman Pot Detectors

In the present set-up of the LHC, there are no Roman Pot detectors installed in the very forward region of IR2. For the matching of the IP-RP phase advance $\Delta\psi$, the detector positions must be assumed. For ATLAS-ALFA, the Roman Pot stations are installed at a longitudinal distance of $\pm147\,\mathrm{m}$ and $\pm220\,\mathrm{m}$ from the IP. The case of IR2 is slightly more complicated, because the injection magnets are installed in this region. First matchings, considering the RPs at a distance of $220\,\mathrm{m}$ from the IP, showed that the phase advance cannot be matched to the desired value of $\Delta\psi = 0.25$. Since the v-value is non-zero in this case, the precision of the reconstruction can be improved if the measurement takes place at two different locations [Sch12], which makes the installation of two detector stations advantageous. As shown in Fig. 5.1, on the ALICE A-Side, the RPs must be placed in a region which is not occupied by the injection magnets. Here, the regions at longitudinal distances of $-180\,\mathrm{m}$ and $-220\,\mathrm{m}$ from the IP are considered. On the ALICE C-side, the regions at distances of $150\,\mathrm{m}$ and $220\,\mathrm{m}$ from the IP are suitable for the installation of very forward detectors.

In Fig. 5.1, not all the elements in the IR are shown, so there is still the possibility of additional constraints, e.g. by vacuum elements. Once an optical configuration is existing, the most appropriate detector locations can also chosen by the positions with the largest L-values. The assumed detector locations are indicated by the black boxes in Fig. 5.1. According to the standard nomenclature of the elements in the LHC sequence, the two Roman Pot stations at $150\,\mathrm{m}$ and $220\,\mathrm{m}$ distance are labeled with RP1.R2B1 and RP2.R2B1, respectively. Correspondingly, the stations on the left hand side are labeled with RP1.L2B2 and RP2.L2B2.
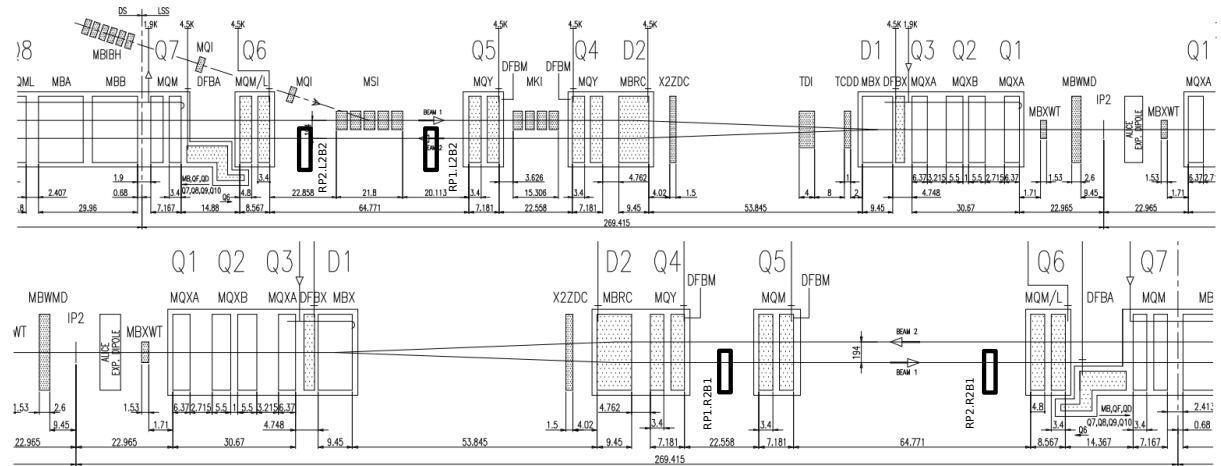
Figure 5.1: Inner part of IR2, together with the considered detector positions on the ALICE A-Side (top) and C-Side (bottom). Note that this drawing is not to scale. Drawing from [B$^+$04].

5.2.3 Optics Matchings

Table 5.1: Boundary conditions for the optics matchings by means of MAD-X.

Quantity	β_x	β_y	α_x	α_y	η_x	η'_x
Unit	[m]	[m]			[m]	10^{-2}
			Beam 1			
Start of DS Left	168.7	35.09	-2.407	0.571	1.961	2.818
IP	β^*	β^*	0	0	0	0
End of DS Right	31.42	172.2	-0.515	2.347	0.996	1.290
			Beam 2			
Start of DS Left	31.42	172.2	0.515	-2.347	0.996	-1.290
IP	β^*	β^*	0	0	0	0
End of DS Right	168.7	35.09	2.407	-0.571	1.961	-2.818

The boundary conditions of the optical parameters at the beginning and at the end of IR2 are shown in Table 5.1. These conditions must imperatively be fulfilled by the optics, which has to be taken into account during the matchings. In addition to the shown boundary conditions, the phase advance between the IP and the second RP station at $\pm 220\,\text{m}$ is matched to

$$\Delta\psi = \begin{cases} 0.34 & \text{for } \beta^* = 18\,\text{m} \\ 1/3 & \text{for } \beta^* = 30\,\text{m} \end{cases}. \tag{5.12}$$

These values have not been chosen arbitrarily, but several matchings showed that these phase advances are the smallest ones that can be reached with considerable magnetic strengths and B1/B2 current ratios. The corresponding phase advance of the nominal optics is approximately $\Delta\psi = 0.5$. A priori, constraints on the phase advance over the IR were not imposed. Different matching results were obtained by re-defining the allowed variable ranges or by limiting the β-functions at different positions in the IR. In the post-selection, only matchings with a penalty function of less than 10^{-19} were considered, and priority was given to the results which required the least external phase compensation. All matchings are done with all crossing, separation and spectrometer bumps switched off. The quadrupole currents which have been varied for the matching are summarized in Table 7.1. For the initialization, the LHC sequence and the LHC proton collision optics at $7\,\text{TeV}$ was loaded.

5.3   The $\beta^* = 18\,\text{m}$ Optics

From the many matching results, the solution with the most convenient properties was chosen. In particular, the presented optical solution was selected, because it combines a small penalty function, small required phase advance compensation, good left/right anti-symmetry, moderate quadrupole strengths, and admissible B1/B2 quadrupole strength ratios. The presented $\beta^* = 18\,\text{m}$ optics are discussed in detail in the following chapters.
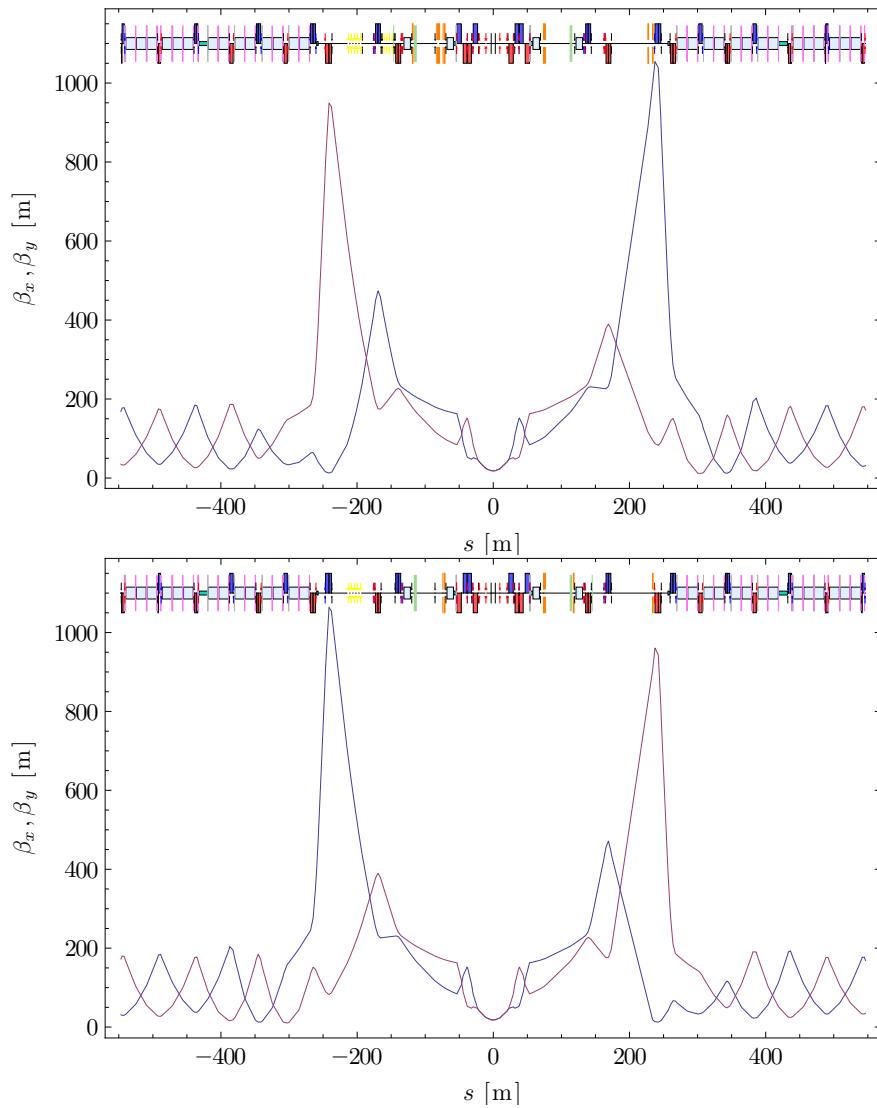
Figure 5.2: Horizontal (blue) and vertical (red) betatron functions of the $\beta^* = 18\,\text{m}$ configuration in IR2. Top: Beam 1, bottom: Beam 2. s is set to zero at IP2.

5.3.1 Optics Properties

Fig. 5.2 shows the β-functions of the $\beta^* = 18\,\mathrm{m}$ optics configuration. The optical functions are shown on a larger scale in Fig. 7.5 in the Appendix.

Both optics show significant peaks of the β-functions at Q6 on both sides of the IP (Beam 1 in vertical direction on the left side, and in horizontal direction on the right side; vice versa for Beam 2), which mainly results from the phase advance constraint to the second Roman Pot station, located right before Q6 on both sides. The largest β-values in the IR are in the order of $\beta =1000\,\mathrm{m}$, compared to $\beta = 300\,\mathrm{m}$ in the nominal configuration with $\beta^* = 10\,\mathrm{m}$. Therefore, the geometrical aperture with the new configuration must be examined.

The β-functions are symmetric with respect to Beam 1 and Beam 2, but are mirrored at the IP. Both individual configurations are roughly anti-symmetric with respect to β_x and β_y, which is necessary due to the quadrupole current ratio constraint.

Fig. 5.3 shows the periodic dispersion functions of the optics with all bumps in the machine switched off. Whereas the horizontal dispersion takes large values in the arcs and is zero at the IP, the vertical dispersion is always zero, due to the absence of vertical bendings in this configuration.

The relevant optical parameters for the measurement of very forward particles are summarized in Table 5.2. The configuration respects the boundary conditions on α, β, η_x, and η_x' at the beginning and the end of the IR (the vertical dispersion function η_y is not matched, because no vertical bendings are present in the considered machine configuration). In the regions of the DS, the β-functions are transferred into the periodic modulation by the FODO structure.
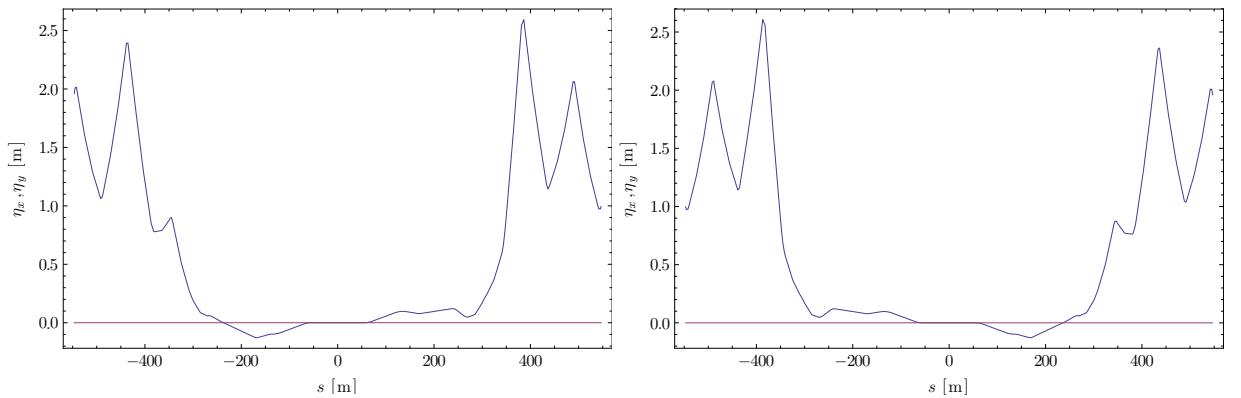
Figure 5.3: Periodic dispersion functions with all bumps in the machine switched off. Blue indicates η_x, red indicates η_y. Left: Beam 1, right: Beam 2.

Table 5.2: Optical parameters of the $\beta^* = 18\,\mathrm{m}$ optics which are relevant for the tagging of very forward protons. The beam sizes are calculated using the beam emittance of the LHC Design Report. The quantity ΔQ_{IR} defines the required external phase advance compensation.

		Beam 1		Beam 2	
Quantity	Unit	x	y	x	y
β^*	m	18.0	18.0	18.0	18.0
β_{RP1}	m	229.0	289.9	314.5	333.3
β_{RP2}	m	781.2	141.0	781.2	141.0
α_{RP1}		0.12	-2.64	-4.48	3.00
α_{RP2}		-7.17	1.80	-7.17	1.80
ΔQ_{IR}		0.4754	0.4567	0.4676	0.4534
$\Delta\psi_{\mathrm{RP1}}$		0.3073	0.2968	0.3271	0.3104
$\Delta\psi_{\mathrm{RP2}}$		0.3400	0.3400	0.3400	0.3400
σ_{RP1}	μm	341.4	382.1	403.0	419.1
σ_{RP2}	μm	631.6	267.5	634.8	272.3
L_{RP1}	m	60.0	69.1	66.6	71.9
L_{RP2}	m	100.1	42.5	100.1	42.5

5.3.2 Quadrupole Configuration

With the presented $\beta^* = 18\,\mathrm{m}$ configuration, all quadrupole currents fulfill the requirements. The currents in terms of k are given in Table 7.1 in the Appendix, whereas the relative currents in terms of % of the nominal strengths are given in Table 5.3.

The largest relative quadrupole strength is reached for KQ9.L2B2 with 90% of the nominal current. The triplet strength KQX.L2 is reduced to 77.8% of the nominal strength. Contrary to the nominal optics, the triplet trims are not set to zero in this configuration (see Table 7.1).

The quadrupole current ratios of the two quadrupole channels are shown in Table 5.3 as well. The largest ratio is $R_{12} = 1.73$ for Q8 right of IP2, leaving a large enough flexibility for operation.

Table 5.3: Relative quadrupole currents for the ALICE $\beta^* = 18\,\mathrm{m}$ configuration. The right column gives the normalized current ratio of the two quadrupole channels (the ratio is not calculated for the independent trim quadrupoles and for the triplet currents).

| Beam 1		Beam 2		
Rel. Strength	Strength Label	Rel. Strength	Strength Label	R_{12}
51.6 %	KQT13.L2B1	62.9 %	KQT13.L2B2	-
85.2 %	KQT12.L2B1	77.2 %	KQT12.L2B2	-
13.5 %	KQTL11.L2B1	84.9 %	KQTL11.L2B2	-
71.0 %	KQ10.L2B1	86.5 %	KQ10.L2B2	1.22
69.3 %	KQ9.L2B1	90.0 %	KQ9.L2B2	1.30
24.5 %	KQ8.L2B1	40.2 %	KQ8.L2B2	1.64
87.3 %	KQ7.L2B1	69.2 %	KQ7.L2B2	1.26
62.3 %	KQ6.L2B1	57.3 %	KQ6.L2B2	1.09
52.0 %	KQ5.L2B1	35.4 %	KQ5.L2B2	1.47
24.9 %	KQ4.L2B1	14.8 %	KQ4.L2B2	1.69
77.8 %	KQX.L2	77.8 %	KQX.R2	-
14.8 %	KQ4.R2B1	24.7 %	KQ4.R2B2	1.67
35.4 %	KQ5.R2B1	52.2 %	KQ5.R2B2	1.47
57.5 %	KQ6.R2B1	63.6 %	KQ6.R2B2	1.11
67.7 %	KQ7.R2B1	88.8 %	KQ7.R2B2	1.31
38.8 %	KQ8.R2B1	22.4 %	KQ8.R2B2	1.73
69.3 %	KQ9.R2B1	69.6 %	KQ9.R2B2	1.01
86.6 %	KQ10.R2B1	72.9 %	KQ10.R2B2	1.19
70.9 %	KQTL11.R2B1	16.0 %	KQTL11.R2B2	-
87.7 %	KQT12.R2B1	89.0 %	KQT12.R2B2	-
64.2 %	KQT13.R2B1	38.5 %	KQT13.R2B2	-

5.3.3   Betatron Phase Advance
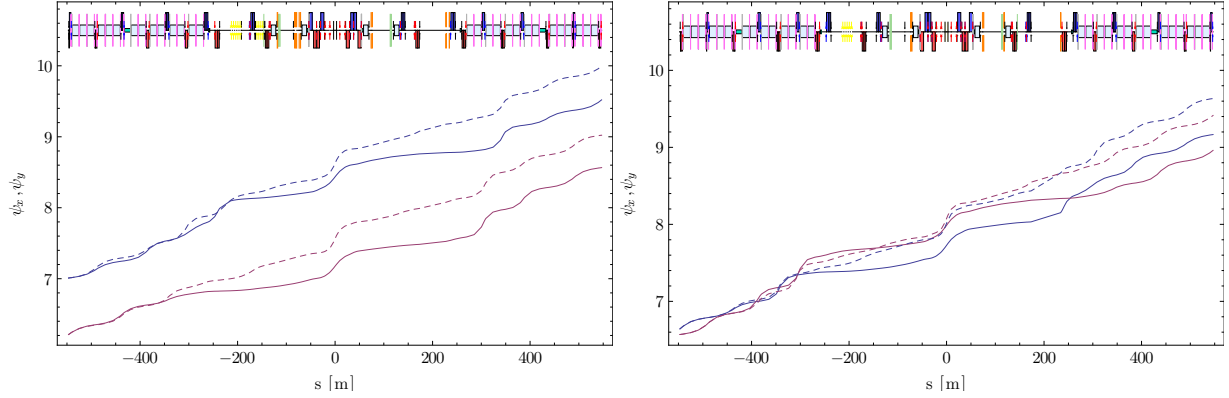
Figure 5.4: Betatron phase of the regular IR2 optics with $\beta^* =10$ m (dashed lines) and of the matched $\beta^* =18$ m optics (straight lines). Blue for ψ_x, red for ψ_y. Left: Beam 1, right: Beam 2.

In the $\beta^* = 18$ m configuration, the phase advance over the IR is strongly reduced with respect to the nominal optical configuration (see Fig. 5.4 for a comparison of the betatron phase evolution). The required external phase advance compensation in horizontal/vertical direction is

$$\Delta Q_{\mathrm{IR}}^{\mathrm{B1}} = 0.4754/0.4567\,, \qquad \Delta Q_{\mathrm{IR}}^{\mathrm{B2}} = 0.4676/0.4534\,. \tag{5.13}$$

As visible in Fig. 5.4, the main difference in the slope of the ψ-evolution occurs between the IP and Q6, so in the region where the phase advance was matched for the $\beta^* = 18$ m optics. Furthermore, this change appears on both sides of the IP for both beams, which is due to the required anti-symmetry of the β-functions with respect to the IP. The limiting factor in this case is the quadrupole current ratio limit. Due to this constraint, very non-symmetric solutions with larger IR phase advances had to be refused in the matching phase. This condition could be obsolete if additional cables would be installed at the power converters. Such an upgrade is currently in progress for the quadrupoles in IR1[1] [Bur13].

Strategies for external phase compensation are discussed in Chap. 5.6.

---

[1]However, the ATLAS-ALFA upgrade is not necessary to reduce the required phase advance compensation, but to make the implementation of the very high β^*-configurations ($\beta^* > 1000$ m) possible.

5.3.4   Crossing Angle and Luminosity

For the presented $\beta^* = 18\,\text{m}$ optics, a crossing angle was matched by means of MAD-X. Thanks to the simple relation in Eq. 3.5, the crossing bumps can be matched with the muon spectrometer magnet switched off. According to [B$^+$04], for protons at LHC design energy, a full crossing angle of $\theta_C = 300\,\mu\text{rad}$ (with spectrometer bump switched on) can be obtained. Following Eq. 3.5, this corresponds to a full external crossing bump of

$$\theta_\text{ext} = 160\,\mu\text{rad}\,. \tag{5.14}$$

The matching was done under the premise of a closed orbit ($y = 0$ at the beginning and at the end of the IR) and a vertical orbit of zero at the collision point. Furthermore, the two MCBXV magnets left and right of IP2 were under constraint to have the same currents with opposite sign. The calculated crossing scheme is shown in Fig. 5.5. As shown in Table 5.4, the required corrector magnet currents to achieve this crossing angle are well below the nominal currents. The existence of additional bumps in the machine leads to different periodic dispersion functions than those which have been previously shown. When the vertical bumps are switched on, the vertical dispersion function becomes considerable. Also, the horizontal dispersion function at the IP is no longer zero if the crossing bumps are switched on in other parts of the ring. The periodic dispersion with the $\beta^* = 18\,\text{m}$ optics, the shown crossing scheme, and the remaining crossing and spectrometer bumps switched on (the tune is not compensated, so Q is reduced by ΔQ_IR) is shown in Fig. 5.6. The peak excursions of the beam orbits are in the order of $\pm 3\,\text{mm}$.
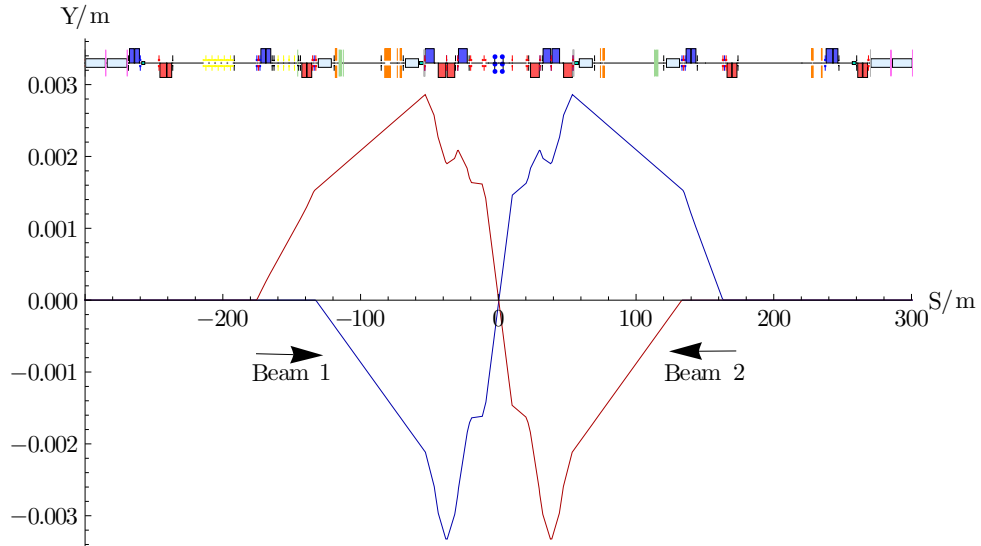

Figure 5.5: Total vertical crossing scheme in IR2 with spectrometer bump switched on, for a full crossing angle of $\theta_C = 300\,\mu\text{rad}$. Blue: Orbit of Beam 1, red: Orbit of Beam 2.

Table 5.4: Orbit corrector strengths for the $300\,\mu$rad crossing angle for the $\beta^* = 18\,$m optics.

	Magnet Name	Type	Nom. Field/T	B/T
Beam 1	MCBYV.A4L2.B1	MCBYV	3.00/2.50 [a]	-0.6905
	MCBYV.4R2.B1	MCBYV	3.00/2.50 [a]	-1.1280
	MCBCV.A5R2.B1	MCBCV	3.11/2.33 [a]	1.3353
	MCBXV.1L2	MCBXV	3.26	2.2778
	MCBXV.1R2	MCBXV	3.26	-2.2778
Beam 2	MCBYV.B5L2.B2	MCBYV	3.00/2.50 [a]	1.0079
	MCBYV.4L2.B2	MCBYV	3.00/2.50 [a]	-0.7019
	MCBYV.A4R2.B2	MCBYV	3.00/2.50 [a]	-0.6905

[a] At a temperature of $1.9\,$K/$4.5\,$K.
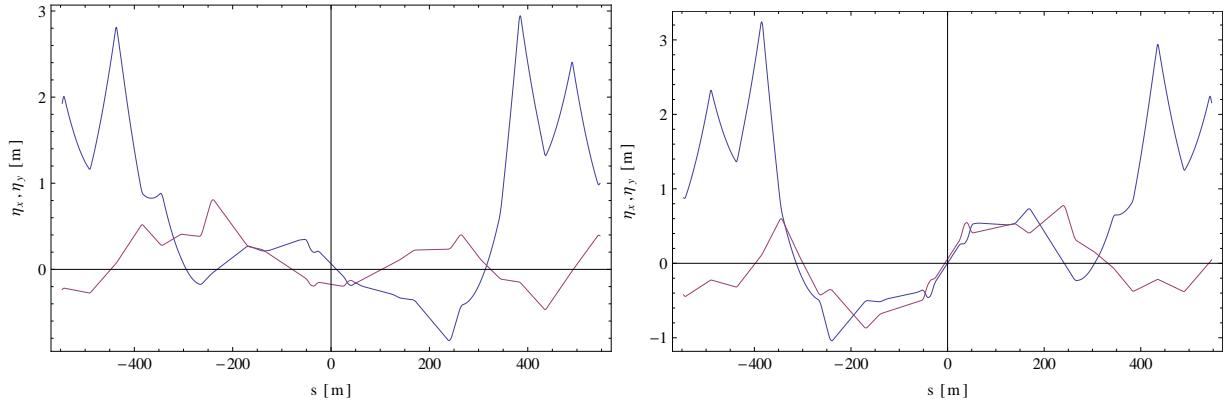
Figure 5.6: Periodic dispersion of the $\beta^* = 18\,$m optics with all crossing and spectrometer bumps switched on (tune not matched). Blue: η_x, red: η_y. Left: Beam 1, right: Beam 2.

The crossing angle of the nominal collision optics is $\theta_C = 175.8\,\mu$rad. Following Eq. 2.54 and Eq. 2.57, the instantaneous luminosity in IR2 with the $\beta^* = 18\,$m optics, is reduced with respect to the nominal optics by a factor of

$$\mathcal{L}_{18}/\mathcal{L}_{10} = 0.56\,, \tag{5.15}$$

The required reduction to match the detector requirements would be in the order of 10^{-2}. Therefore, the luminosity must still be scaled, as discussed in [Mor01].

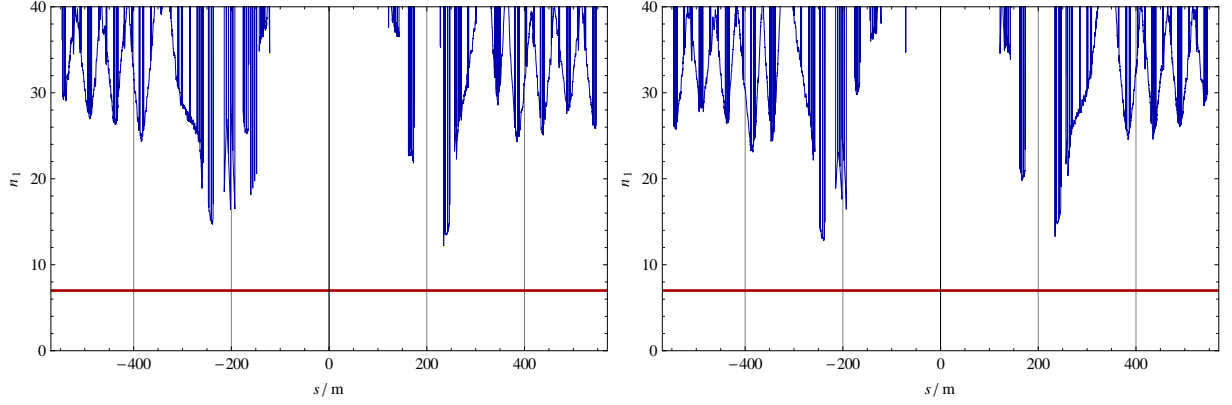### 5.3.5   Geometrical Acceptance

Figure 5.7: Aperture in terms of n_1 for the whole IR, calculated for a beam energy of 7 TeV, using the Design Report emittance and all crossing bumps and spectrometer bumps switched on. The red line indicates the limit of $n_1 = 7$. Left: Beam 1, right: Beam 2.

The geometrical acceptance of the $\beta^* = 18\,$m optics is shown in terms of n_1 in Fig. 5.7. For the calculations, the considered beam energy is 7 TeV and the Design Report emittance is used. All crossing and spectrometer bumps are switched on. The considered crossing bump is the $\theta_c = 300\,\mu$rad crossing scheme which was shown in the previous chapter. The smallest values of n_1 occur at the positions where the β-functions are extreme, which is in the centre of Q6 on both sides of the IR. The smallest n_1-values are $n_1 = 13$ for Beam 1 at Q6 right of IP2 and $n_1 = 14$ for Beam 2 at Q6 left of IP2. Since all the values are well beyond the limit of $n_1 = 7$, the $\beta^* = 18\,$m optics are considered to be safe. Note that the presented n_1-values are still conservative because:

- The worst case emittance is considered, so the beam sizes are overestimated.

- The tune is not compensated, which leads to larger dispersion functions.

- The largest possible crossing angle is taken into account.

In the triplet and detector region (± 23 m from the IP), the aperture is well-beyond $n_1 = 40$. Existing plans for the upgrade during LS2 envisage the installation of a smaller beam pipe, which would reduce the available aperture. This region is studied in detail, with both, the old and the new ALICE beam pipe, in Chap. 7.1.

5.3.6   Optical Length and Local Dispersion
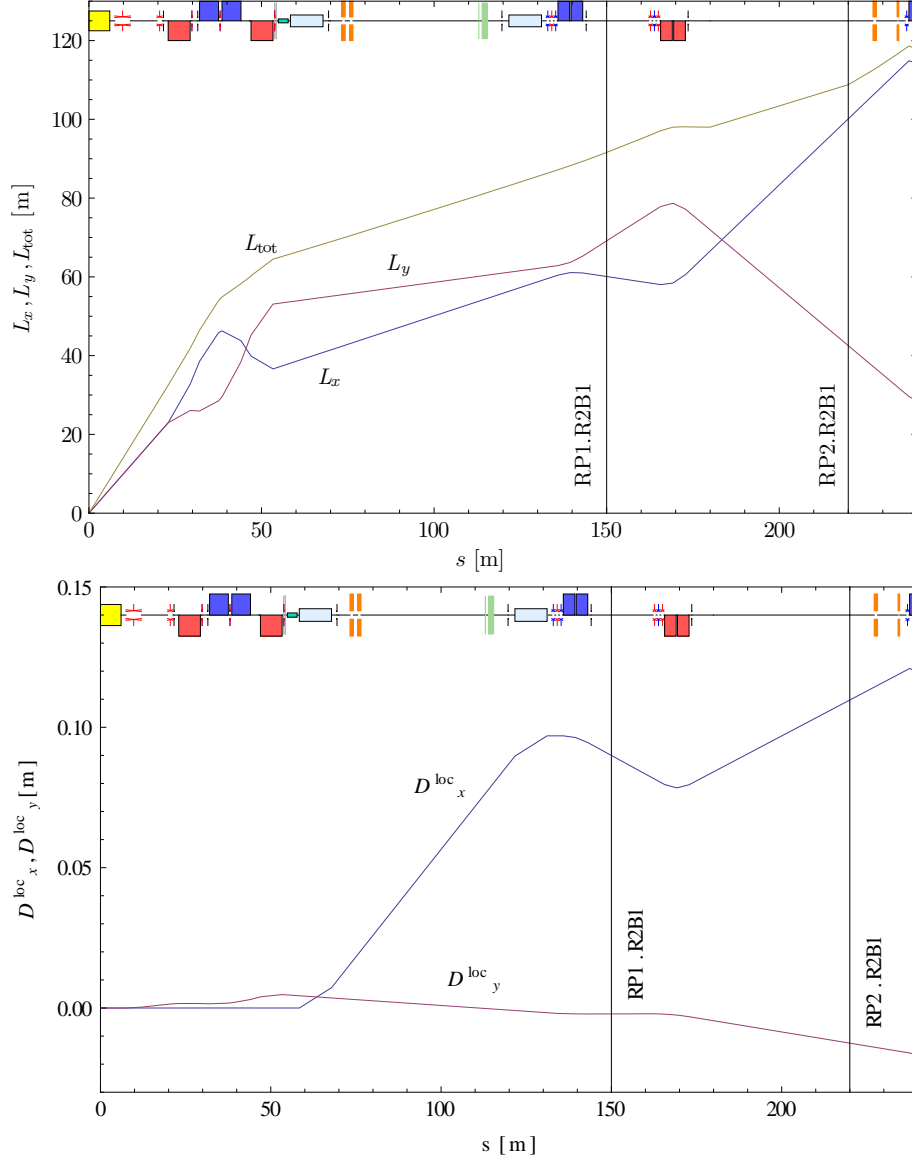
Figure 5.8: Top: Optical length of the $\beta^* = 18\,\mathrm{m}$ optics for both transverse directions of Beam 1 at the ALICE C-side. Bottom: Local dispersion functions of Beam 1 for the ALICE C-side. The position $s = 0$ indicates the IP.

The two important quantities for the measurability at very low $|t|$-values and for a good resolution of $\xi = \frac{\Delta p}{p}$ are the optical length L and the local dispersion function D^{loc}. The evolution of the optical length and the local dispersion in both transverse directions is shown for Beam 1

at the ALICE C-side in Fig. 5.8. Using this information, the best possible detector locations for the measurement can be determined. For RP2.R2B1, the best detector location would be as closely as possible to Q6, because the L_{tot}-function[2] is continuously rising.

For the first RP station RP1.R2B1, a position closely to Q5 should be chosen. Furthermore, the detector should preferably be placed behind the quadrupole, to have the largest possible L_{tot}-function at the RP station. Besides, studies on the detector resolution in different scenarios show that such a placing would be advantageous, because the angle of incidence can be measured more accurately, if the two RP stations are not separated by a quadrupole [Sch12]. The dispersion is calculated with the crossing bump and spectrometer bump switched on. As shown, the dispersion functions take values of up to $D_x^{\text{loc}} = 12\,\text{cm}$, so the dependency of the position on the fractional momentum loss is small. Since the optics for Beam 2 are matched with the same conditions on the phase advance between IP and RP2.L2B2, the optical length and the dispersion functions on the left hand side are exactly identical but mirrored with respect to the IP. The evolution of L and D^{loc} on the left hand side is therefore not shown. However, for the acceptance calculations, the two sides are considered separately because the RPs are placed at different positions.

5.4 The $\beta^* = 30\,\text{m}$ Optics
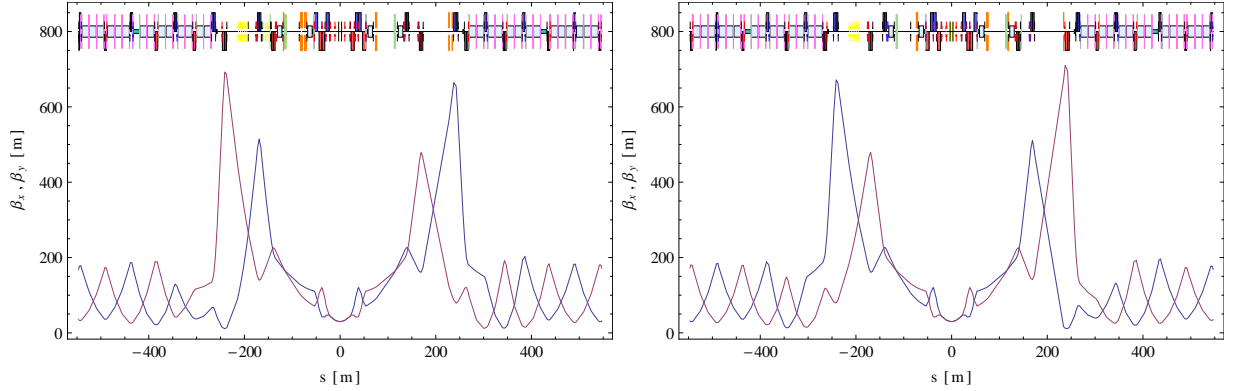
Figure 5.9: Betatron functions of the $\beta^* = 30\,\text{m}$ configuration in IR2. Blue indicates β_x, red indicates β_y. Left: Beam 1, right: Beam 2.

The very optimistic extreme for a high β^*-configuration in IR2 has a value of $\beta^* = 30\,\text{m}$. This configuration could be implemented for a bunch spacing of $50\,\text{ns}$ or if very small emittances could be reached. As mentioned, the phase advance from IP to RP2 was matched to $\Delta\psi = 1/3$

---

[2]The total optical length L_{tot} is given by $L_{\text{tot}}^2 = L_x^2 + L_y^2$.

in both transverse planes for both beams. The β-functions are shown in Fig. 5.9.

This configuration requires an external phase advance compensation of

$$\Delta Q_{\mathrm{IR}}^{\mathrm{B1}} = 0.466/0.414 \,, \quad \Delta Q_{\mathrm{IR}}^{\mathrm{B2}} = 0.486/0.431 \,. \tag{5.16}$$

The limitations on the quadrupole gradients are fulfilled, except the slightly too large powering at Q12 left of IP2 for Beam 1 which is powered at 91.6% of the nominal strength. However, this is still tolerable because exceeding the initial limitation only occurs for one magnet. The peaks of the betatron functions at Q6 are smaller than for the $\beta^* =18\,\mathrm{m}$ optics, which reduces the acceptance but could not have been solved by rematchings. Thanks to this, the geometrical aperture in terms of n_1 is even better than for the $\beta^* =18\,\mathrm{m}$ optics. An exception is the region around the IP, where the β-functions are larger (see Chap. 7). The crossing scheme is the same as for the $\beta^* = 18\,\mathrm{m}$ optics. The optical lengths at the detector positions are for x/y

$$L^{\mathrm{RP1.B1}} = 75.8/90.0 \ \mathrm{m} \,, \qquad L^{\mathrm{RP2.B1}} = 105.7/59.2\,\mathrm{m} \,, \tag{5.17}$$

$$L^{\mathrm{RP1.B2}} = 73.0/103.3\,\mathrm{m} \,, \qquad L^{\mathrm{RP2.B2}} = 105.7/59.2\,\mathrm{m} \,, \tag{5.18}$$

which is slightly better than for the $\beta^* = 18\,\mathrm{m}$ configuration. More details on this configuration can be found in [HS13]. The quadrupole strengths of the $\beta^* = 30\,\mathrm{m}$ optics are given in Table 7.1.

5.5   Beam-Beam Separation

The optics shown in the previous chapters, combined with the matched crossing angle, can be evaluated for the beam-beam separation. It is useful to introduce a normalized beam-beam separation in terms of the largest RMS beam size [VJ12]

$$\Sigma_N = \frac{r_{12}}{\max(\sigma_{x12}, \sigma_{y12})} \,, \tag{5.19}$$

where r_{12} is the distance of the beam centres and $\max(\sigma_{x12}, \sigma_{y12})$ is the largest RMS beam size, depending on the transverse direction in which one beam is largest. Severely, this quantity must be calculated for both beams (which is implied by the index $x12$), but thanks to the fact that the behavior in the inner triplet region is exactly identical for both beams, it is sufficient to consider the maximum σ of the two transverse directions for one beam.

The normalized separation of the two beams in the inner triplet region is shown in Fig. 5.10. Outside of this region, the two beams start moving in different beam pipes. For both configurations, the smallest separation occurs at the first beam-beam encounter and is well beyond $15\,\sigma$ for all other encounters. Thanks to the larger bunch spacing, considered for the $\beta^* =30\,\mathrm{m}$ optics, the separation at the first encounter for this case is more than $\Sigma_N = 16\,\sigma$. For the $\beta^* =18\,\mathrm{m}$ optics, the separation is $\Sigma_N = 11.6\,\sigma$ at the first encounter.
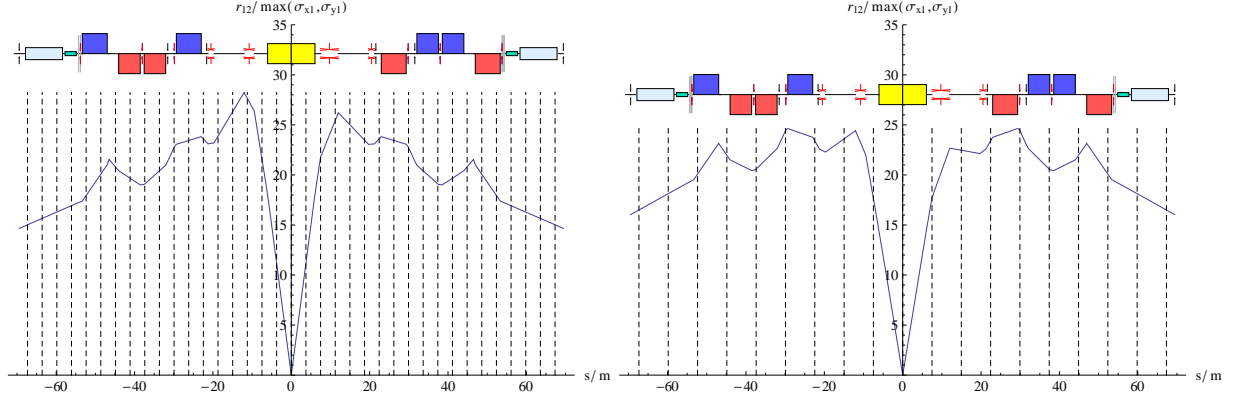
Figure 5.10: Normalized beam-beam separation for the β^* =18 m optics (left) and for the β^* =30 m optics (right). The dashed lines indicate the potential bunch encounters. The considered bunch spacing is 25 ns for $\beta^* = 18$ m and 50 ns for $\beta^* = 30$ m. The IR2 crossing angle is $\theta_C = 300 \mu$rad. The beam emittance of the LHC Design Report was used.

The long range beam-beam tune shift parameter is calculated for both configurations, according to Eq. 2.52. The calculated parameters are listed in Table 5.5 in comparison to the nominal ALICE configuration with $\beta^* = 10$ m. As shown, the long range tune shift parameters are smaller than for the nominal configuration. For the β^* =30 m optics, the difference comes from the fact that the considered bunch spacing is different. For the β^* =18 m optics, this results from the conservative assumption of the required separation and the resulting very large crossing angle. Regarding the rule of thumb that a configuration is safe if the tune shift parameter is $\xi^{bb} < 10^{-3} - 10^{-4}$, the two considered configurations have enough separation. If the considered crossing angle is used, there is even some margin for a larger β^*-value, if only this parameter is taken as reference. However, this should be handled with care, because not all beam-beam interactions are taken into account with this parameter.

Table 5.5: Long range beam-beam tune shift parameters for different configurations.

β^*	s_{bb} (ns)	θ_C (μrad)	ξ^{bb}
10	25	175.8	$9.9 \cdot 10^{-5}$
18	25	300	$5.5 \cdot 10^{-5}$
30	50	300	$2.4 \cdot 10^{-5}$

5.6   Phase Advance Compensation

5.6.1   General Considerations

In comparison to the nominal optics with $\beta^* = 10\,\text{m}$, the two presented optics for ALICE have significantly different phase advances across the IR. At high-intensity operation, this phase advance has to be compensated in half of the LHC ring, between IP1 and IP5. One very important reason for the large phase difference between the nominal optics and the high β^*-optics is the matching of the phase advance between IP and the second RP location. A direct comparison of the phase advances between the IP and Q6, which is located in a distance of $\approx 230\,\text{m}$ from the IP, is shown in Table 5.6. Due to the quadrupole current ratio constraint and the related anti-symmetry of the β-functions with respect to the IP, approximately the same phase advance reduction occurs at the other side of the IP.

Phase advance compensations are required for the implementation of the TOTEM and ALFA optics as well, but the amount is much smaller than for the ALICE high β^*-optics. To make the IRs comparable, the IP-Q6 phase advance $\Delta\psi^{\text{Q6}}$ of the nominal optical configuration in IR5 is compared with the $\beta^* = 90\,\text{m}$ optics as well[3]. As shown in Table 5.6, the difference between the nominal $\beta^* = 0.55\,\text{m}$ optics and the $\beta^* = 90\,\text{m}$ optics in IR5 is very low compared to the difference between the $\beta^* = 10\,\text{m}$ optics and the $\beta^* = 18\,\text{m}$ optics for ALICE.

Several approaches for external tune compensation are discussed in the following.

Table 5.6: Comparison between the phase shifts $\Delta\psi^{\text{Q6}}$ between IP and Q6 and the required phase advance compensations ΔQ for different configurations in IR2 and IR5.

	IR5			IR2	
β^* (m)	$\Delta\psi_x^{\text{Q6}}$	$\Delta\psi_y^{\text{Q6}}$	β^* (m)	$\Delta\psi_x^{\text{Q6}}$	$\Delta\psi_y^{\text{Q6}}$
0.55	0.54	0.28	10.0	0.55	0.52
90.0	0.51	0.25	18.0	0.35	0.35
β^* (m)	ΔQ_x	ΔQ_x	β^* (m)	ΔQ_x	ΔQ_x
0.55	0.00	0.00	10.0	0.00	0.00
90.0	0.23	0.06	18.0	0.48	0.46

---

[3]Q6 is located at approximately 230 m distance from the IP for both regions, IR2 and IR5.

5.6.2 Global Compensation

In global compensation techniques, the quadrupoles of the periodic FODO lattice (see Chap. 2.3.3) in the LHC arcs are used to obtain a larger phase advance in these regions. Following Eq. 2.44, the phase advance can be varied by changing the focal length f, so the strengths of the quadrupoles are increased, which leads to reduced betatron functions and an increased phase advance. This approach is the standard technique during the implementation of the TOTEM and ALFA high β^*-optics. Thanks to the smaller β-values in the arcs, this method does not imply any problems with the aperture. In analogy to the nominal LHC cycle, in high β^*-operation, the beams are ramped and finally un-squeezed to the aimed optical configuration (see Chap. 3.4.2). The phase advance compensation is continuously applied during the un-squeeze. Thanks to the large size of the arcs, this method is applicable for even large phase advance compensations. The tunability range of the arcs was subject to theoretical studies [A+08] and is shown for the whole ring in Fig. 5.11. The tunability of half of the ring can be extraploated by this illustration. However, the study was done only for distinct settings and could be repeated to match the requirements of the presented optics. According to Fig. 5.11, with the arcs in the whole LHC ring, a simultaneous compensation of $\Delta Q \approx 0.75$ can be reached in both transverse directions.

5.6.3 Rematching of IR4

As shown before, the IR4 optics are not limited by serious constraints [A+08], so this IR gives some flexibility in terms of phase advance. The limiting factor in terms of tunability is the available aperture, which is more tight at injection due to the larger emittance. Former studies have discussed the tuneability of IR4 [B+04, A+08]. As a result of these studies, the tunability of this IR is summarized for injection and collision energy as shown in Fig. 5.11. As expected, the flexibility at injection is less then at LHC design energy. However, it is safer to vary the configuration before injection, since the beam instrumentation imposes tight limits and is fragile for damaging [Gio12]. Rematches of the IR4 optics have been realized to compensate the phase difference of the TOTEM $\beta^* = 90\,\mathrm{m}$ optics. The rematched optics are shown in Fig. 5.12. For these configurations, the peaks of the β-functions, compared to the nominal configuration are larger, but also the minima are lower which effectively increases the phase advance. The illustrated limitation at injection is based on the LHC design emittance. With smaller emittances, the achievable compensation is larger, so the indicated boundaries are conservative.
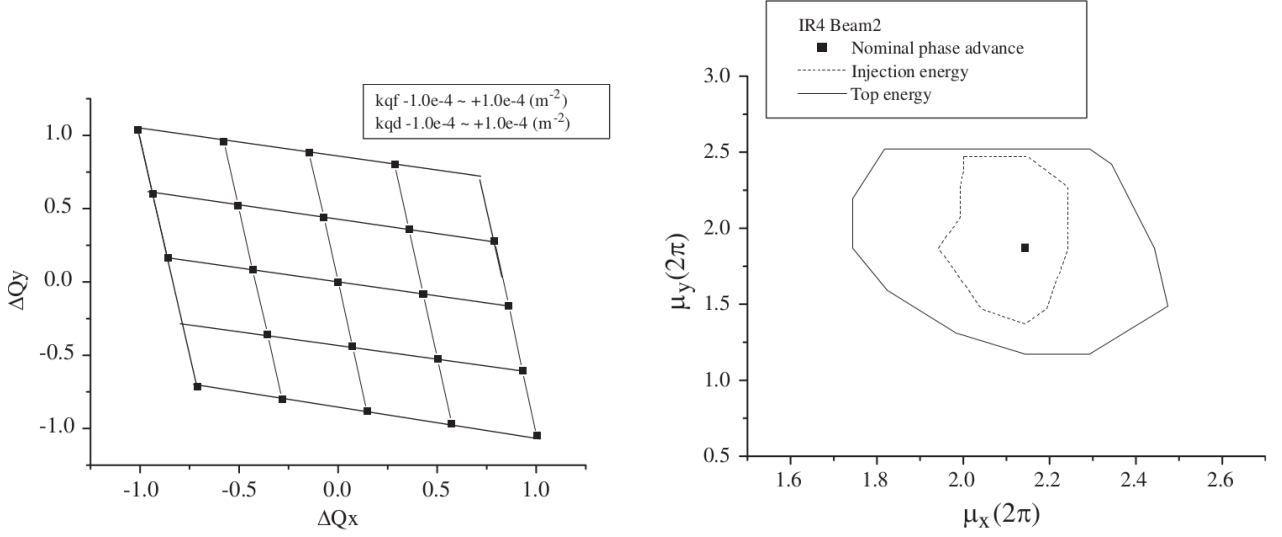
Figure 5.11: Left: Tunability range of the main arcs for global tune compensation. Right: Tunability of IR4 at injection energy (dashed line) and at LHC design energy (straight line). The phase advance is denoted by $\mu = 2\pi\psi$ in this case. The regular phase advance across the IR is $\Delta\psi_x^{IR}/\Delta\psi_y^{IR} = 2.143/1.870$ in horizontal/vertical direction [A$^+$08].
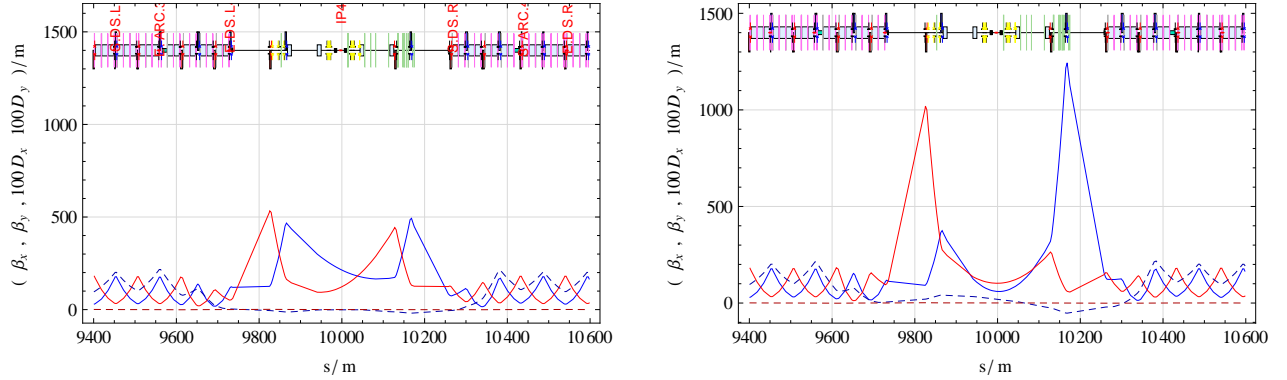

Figure 5.12: Left: Nominal IR4 optics for Beam 1 in collision mode. Right: Rematched optics with an increased phase advance by $\Delta Q_{x/y} = 0.22/0.05$ for tune compensation of the TOTEM/ALFA $\beta^* = 90\,\text{m}$ optics [BW10] (global LHC coordinates, the periodic dispersion is denoted by D in this case). Blue: β_x, red: β_y, blue dashed line: η_x, red dashed line: η_y.

5.6.4 Perspectives

Based on the presented tunability ranges, it can be seen that the required phase compensation could in principle be done if the rematchings of the arcs and IR4 are combined. However, the potential of the two methods is pushed close to the limits. If necessary, the phase advance over the IR could be changed which would affect the acceptance for low $|t|$-values.

The different optics in IR4 at injection energy would imply an increased phase advance which would have to be compensated by larger β-functions in the arcs. Since the IP1-IP5 phase advance constraint is only imposed in the collision mode, this compensation could be done globally, so the changes of the β-functions in the arcs would be moderate. However, the aperture due to this change would have to be evaluated.

In conclusion, the implementation of the optics requires additional studies for phase advance compensation. A detailed analysis would take into account different emittance scenarios and would analyze the tunability of the arcs in half of the ring in the $\Delta Q_x / \Delta Q_y$ region of interest. Such a study will require a significant amount of time and will only be worthwhile if ALICE decides to pursue the high β^*-project.

6.   Detector Acceptance

Introduction

Based upon the presented optical configurations, the detector acceptance for very forward particles can be calculated. This gives information about the measurability of scattered particles as a function of $|t|$ and ξ. The results of these calculations depend on numerous assumptions which are indicated for each acceptance distribution. Different parameter sets for the acceptance calculations are discussed and compared.

6.1   Approach

As part of this thesis, two tracking algorithms for the acceptance simulation have been implemented independently, in collaboration with R. Schicker. The algorithms are based on the two different platforms Wolfram Mathematica [Tro04] and C [RKL75], which gives the possibility to cross-check the simulation algorithms for their correctness. Using the same accelerator settings as input, both algorithms reproduce the same detector acceptances as a function of $|t|$ and ξ. The general structure of one simulation at a given $|t|$ and ξ is:

1. Definition of the diffractive parameters $|t|$ and ξ and of the number of particles n_{IP}.

2. Generation of the particle position in a Gaussian distribution as a function of the RMS beam size at the IP. Creation of a random azimuthal angle, and calculation of the resulting θ_x^* and θ_y^* for the given value $|t|$ and ξ.

3. Transport of the particle from the IP to the two RP detector positions by using the known matrix elements of the respective optical configuration.

4. Increase a counter if the particle is within the acceptance of both detectors.

5. Repeat the points 2. to 4. for a number of n_{IP} particles. The number of detected particles at fixed $|t|, \xi$ is defined as $n_d(|t|, \xi)$.

6. Calculate the acceptance for the given $|t|, \xi$ by

$$\mathcal{A}(|t|, \xi) = \frac{n_d(|t|, \xi)}{n_{\mathrm{IP}}} . \tag{6.1}$$

The properties of several parameters which are of importance for the acceptance simulations are only vaguely known. Therefore, the corresponding properties are assumed, based on empiric information or guesses. The following passages give a brief overview over the relevant parameters with the assumed properties.

Detector Geometry   The geometry of the Roman Pot detectors plays a significant role for the measurement. As shown in Fig. 4.5, the detectors used for TOTEM and ALFA host two vertical and one horizontal edgeless silicon sub-detector. The detector in the horizontal plane is installed on the outer part of the two beam pipes (see Fig. 4.7).

In the high β^*-configurations for TOTEM and ALFA, the phase advances are matched to $\Delta\psi_y = 0.25$ in the vertical and $\Delta\psi_x = 0.5$ in the horizontal plane, so the optics are parallel-to-point focusing in the vertical plane and point-to-point focusing in the horizontal plane [Hin08]. The latter configuration is independent of the scattering angle and only depending on the initial position. In vertical direction, the scattering angle is projected into an amplitude y, which is scaled by the optical length L_y. For a given $|t|$-value, the particles in vertical direction are equally distributed and have the largest amplitude if $\theta_x^* = 0$. The horizontal distribution is a Gaussian, scaled by the factor v_x. For a given value of ξ, this distribution is horizontally shifted, depending on the local dispersion function D_x^{loc}. Since the local horizontal dispersion is always of the same sign, the installation of a second horizontal detector is unnecessary. The particle tracks on the detector with such a configuration is shown on the left panel of Fig. 6.1.

The ALICE high β^*-optics, however, were not matched to these phase advances. The particles with given $|t|$-value hit the detector in an elliptic distribution, as shown in the right panel of Fig. 6.1. Therefore it would be advantageous to have horizontal measurements on both beam sides. For the acceptance simulations, a Roman Pot with two detectors in the horizontal plane is considered (see Fig. 6.1). However, it is not yet known if such a device is producable.

Detector Distance from Beam Centre   The minimum distance of the detector to the beam centre has a large impact on the acceptance. As a general guideline for high-intensity pp-operation, the Roman Pots must be retracted by $3\,\sigma$ with respect to the TCTs [Sch12]. The TOTEM detectors are allowed to be moved to a distance of $14\,\sigma$ to the beam centre in high-intensity operation [Dei12]. This distance is considered for the ALICE acceptance calculations as well. The impact of different detector distances is discussed.
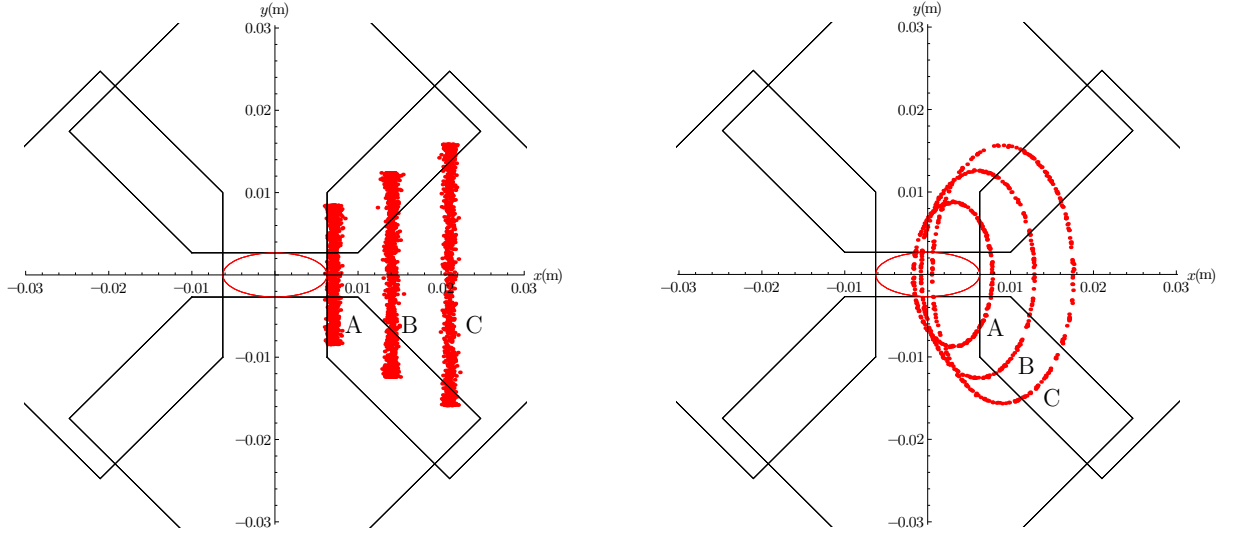
Figure 6.1: Particle hits in the edgeless silicon detectors for three sets, A, B, and C of $|t|,\xi$-values, with $|t|_A < |t|_B < |t|_C$ and $\xi_A < \xi_B < \xi_C$. Left: Optics with $\Delta\psi_x = 0.5$ and $\Delta\psi_y = 0.25$. Right: Optics with $0.25 < \Delta\psi_{x,y} < 0.5$. The 10σ beam-profile is shown at the centre.

Emittance The edgeless silocon detectors are assumed to be at a distance of $14\,\sigma$ from the beam centre. This is a relative distance which depends on the beam emittance, as shown in Eq. 2.35. Thus, for the diffractive measurements, the smallest possible emittances are desirable.

Outer Boundaries and Beam Pipe Losses Particles with very large $|t|$-values have large amplitudes in x and y when they arrive at the RP station. The outer limit for the detectability of the particles is assumed to be at a distance of $2.9\,\mathrm{cm}$ from the beam centre. Furthermore, losses can occur in the beam pipe before the detector stations. These losses become significant for very large $|t|$ and ξ-values. In the presented simulations, those losses are not considered.

The *standard conditions* for the acceptance simulations are:

- The Design Report emittance at LHC design energy, $\epsilon_N = 3.75\,\mu\mathrm{m\,rad}$, is considered.

- The RPs are located at distances of $\Delta s = -180\,\mathrm{m}$ and $\Delta s = -220\,\mathrm{m}$ from the IP for Beam 2 and at distances of $\Delta s = +150\,\mathrm{m}$ and $\Delta s = +220\,\mathrm{m}$ from the IP for Beam 1.

- The edgeless silicon detectors in a Roman Pot are installed on both sides, in the horizontal and vertical plane. They are operated at a distance of $14\,\sigma$ from the beam centre.

- The outer limit for the detection is a distance of $2.9\,\mathrm{cm}$ from the beam centre. The beam pipe losses between IP and RP are not taken into account.

6.2   Acceptance Simulations

The acceptances of the different optical configurations are shown as a function of $|t|$ and ξ. The considered range for the fractional momentum loss is $0 \leq \xi \leq 0.10$. As shown in Fig. 5.8, the local dispersion of the $\beta^* = 18\,\mathrm{m}$ optics takes values up to $D^{\mathrm{loc}} = 0.12\,\mathrm{m}$. With a momentum loss of $\xi = 0.10$, this corresponds to an additional deviation from the ideal trajectory of $1.2\,\mathrm{cm}$. The LHC beam screen provides a horizontal aperture of approximately $47\,\mathrm{mm}$ in total [ADK04]. Therefore, particles with small $|t|$-values and a fractional momentum loss of $\xi < 0.1$ will most probably not be lost before the RP. Detailed studies on the particle losses between IP and detector could be done using the tracking module PTC [Sch05].

6.2.1   Nominal Collision Optics

The nominal ALICE optics are not optimized for very forward measurements. The acceptance rises very slowly with increasing $|t|$ (see Fig. 6.2). In order to be able to compare the acceptance of different optics to each other, the $|t|$-value with $\mathcal{A} = 50\%$, for $\xi = 0$, denoted by $|t|_{50\%}$, is considered as a reference. For the measurement on the ALICE A-side, this threshold is reached at $|t|_{50\%} \approx 18\,\mathrm{GeV}^2$, for the measurement on the ALICE C-side at $|t|_{50\%} \approx 13\,\mathrm{GeV}^2$. The acceptances of the two sides are different, which is can be explained by the different detector positions left and right and the rather non-symmetric optics at the standard configuration.
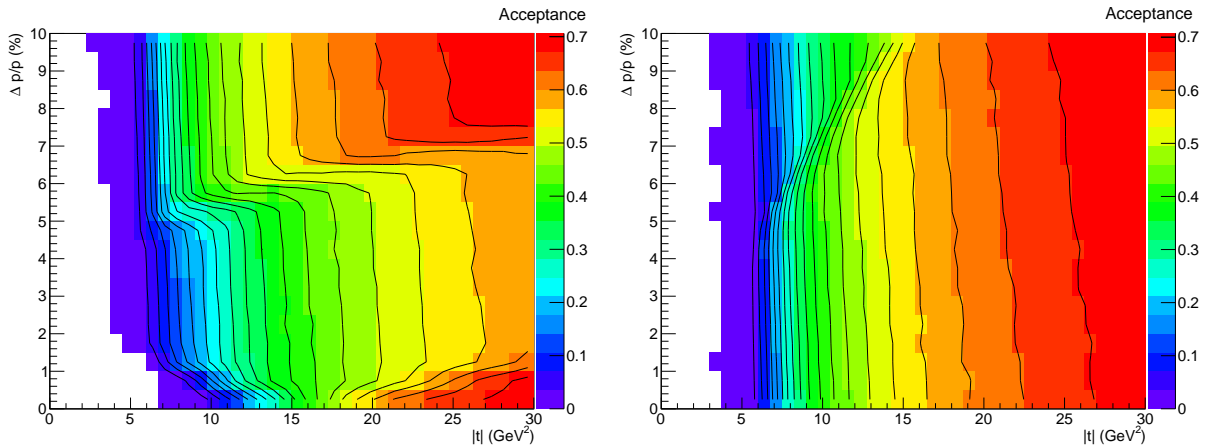

Figure 6.2: Proton acceptance for the nominal $\beta^* = 10\,\mathrm{m}$ optics as a function of $|t|$ and $\xi = \Delta p/p$. Left: Acceptance for the ALICE A-side (Beam 2), right: Acceptance for the C-side (Beam 1). Note the different scale of the z-axis with respect to the following acceptance distributions. The contour lines correspond to acceptance steps of 0.05.

6.2.2 The $\beta^* = 18\,\text{m}$ Optics

Fig. 6.3 shows the acceptance of the $\beta^* = 18\,\text{m}$ optics at the two sides of IP2. The reference of $\mathcal{A} = 50\%$ for elastic events is reached at $|t|_{50\%} = 0.44\,\text{GeV}^2$ on both, ALICE A-side and C-side. The acceptances of the two sides do not differ significantly. A region with an acceptance of $\mathcal{A} = 100\%$ is in a range of $0.7\,\text{GeV}^2 \leq |t| \leq 4.1\,\text{GeV}^2$ for elastic events. This region reaches over a broader range in ξ, for the measurements on the ALICE A-side. Due to the elliptic shapes of the particle distributions with given $(|t|, \xi)$, an acceptance of $\mathcal{A} = 100\%$ with small ξ-values can only be reached if the beam is instrumented on both sides in the horizontal direction. The acceptances with only one horizontal detector are discussed in Chap. 6.3.3.
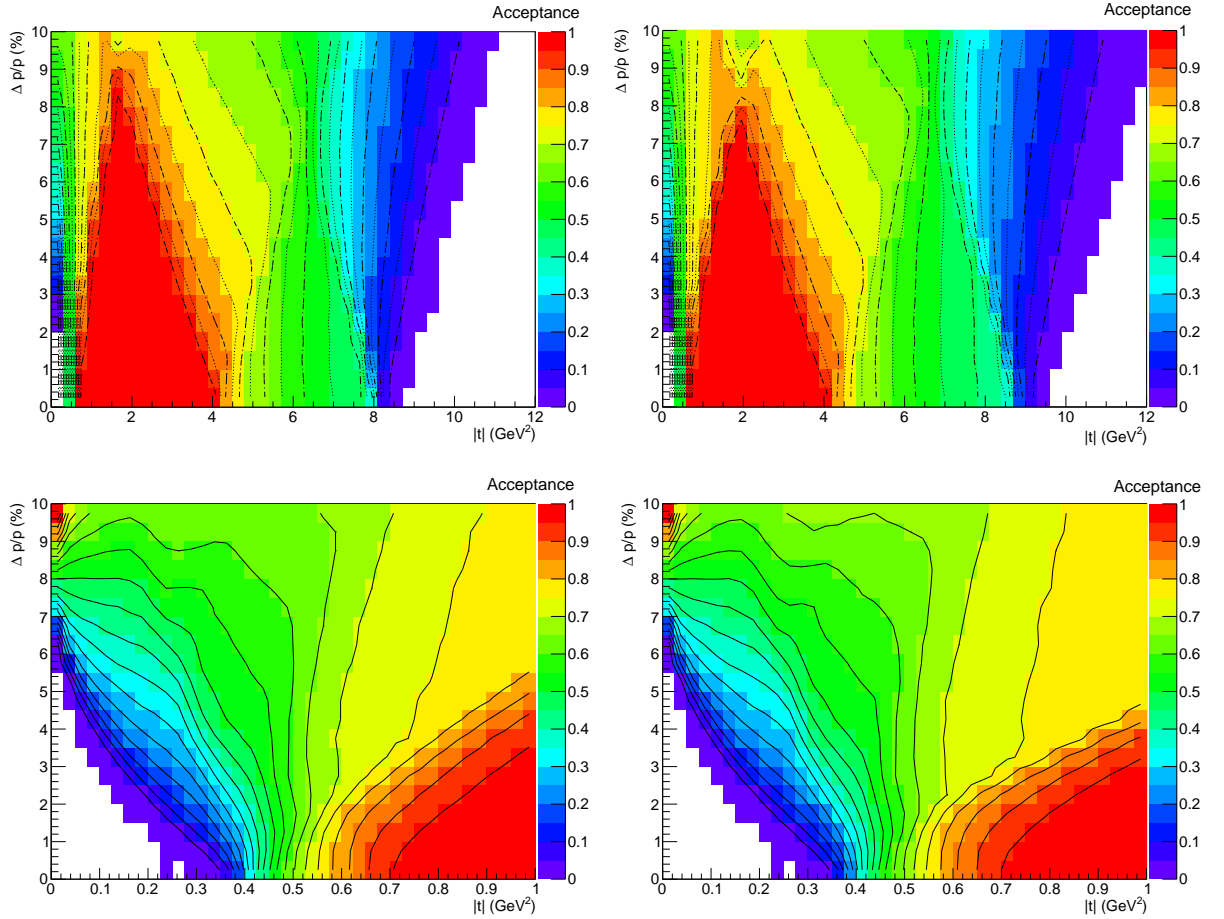
Figure 6.3: Acceptances of the $\beta^* = 18\,\text{m}$ optics for different $|t|$- and $\xi = \Delta p/p$ ranges in standard conditions for the ALICE A-side (left) and the ALICE C-side (right). The contour lines correspond to acceptance steps of 0.05.
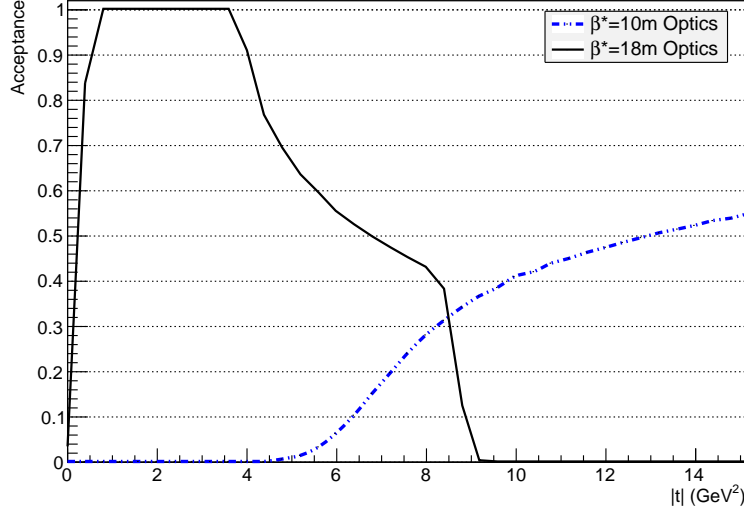
Figure 6.4: Comparison of the acceptances for elastic events ($\xi = 0$) with the nominal $\beta^* = 10\,\mathrm{m}$ optics and with the $\beta^* = 18\,\mathrm{m}$ optics for the measurement on the ALICE C-side.

Fig. 6.4 shows a comparison of the acceptance evolution for the nominal ALICE optics and the $\beta^* = 18\,\mathrm{m}$ optics in the range $0\,\mathrm{GeV}^2 \leq |t| \leq 16\,\mathrm{GeV}^2$ with $\xi = 0$. It is clearly visible that the matched optics improve the measurability at very low $|t|$-values in comparison to the the nominal optics. The drop of the acceptance for $|t| > 4\,\mathrm{GeV}^2$ is due to the outer limit of the detectability. The acceptance evolution for $|t| > 4\,\mathrm{GeV}^2$ shows a step at $|t| \approx 8\,\mathrm{GeV}^2$, which can be traced back to the condition that the particle should be detectable in both RP stations.

With the given boundary conditions (standard conditions), an acceptance of $\mathcal{A} = 100\%$ can not be reached with the $\beta^* = 10\,\mathrm{m}$ optics.

For the ALICE A-side, the corresponding acceptance evolution is not shown. However, as shown in Fig. 6.3, the acceptance evolution for the measurement on the ALICE A-side with the $\beta^* = 18\,\mathrm{m}$ optics is similar to the measurement on the ALICE C-side.

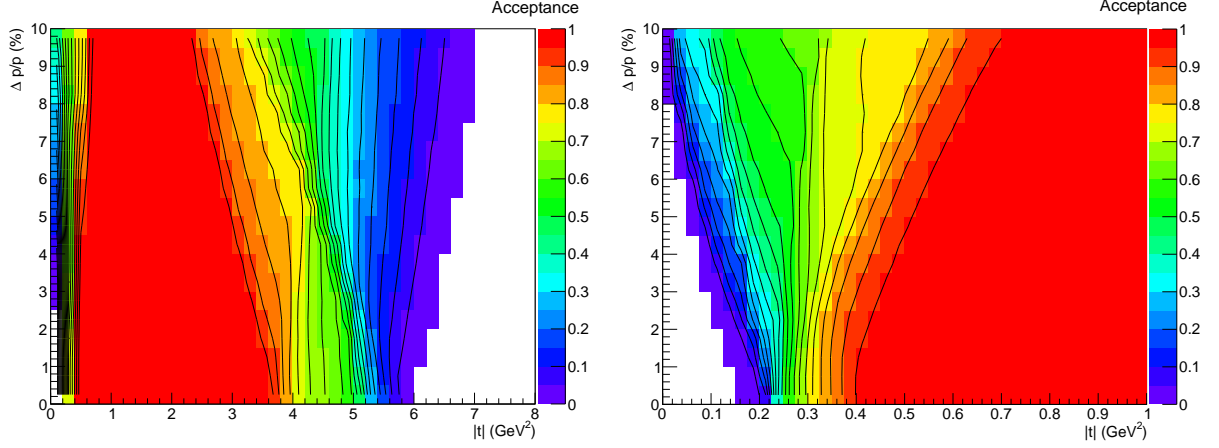### 6.2.3 The $\beta^* = 30\,\mathrm{m}$ Optics

Figure 6.5: Acceptance of the $\beta^* =30\,\mathrm{m}$ optics as a function of $|t|$ and $\xi = \Delta p/p$ in different $|t|$-ranges for the ALICE C-side. The contour lines correspond to acceptance steps of 0.05.

The detector acceptance as a function of $|t|$ and ξ for the $\beta^* =30\,\mathrm{m}$ optics is shown for the ALICE C-side in Fig. 6.5. The acceptance distribution is comparable to the calculations for the $\beta^* = 18\,\mathrm{m}$ optics, but shifted to smaller $|t|$-values. The direct comparison between the two optics is shown for elastic events in Fig. 6.6. With this optical configuration, the $\mathcal{A} = 50\%$ threshold is already reached for $|t|_{50\%} = 0.24\,\mathrm{GeV}^2$.
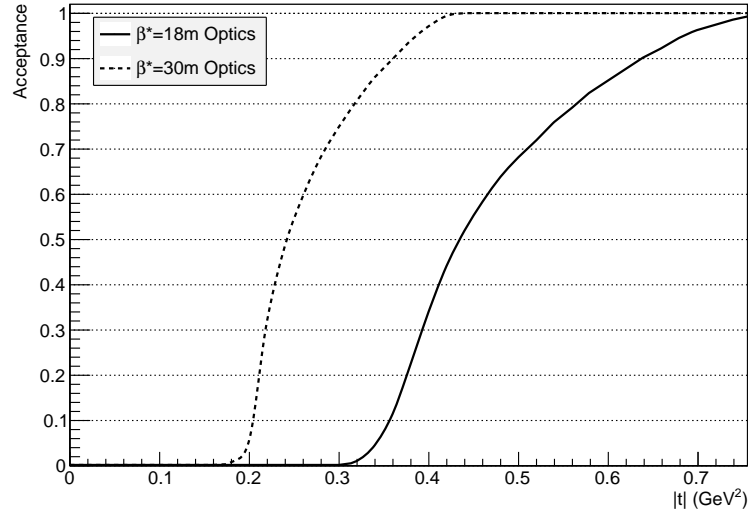

Figure 6.6: Comparison of the acceptances for elastic events ($\xi = 0$) on the ALICE C-side with the $\beta^* = 18\,\mathrm{m}$ optics and the $\beta^* = 30\,\mathrm{m}$ optics.

6.3   Special Conditions

The shown acceptances were calculated with the standard conditions defined in Chap. 6.1. In the following chapter, the individual parameters are varied separately in reasonable limits, and the impact on the acceptance is discussed. This gives an impression on the possible uncertainties on the acceptance by the choices which were made. With the exception of the detector geometry, all assumptions in the standard conditions are conservative choices which lead to the worst possible acceptance for a given optical configuration.

6.3.1   Beam Emittance

The considered standard emittance was the Design Report value of $\epsilon_N = 3.75\,\mu$m rad. As it will be discussed in Chap. 7.4, lower emittances than this are reachable in the LHC. Fig. 6.7 shows the acceptance of the $\beta^* =18$ m optics for Beam 1 with different emittances while all other parameters remain at standard conditions. As expected, the $|t|_{50\%}$-value decreases with decreasing emittance. With the smallest considered emittance of $\epsilon_N = 2.25\,\mu$m rad, the $\mathcal{A} =50\,\%$ threshold is reached for $|t|_{50\%} = 0.26\,\text{GeV}^2$.
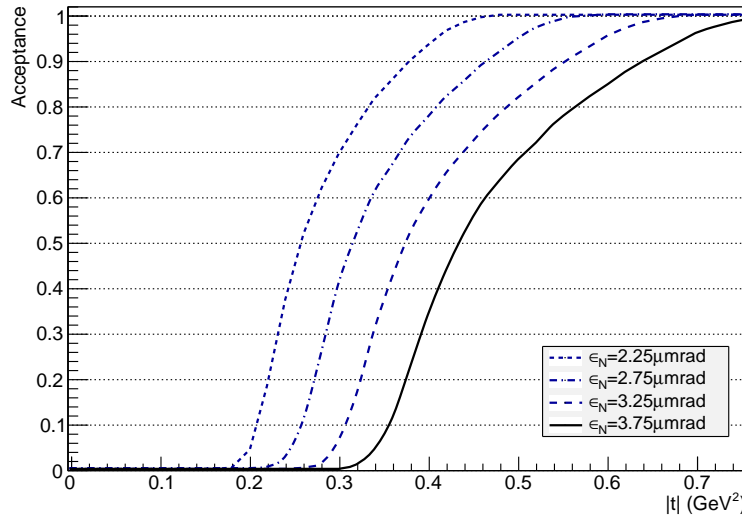

Figure 6.7: Acceptance of the $\beta^* = 18$ m optics on the ALICE C-side for elastic events with different emittances. The black solid line corresponds to the standard conditions.

6.3.2 Detector Distance

In the standard conditions, a distance of $D_{\mathrm{db}} = 14\,\sigma$ between the beam centre and the detector edge is considered. This was outlined to be a conservative value [Sch12]. The acceptance at the ALICE C-side for elastic events with three different detector distances ($D_{\mathrm{db}} = 10\,\sigma$, $12\,\sigma$, $14\,\sigma$) is shown in Fig. 6.8 while using standard conditions for the remaining parameters.

The $|t|_{50\%}$-value decreases with decreasing detector distance. With the smallest considered detector distance of $D_{\mathrm{db}} = 10\,\sigma$, the $\mathcal{A} = 50\%$ threshold is reached for $|t|_{50\%} \approx 0.24\,\mathrm{GeV}^2$.
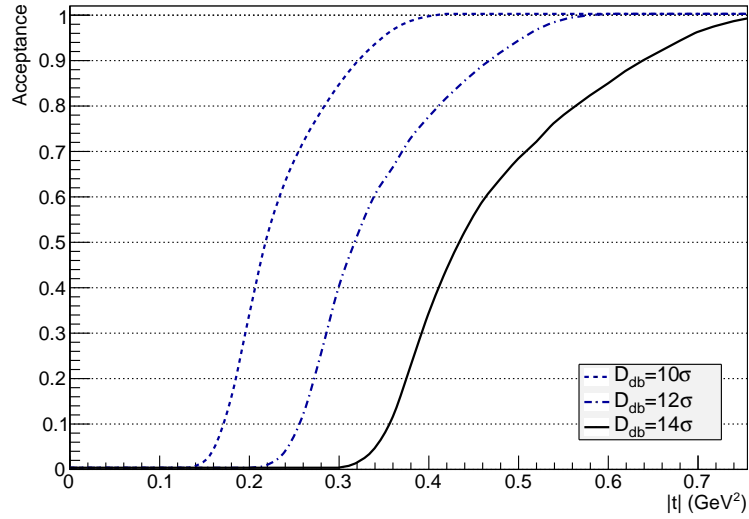

Figure 6.8: Acceptances of the $\beta^* = 18\,\mathrm{m}$ optics for elastic events on the ALICE C-side for different detector distances D_{db} of the edgeless silicon detectors from the beam centre. The black, solid line represents the acceptance in standard conditions.

6.3.3 Detector Geometry

The detector layout which is considered in the standard conditions presumes one horizontal detector at either of the two sides of the beam (for $x < 0$ and $x > 0$). However, this is a hypothetical, ideal detector layout, which is not applied in the Roman Pot detectors used by TOTEM and ALFA (Fig. 6.1 shows the detector layout in the standard conditions and Fig. 4.5 shows the detector layout of the RPs which are installed in IR1 and IR5). It is not yet known whether the installation of a second set of horizontal sub-detectors in the Roman Pot stations is feasible or not. The detector layout in the standard conditions was an optimistic assumption.
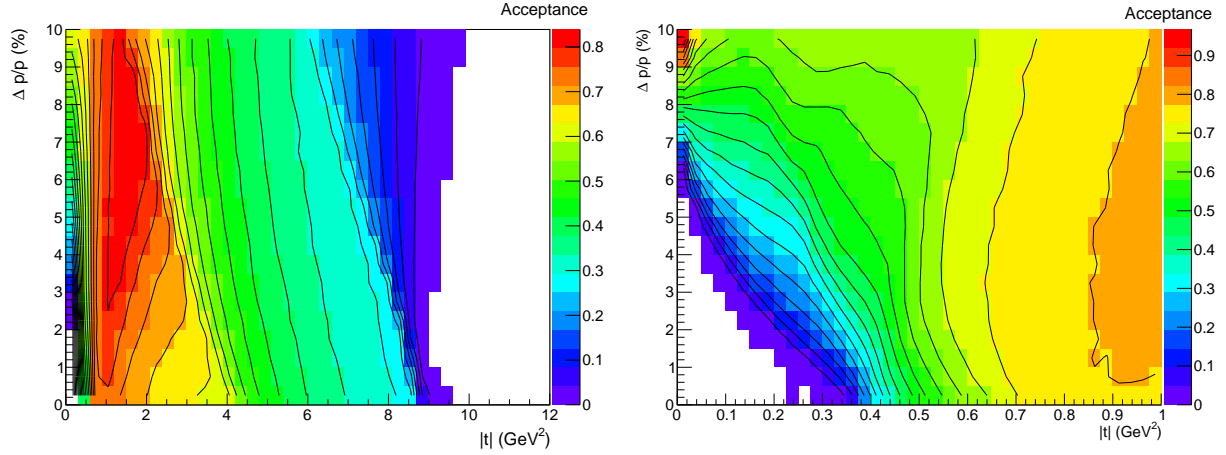
Figure 6.9: Acceptance of the $\beta^* = 18\,\mathrm{m}$ optics on the ALICE C-side with one instead of two horizontal detectors. Note the different z-axis ranges between left and right. The contour lines correspond to acceptance steps of 0.05.

The result of the acceptance calculations, using the detector design of the existing RPs with one set of edegeless silicon detectors in horizontal direction [BV09], is shown in Fig. 6.9. The horizontal set of the edgeless silicon sub-detectors is installed at the outer side of the respective beam pipe[1]. For the measurements with Beam 1 (ALICE C-side), the horizontal detector would be placed at the side with $x > 0$, and vice versa for the measurement with Beam 2 (ALICE A-side). The sign of the horizontal vertical dispersion function at the RP location is such, that particles with momentum loss $\xi > 0$ are deviated towards the remaining horizontal edgeless silicon detector. Furthermore, the vertical detectors have an overlap with the horizontal detectors, as shown in Fig. 4.5. Thus, the corrected acceptance $\mathcal{A}_c$ is related to the standard acceptance $\mathcal{A}$ by

$$\mathcal{A}_c > 0.75\,\mathcal{A}\,. \tag{6.2}$$

This scaling is clearly visible when comparing the acceptance in standard conditions in Fig. 6.5 with the corrected acceptances shown in Fig. 6.9. The $\mathcal{A} = 50\,\%$ threshold for elastic events is reached at $|t|_{50\%} = 0.49\,\mathrm{GeV}^2$ with standard conditions being applied for the remaining parameters.

---

[1]In this sense, the outer side means the horizontal side of the beam pipe which is not between the two pipes, in which Beam 1 and Beam 2 are moving, respectively.

6.4 Conclusion

The acceptance studies show that the detector acceptance of the RPs is significantly improved with the $\beta^* = 18\,\mathrm{m}$ optics, compared to the nominal $\beta^* = 10\,\mathrm{m}$ configuration in ALICE. However, a clear statement on the reachable $|t|$-acceptance can not be given, because the relevant parameters are not fully known yet. Based on different assumptions on the beam parameters, the detector layout, and the possible detector settings, a possible $|t|_{50\%}$-range of

$$0.24\,\mathrm{GeV}^2 \leq |t|_{50\%} \leq 0.49\,\mathrm{GeV}^2\,, \tag{6.3}$$

was deduced for the measurements on the ALICE C-side with the $\beta^* = 18\,\mathrm{m}$ optics. The lower limit is rather optimistic, even if combinations of optimistic parameters (e.g. reduced emittance and smaller detector distance in terms of σ at the same time) are not covered. Especially due to fact that the optics are intended to be implemented during high-intensity operation, the detector-distance from the beam centre should be evaluated very conservatively.

The same considerations for the $\beta^* = 30\,\mathrm{m}$ optics lead to an acceptance range

$$0.13\,\mathrm{GeV}^2 \leq |t|_{50\%} \leq 0.28\,\mathrm{GeV}^2\,. \tag{6.4}$$

Since no concrete strategy for the required phase advance compensation has been worked out yet, the acceptance of rematched optics with $\beta^* = 18\,\mathrm{m}$, which require lower phase advance compensations, is discussed in Chap. 7.5.

7.   Outlook

This chapter gives information about additional studies which have been carried out in relation to the development of the high β^*-optics for ALICE. This includes the compatibility of the optics with upgrade scenarios, additional studies on phase advance compensation, the transition from injection to collision optics, studies on the reachable resolution in $|t|$ and ξ, and the reachable emittances during operation of the LHC.

7.1   New ALICE Beam Pipe

For the second upgrade interval of the LHC, it is foreseen to install a new beam pipe at ALICE, in order to allow the installation of detector layers closer to the collision point. This leads to a reduced available aperture at the collision point. The proposed dimensions of the beam pipe are shown in Fig. 7.1. Even though previous studies [Gio12] indicate that the new beam pipe is not compatible with the injection optics, the aperture at LHC design energy was studied for the β^* =18 m optics and the β^* =30 m optics. The calculated geometrical acceptance in terms of n_1 is shown in Fig. 7.2. Obviously, the available aperture at LHC design energy is reduced when using the smaller pipe dimensions, but the limitation of $n_1 = 7$ is not reached.
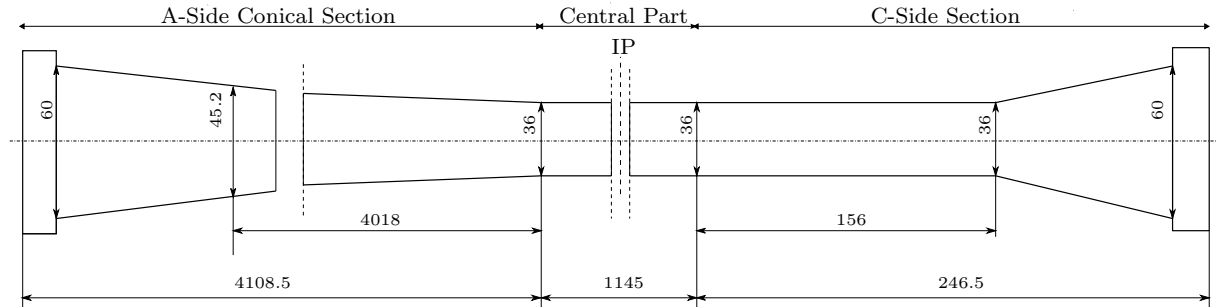

Figure 7.1: Prospective new ALICE beam pipe dimensions after Long Shutdown 2 [Rie12]. The diameter at IP2 of the present beam pipe is $d = 58\,\mathrm{mm}$.
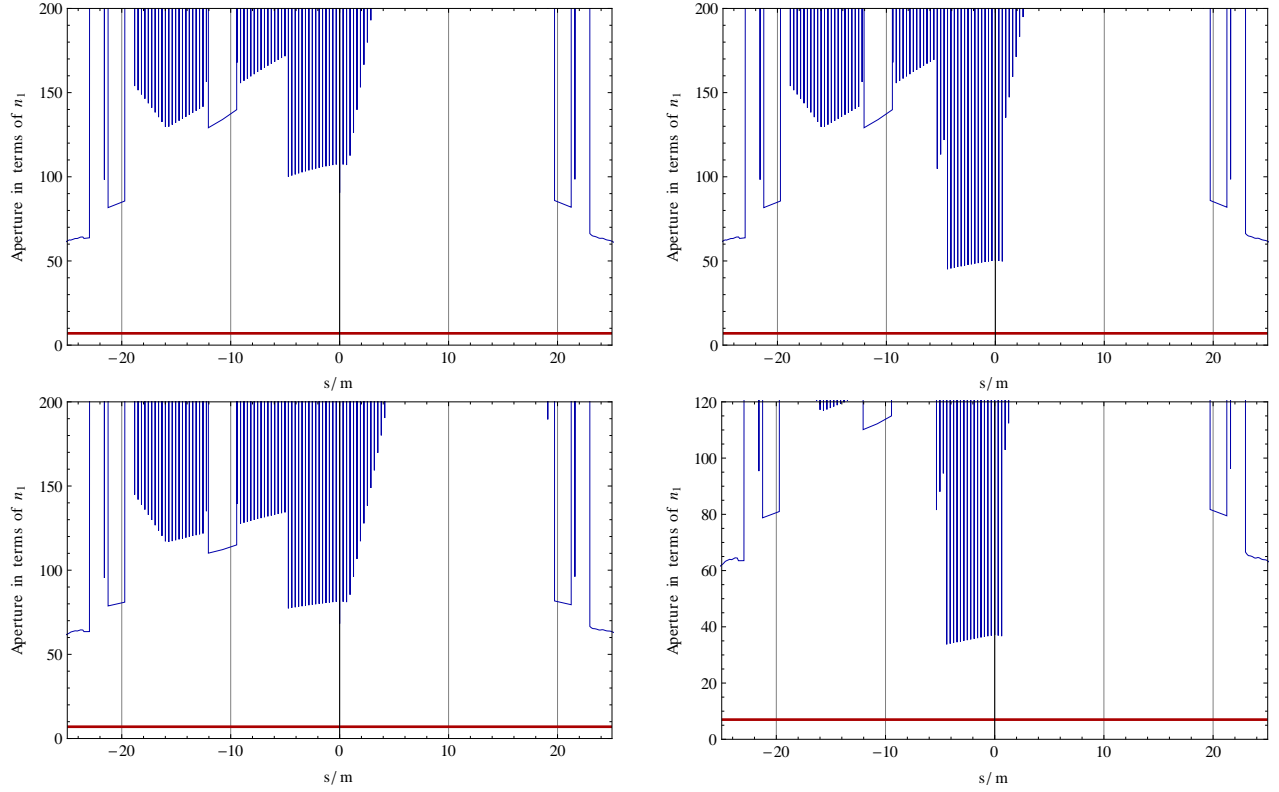
Figure 7.2: Top: Aperture at 7 TeV with $\epsilon_N = 3.75\,\mu\text{m rad}$ for the $\beta^* =18\,\text{m}$ optics in the inner triplet region for the present ALICE beam pipe (left) and for the new ALICE beam pipe (right). Bottom: The same quantities are shown for the 30 m optics. Note the different scales between left and right. The shown n_1-functions are calculated for Beam 1 but the optical functions and the available aperture are the same for Beam 2 (all crossing and spectrometer bumps switched on).

7.2   Un-Squeeze

In analogy to the squeeze in the nominal LHC cycle, the transfer from the injection optics to the collision optics has to be performed in several steps, in order to have a continuous transition of the magnet strengths. In the high β^*-optics implementation, this transition is usually referred to as the un-squeeze. The average increase of the β^*-value between two intermediate steps to reach the existing high β^*-optics in IR1/IR5 is 10%-15% [Bur12b]. In between two matched optical configurations, the magnet strengths are linearly interpolated which implies some β-beating.

Such intermediate configurations will also have to be developed for IR2, if the presented optics should be implemented. Compared to the IR1/IR5 optics, the change of the phase advance between the initial optics and the high β^*-optics in IR2 is very large, while the difference of the β^*-values is lower. Therefore, transitions with several intermediate steps at a fixed β^*-value but with a changing phase advance cause could be applied. Since the triplet strength for all presented configurations is reduced, a time-saving simultaneous ramp and un-squeeze could be used. For the $\beta^* = 18\,\text{m}$ optics, the final triplet strength is 77.8% of the nominal strength, which would be reached at 5.446 TeV. All intermediate steps must respect the same boundary conditions of the LHC as the collision optics.

7.3 Reconstruction

An algorithm for the reconstruction of the $|t|$- and ξ-value was developed by R. Schicker [Sch13]. It is based on the minimization of χ^2, using the particle positions at the two successive detector locations (see also [TSC11]), and the angle of incidence. By means of this algorithm, the reachable resolution in ξ and $|t|$ can be evaluated as a function of the detector resolution.
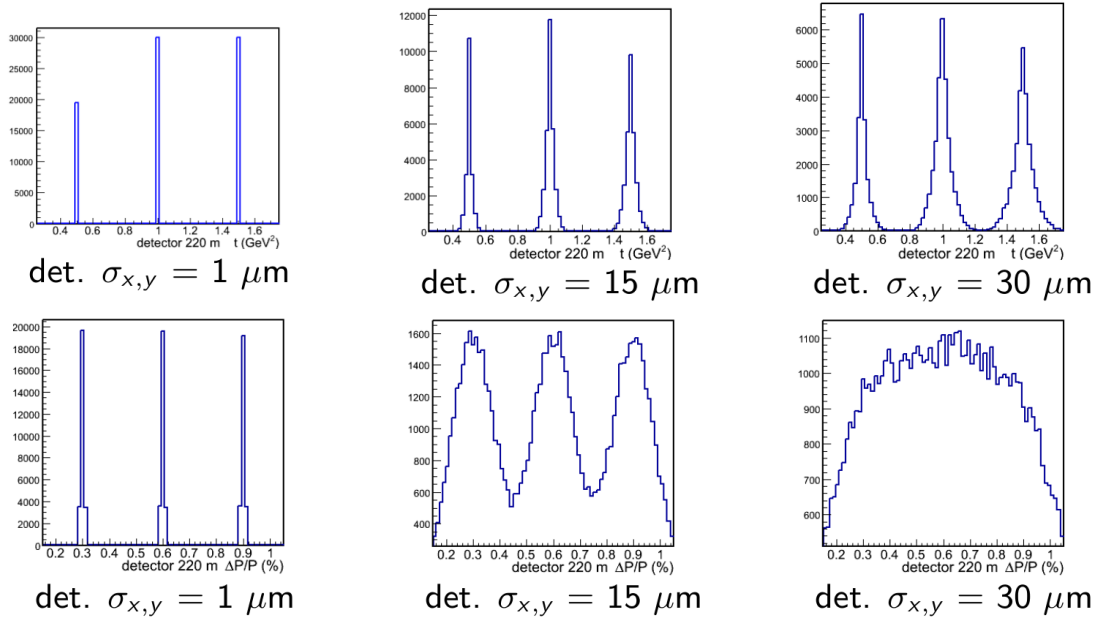

Figure 7.3: Reconstructed signals for different detector resolutions with the $\beta^* = 18\,\text{m}$ optics. Top: Response signals for $|t| = 0.5\,\text{GeV}^2$, $t = 1.0\,\text{GeV}^2$, $t = 1.5\,\text{GeV}^2$. Bottom: Response signals for $\xi = 0.03$, $\xi = 0.06$, $\xi = 0.09$. The considered detector resolutions are given by $\sigma_{x,y}$ for each figure. Graphics from [Sch13].

The total reconstructed signal is given by the convolution of the physical distribution at the detector locations (for fixed parameters ξ and $|t|$) with the detector response. The resolution in $|t|$ and ξ depends on the physical distance for different $|t|$- and ξ-values in the edgeless silicon detectors, and on the detector resolution. The detector response signal for three equally distributed $|t|$- and ξ-values is compared for different considered detector resolutions in Fig. 7.3. With a detector resolution of $\sigma_{x,y} = 30\,\mu\mathrm{m}$, two signals with $\Delta t = 0.5\,\mathrm{GeV}^2$ can be well-separated, while two signals with $\Delta\xi = 0.03$ become blurred.

7.4 Future Beam Emittances

As mentioned in previous chapters, during the operation of the LHC, it turned out that the injectors could deliver beams with much better emittance than foreseen in the LHC Design Report. In regular 50 ns physics operation, normalized emittances of $\epsilon_N = 2\,\mu\mathrm{m}\,\mathrm{rad}$ were reached [K$^+$11]. Furthermore, during special machine development runs with a bunch spacing of 25 ns, emittances as low as $\epsilon_N = 1.4\,\mu\mathrm{m}\,\mathrm{rad}$ could be achieved [Jow13]. Therefore, it is realistic to consider smaller emittances than the LHC Design Report value. Smaller emittances would be advantageous for many reasons:

1. Thanks to the smaller beam dimensions, a larger β^*-value is reachable with the same crossing angle and the same required separation. This can be used to adjust the IR phase advance while maintaining the acceptance constant, or to increase the acceptance by a larger β^*-value while keeping the IP-RP phase advance constant.

2. The Roman Pot detectors can be brought closer to the beam centre, which improves the acceptance for low $|t|$-values.

3. The smaller beam sizes lead to a better tunability of IR4, making larger tune compensations possible.

In conclusion, the feasibility calculations for the β^*-value and the phase advance compensation can be seen as lower, conservative limits. Pursuing studies on optics with larger β^*-values could be realized, once reliable input on realistic emittances during the future 25 ns physics operation is available. However, with the $\beta^* = 18\,\mathrm{m}$ optics and the $\beta^* = 30\,\mathrm{m}$ optics, the very conservative and very optimistic extremes for possible high β^*-optics on ALICE were presented.

7.5 Additional Studies on Phase Advance Compensation

As discussed in Chap. 3.5.2, the B1/B2 ratio constraint arises from the current cabling of the LHC quadrupole magnets. If this constraint was eliminated, then the betatron functions for one beam would not have to be x/y anti-symmetric with respect to the IP. This would give (in principle) the possibility to compensate the phase advance within the IR. First matchings showed, that non-symmetric optics are feasible and larger IR phase advances can be reached.

Numerous rematches were done to evaluate the impact of different $\Delta\psi$-values on the acceptance. Fig. 7.4 shows the required phase advance compensation ΔQ as a function of the corresponding $\mathcal{A} = 50\%$ acceptance threshold. The acceptance calculations are realized under standard conditions. As shown, the required compensation in vertical direction can be significantly reduced if larger $|t|_{50\%}$-values would be acceptable. The required phase advance compensation with $|t|_{50\%} = 0.70\,\mathrm{GeV}^2$ would be $\Delta\psi_{\mathrm{IR}} = 0.404/0.257$. Following Fig. 5.11, this phase advance could be compensated, using only the arc quadrupoles between IP1 and IP5. In combination with the conservative detector layout with only one horizontal detector, this threshold becomes

$$|t|_{50\%} = 0.78\,\mathrm{GeV}^2 \,. \tag{7.1}$$

Since it is known that the required phase advance compensation for such a configuration could be provided, this can be seen as an upper limit of the reachable acceptance threshold.
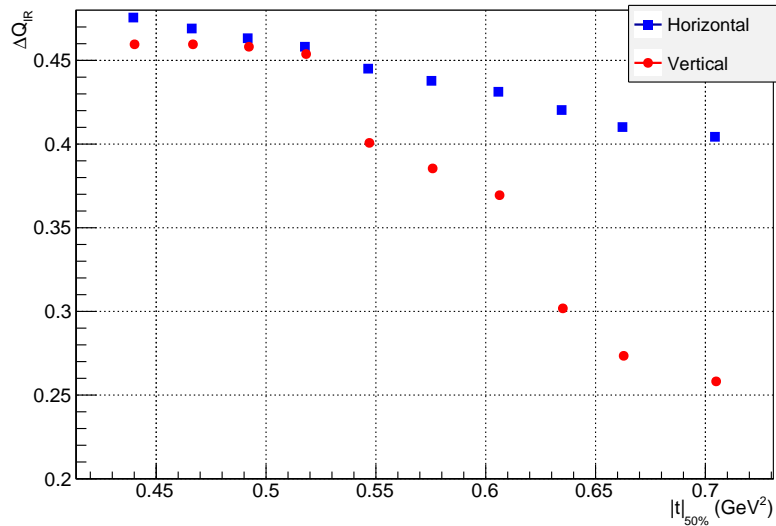

Figure 7.4: Required phase advance compensations in the two transverse directions as a function of the $|t|_{50\%}$-threshold for different rematched optics with $\beta^* = 18\,\mathrm{m}$.

Summary

In this thesis, the development and evaluation of an optical configuration with large β^*-value in the LHC region around the ALICE detector was described. This configuration should allow the measurement of very forward particles in parallel to the nominal proton-proton physics program in ALICE and the remaining LHC experiments. Very forward particles are emitted from the Interaction Point, due to diffractive or elastic scattering events, probably related to the exchange of one or multiple Pomerons. The detection of these particles can be provided by means of Roman Pot detectors, installed in the very forward region.

The optics design must optimize the measurability of the very forward particles, but respect the many constraints which are imposed by the present configuration of the LHC. For the optimization of the measurement, the β^*-value should be maximized, and the betatron phase advance between the Interaction Point and the prospective Roman Pot detector positions must be matched to a value as closely as possible to $\Delta\psi = 0.25$.

Based on conservative assumptions on the reachable emittance, the reachable crossing angle, and the required beam-beam separation, a value of $\beta^* = 18\,\mathrm{m}$ is considered, which is compatible with the LHC design filling scheme with 2808 bunches (corresponding to a bunch spacing of 25 ns). The beam line around the ALICE detector is analyzed for suitable positions for the Roman Pot detector placement. The proposed locations are at longitudinal distances of -180 m/-220 m from the Interaction Point for the measurement with Beam 2, and at +150 m/+220 m for the measurement with Beam 1. The installation of two detector stations is necessary for the reconstruction, because the phase advance between Interaction Point and Roman Pot detector can not be matched to the desired value. Optics with $\beta^* = 18\,\mathrm{m}$ were matched and optimized for best performance in terms of measurability of very low four-momentum transfers $|t|$. A phase advance of $\Delta\psi = 0.34$ to the second detector station can be reached for both beams in both transverse directions. The optics are compatible with the magnet limitations, aperture constraints and separation requirements. In order to provide a sufficiently large beam-beam separation at the parasitic bunch encounters, a crossing scheme, providing a full crossing angle of $\theta_C = 300\,\mu\mathrm{rad}$, was matched.

Very large phase advance compensations must be provided by other parts of the machine. Due to the required applicability in high-intensity operation, this phase advance compensation must be feasible between IP1 and IP5. So far, no concrete strategy for this compensation was worked out. With the proposed configuration, the luminosity in ALICE is reduced, but is still too large to match the detector requirements.

The $|t|$- and ξ-acceptance of the matched optics with the proposed detector locations is studied. The results of these studies are strongly depending on the assumptions which are made for the beam properties, the detector layout and detector distance from the beam centre. In the rather conservative standard conditions, the $\beta^* = 18\,\mathrm{m}$ optics reach an acceptance of $\mathcal{A} = 50\%$ for elastic events ($\xi = 0$) at a value of $|t|_{50\%} = 0.44\,\mathrm{GeV}^2$, instead of $|t|_{50\%} \approx 13\,\mathrm{GeV}^2$ with the nominal optical configuration in Insertion Region 2. Taking into account either more optimistic or more pessimistic measurement scenarios, an interval with upper and lower limits of the reachable acceptance with $\beta^* = 18\,\mathrm{m}$ can be given

$$0.24\,\mathrm{GeV}^2 \leq |t|_{50\%} \leq 0.78\,\mathrm{GeV}^2. \tag{7.2}$$

Besides the $\beta^* = 18\,\mathrm{m}$ optics, a configuration with $\beta^* = 30\,\mathrm{m}$ is briefly discussed, which is compatible with a bunch spacing of $50\,\mathrm{ns}$. The phase advance from Interaction Point to Roman Pot detectors of this configuration is matched to $\Delta\psi = 1/3$. The acceptances of this configuration are better than for the $\beta^* = 18\,\mathrm{m}$ case. However, this configuration is most likely not implementable during high-intensity operation of the LHC, with the largest number of bunches. Additional studies which have to be carried out before real implementation of the optics are outlined. A continuous un-squeeze for the transition from injection optics to the $\beta^* = 18\,\mathrm{m}$ optics must be developed. The optics are compatible with the prospective new ALICE beam pipe dimensions. An algorithm for the reconstruction of the $|t|$- and ξ-values is discussed. Lower emittances would enhance the potential of high β^*-optics and give the possibility to apply larger β^*-values. Significant reductions of the required external phase advance compensation can be reached at the expense of an increased acceptance threshold.

In conclusion, an optical configuration with increased β^*-value and matched phase advance, compatible to long time running conditions, was found to be feasible for ALICE. The concrete details of such a configuration still depend on subsequent studies on phase advance compensation and on the reachable emittance in high-intensity operation. Several essential steps for the implementation still have to be taken, which will be carried out if ALICE decides to implement a high β^*-configuration. For the presented $\beta^* = 18\,\mathrm{m}$ optics, an interval for the reachable acceptances as a function of $|t|$ can be given. Ongoing studies [S+13] indicate that acceptances in this range are eligible for the study of additional physics topics at the LHC.
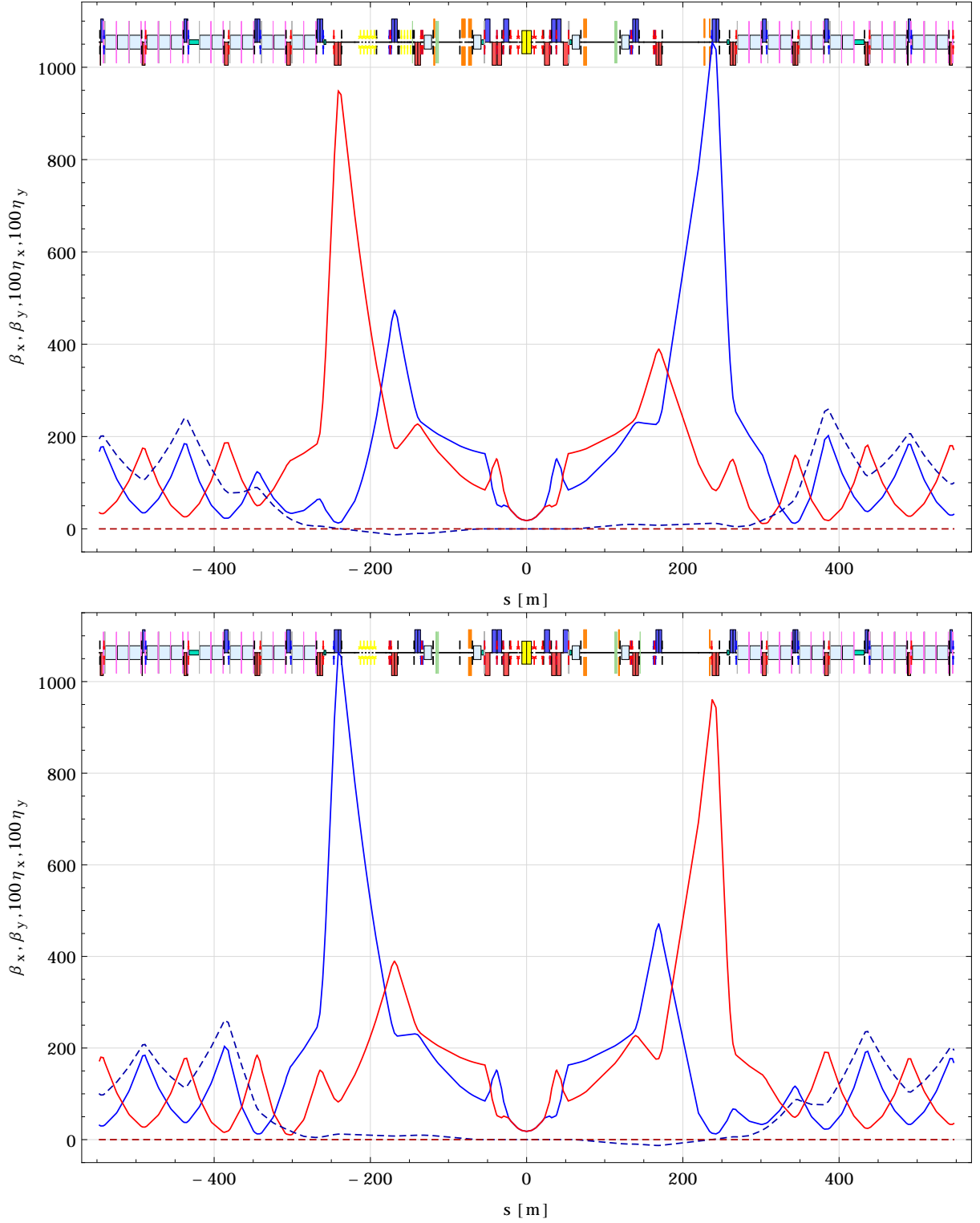
Appendix

Figure 7.5: Optical functions of the $\beta^* = 18\,\text{m}$ optics. Blue line: β_x, red line: β_y, blue dashed line: η_x, red dashed line: η_y. All bumps switched off. Top: Beam 1, Bottom: Beam 2.
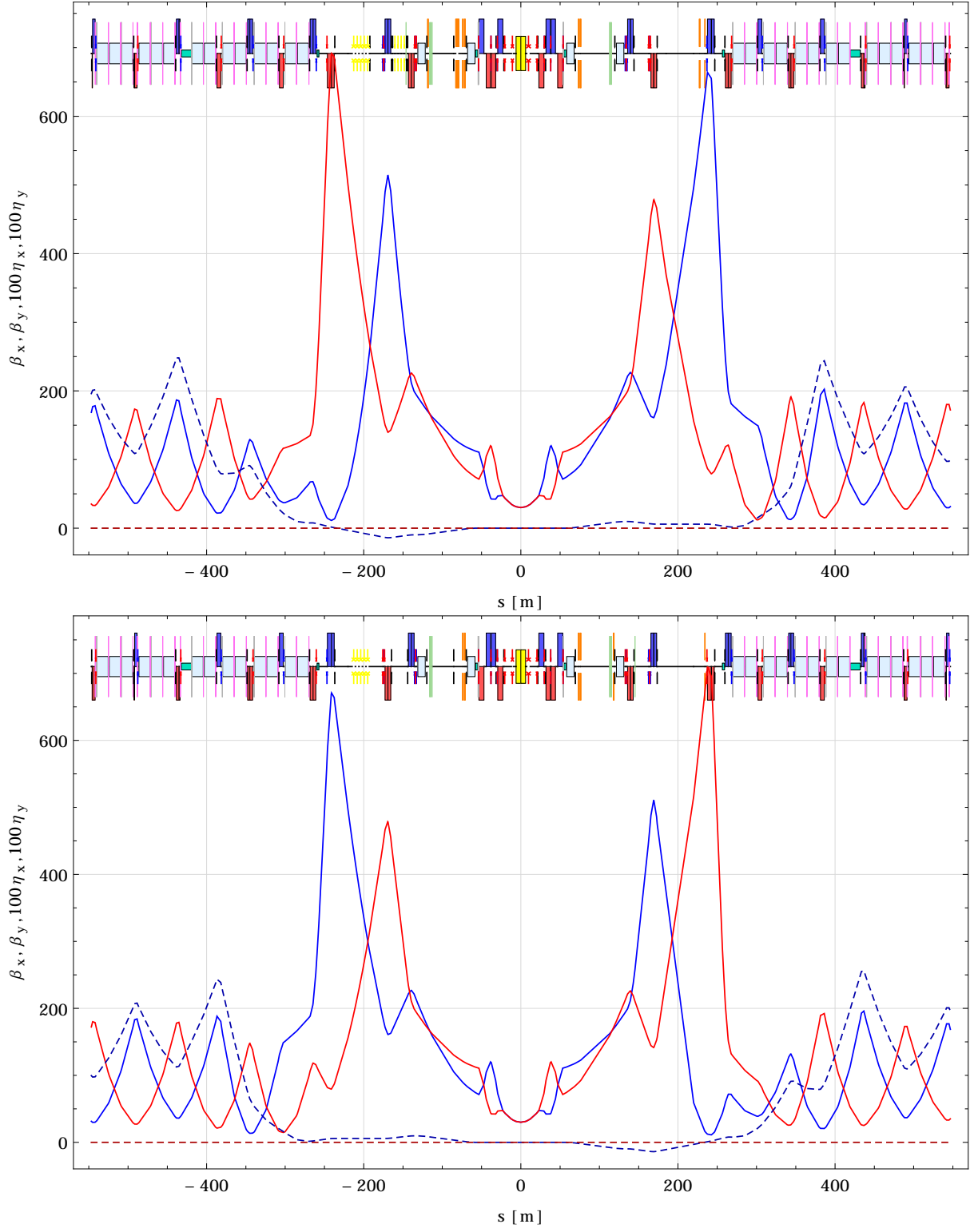
Figure 7.6: Optical functions of the $\beta^* = 30\,\text{m}$ optics. Blue line: β_x, red line: β_y, blue dashed line: η_x, red dashed line: η_y. All bumps switched off. Top: Beam 1, Bottom: Beam 2.

Table 7.1: Normalized quadrupole gradients of the $\beta^* = 18\,\text{m}$ optics and the $\beta^* = 30\,\text{m}$ optics.

Magnet-Strength	Limits $[\pm10^{-4}\text{m}^{-2}]$		18 m optics $[10^{-4}\text{m}^{-2}]$				30 m optics $[10^{-4}\text{m}^{-2}]$			
			L2B1	R2B1	L2B2	R2B2	L2B1	R2B1	L2B2	R2B2
KQT13.	−52.67	52.67	-27.17	-33.83	-33.11	-20.29	-34.28	-31.07	-34.73	-38.11
KQT12.	−52.67	52.67	-44.89	-46.19	-40.69	-46.88	-48.37	-28.29	-34.42	-42.25
KQTL11.	−53.53	53.53	7.23	-37.93	-45.46	8.56	7.76	-46.72	-31.61	9.52
KQ10.	1.60	85.65	-60.84	74.20	74.13	-62.40	-63.59	74.84	73.57	-70.04
KQ9.	1.60	85.65	59.36	-76.60	-77.10	59.63	59.63	-75.26	-71.70	59.46
KQ8.	1.60	85.65	-21.00	33.25	34.42	-19.21	-25.97	43.63	41.40	-29.35
KQ7.	1.60	85.65	74.75	-57.97	-59.24	76.08	74.98	-55.23	-51.15	74.88
KQ6.	1.60	68.50	-42.71	39.40	39.29	-43.57	-42.5	37.58	36.39	-43.67
KQ5.	3.80	68.50	35.65	-24.28	-24.28	35.77	39.85	-31.64	-31.64	40.00
KQ4.	3.80	68.50	-17.09	10.13	10.13	-16.91	-23.11	20.00	20.00	-22.85
KQX.L2	2.45	87.80	68.32				60.40			
KTQX1.L2	±7.34		-2.76				-2.51			
KTQX2.L2	±35.12		2.87				2.45			

Bibliography

[A⁺08]   M. Aiba *et al.* Optics flexibility in the LHC at top energy. *Proceedings of EPAC, Genoa, Italy*, 2008.

[ADK04]   V.V. Anashin, R.V. Dostovalov, and A.A. Krasnov. The vacuum studies for LHC beam screen with carbon fiber cryosorber. *Proceedings of APAC, Gyeongju, Korea*, 2004.

[AF⁺12]   R. Alemany-Fernandez *et al.* ALICE spectrometer polarity reversal. Technical Report CERN-ATS-2012-039 MD, Geneva, Apr. 2012.

[ALI00]   ALICE Collaboration. Technical Design Report of the Time Projection Chamber. 2000. CERN / LHCC 2000-001.

[ALI01]   ALICE Collaboration. Technical Design Report of the Transition Radiation Detector. 2001. CERN / LHCC 2001-021.

[ALI04a]   ALICE Collaboration. ALICE: Physics Performance Report, Volume I. *J. Phys. G: Nucl. Part. Phys.*, 30(11), 2004.

[ALI04b]   ALICE Collaboration. ALICE Technical Design Report on forward detectors: FMD, T0 and V0. Technical report, CERN-LHCC-2004-025, 2004.

[ALI08a]   ALICE Collaboration. The ALICE experiment at the CERN LHC. A Large Ion Collider Experiment. *J. Instrum.*, 3:S08002. 259 p, 2008.

[ALI08b]   ALICE Website. `http://aliceinfo.cern.ch/Public/en/Chapter2/Chap2Experiment-en.html`, 2008. [Online; accessed 26-Oct-2012].

[ALI10]   ALICE Collaboration. Alignment of the ALICE Inner Tracking System with cosmic-ray tracks. *J. Instrum.*, 5:P03003. p.1–38, 2010.

[ALI13] ALICE MATTERS Website. The proton-lead run: A new adventure for the ALICE experiment. `http://alicematters.web.cern.ch/?q=endpPBrun`, 2013. [Online; accessed 11-Apr-2013].

[ATL11] ATLAS Collaboration. Observation of a new χ_b state in radiative transitions to Υ(1S) and Υ(2S) at ATLAS . *Phys. Rev. Lett.*, 108(CERN-PH-EP-2011-225), Dec. 2011.

[ATL12] ATLAS Collaboration. Observation of a new particle in the search for the Standard Model Higgs boson with the ATLAS detector at the LHC. *Phys. Lett. B*, (716):1–29, 2012.

[AW12] R. Assmann and J. Wenninger. Von der Idee zur Rekordmaschine. *Physik Journal*, 11(04), 2012.

[B⁺03] O. Brüning *et al.* The Nominal Operational Cycle of the LHC with Beam (version 1). Technical Report LHC-Project-Note-313, CERN, Geneva, Feb. 2003.

[B⁺04] O. Brüning *et al. LHC Design Report (Volume I, The LHC Main Ring)*. CERN, Geneva, 2004.

[B⁺11] H. Burkhardt *et al.* 90 m Optics Commissioning. San Sebastian, Spain, 2011. Proceedings of IPAC2011.

[B⁺12a] O. Brüning *et al.* The Large Hadron Collider. *Prog. Part. Nucl. Phys.*, 10.1016/j.ppnp.2012.03.001, Apr. 2012.

[B⁺12b] H. Burkhardt *et al.* Plans for High Beta Optics in the LHC. Technical Report CERN-ATS-2012-141, CERN, Geneva, May 2012.

[Bac89] G. Bachy. Engineering and construction experience at LEP. (CERN-LEP-IM-89-31), Apr. 1989.

[Brü99] O. Brüning. Optics solutions in IR2 for Ring-1 and Ring-2 of the LHC Version 6.0. Technical Report LHC-Project-Note-188, CERN, Geneva, May 1999.

[BT01] F. Bordry and H. Thiesen. LHC inner triplet powering strategy. In *Proceedings of the Particle Accelerator Conference 2001*, volume 1, pages 633–635. IEEE, 2001.

[Bul02] CERN Bulletin. A magnet worthy of ALICE. (BUL-NA-2002-143):1, Nov. 2002.

[Bur12a] H. Burkhardt, October 2012. Poster on IPAC2012.

[Bur12b] H. Burkhardt, 2012. Private Communication.

[Bur13] H. Burkhardt. Strategy for very high β running after LS1. Talk at ALFA Meeting, March 2013. `https://espace.cern.ch/lhc-machine-committee/Minutes/1/lmc_132.pdf`, [Online; accessed 31-Mar-2013].

[BV09] A. Breskin and R. Voss, editors. *The CERN Large Hadron Collider: Accelerator and Experiments*, volume 2: CMS, LHCb, LHCf and TOTEM. CERN, Geneva, 2009.

[BW10] H. Burkhardt and S. White. High-β^* Optics for the LHC. Technical Report LHC-Project-Note-431, CERN, Geneva, Jun. 2010.

[CAS06] *Proceedings of the CERN Accelerator School 2003, Zeuthen, Germany*, CERN, Geneva, 2006.

[CER09] CERN. LHC sets new world record, CERN Press Release. `http://press.web.cern.ch/press-releases/2009/11/lhc-sets-new-world-record`, 2009. [Online; accessed 26-Oct-2012].

[CER11] CERN. LHC Schedule 2012. `https://espace.cern.ch/be-dep/BEDepartmentalDocuments/BE/LHC_Schedule_2012.pdf`, 2011. [Online; accessed 15-Jan-2013].

[CER12] CERN. LHC physics data taking gets underway at new record collision energy of 8 TeV, CERN Press Release. `http://press.web.cern.ch/press-releases/2012/04/lhc-physics-data-taking-gets-underway-new-record-collision-energy-8tev`, 2012. [Online; accessed 15-Jan-2013].

[Cha99] A. Chao. *Handbook of accelerator physics and engineering*. World Scientific Publishing Company Incorporated, 1999.

[Cou99] CERN Courier. Probing the pomeron. `http://cerncourier.com/cws/article/cern/27985`, 1999. [Online; accessed 08-Feb-2012].

[Cou08] CERN Courier. TOTEM and LHCf: Roman pots for the LHC. `http://cerncourier.com/cws/article/cern/35883`, 2008. [Online; accessed 26-Oct-2012].

[D+02] S. Donnachie *et al. Pomeron physics and QCD*, volume 19. Cambridge University Press, 2002.

[Dei12] M. Deile, 2012. Private Communication.

[Fab08] C.W. Fabjan. ALICE at the LHC: getting ready for physics. *J. Phys. G: Nucl. Part. Phys.*, 35(10):104038, 2008.

[Fer09]   Fermilab.   Fermilab   webpage.   `http://www.fnal.gov/pub/tevatron/`
`tevatron-operation.html`, 2009. [Online; accessed 15-Jan-2013].

[Fit12]   M. Fitterer, 2012. Unpublished Mathematica Notebook.

[For12]   K. Foraz.   LS1 general planning and strategy for the LHC, LHC injectors.   In
Proceedings of Chamonix 2012 workshop on LHC Performance. CERN, 2012.

[Gio12]   M. Giovannozzi, 2012. Private Communication.

[GM10]   C. Gerthsen and D. Meschede. *Gerthsen Physik.* Springer Verlag, Berlin, 2010.

[Hel10]   M. Heller. *Mesure de la luminosité absolue et de la section efficace totale proton-
proton dans l'expérience ATLAS au LHC. oai:cds.cern.ch:1305411.*   PhD thesis,
Université Paris-Sud 11, Orsay, 2010.

[Her12]   W. Herr, 2012. Private Communication.

[Hin08]   F. Hinterberger. *Physik der Teilchenbeschleuniger und Ionenoptik.* Springer Verlag,
Berlin Heidelberg, 2008.

[HK08]   W. Herr and D. I. Kaltchev. Effect of phase advance between interaction points in
the LHC on the beam-beam interaction. Technical Report LHC-Project-Report-1082,
CERN, Geneva, May 2008.

[Hol13]   B. Holzer, 2013. Private Communication.

[HS13]   P. D. Hermes and R. Schicker. Tagging of very forward protons in ALICE. Technical
Report CERN-ATS-2013-001, CERN, Geneva, Jan 2013.

[JO97]   J.B. Jeanneret and R. Ostojic. Geometrical acceptance in LHC Version 5.0. Technical
Report LHC-Project-Note-11, CERN, Geneva, Sep. 1997.

[Jow97]   J.M. Jowett. Basic MAD Tables in Mathematica. (CERN-SL Note/97-55 (AP)), 1997.

[Jow13]   J.M. Jowett. LHC Status Report. Run 1 - The Final Act. Talk at LHC experiments
comittee, 13/03/2013, 2013.

[JR96]   J.B. Jeanneret and T. Risselada. Geometrical aperture in LHC at injection. Technical
Report LHC-Project-Note-66, CERN, Geneva, Sep. 1996.

[K+11]   V. Kain *et al.* Transverse emittance preservation through the LHC cycle. Technical
Report CERN-ATS-2011-056, Sep. 2011.

[Kul01] S. Kullander. Accelerators and Nobel Laureates. `http://www.nobelprize.org/nobel_prizes/physics/articles/kullander/`, 2001. [Online; accessed 26-Oct-2012].

[L3 90] L3 Collaboration. The Construction of the L3 Experiment. *Nucl.Instrum.Meth.*, A289:35–102, 1990.

[LA05] T. Ludlam and S. Aronson. Hunting the quark gluon plasma. (BNL -73847-2005), 2005.

[Lef08] C. Lefèvre. The CERN accelerator complex. Complexe des accélérateurs du CERN. Available on CERN Document Server, Dec. 2008.

[LHC13] LHC Experiments. `http://public.web.cern.ch/public/en/lhc/lhcf-en.html`, 2013. [Online; accessed 08-Jan-2013].

[LM93] P. Lefèvre and D. Möhl. A low energy accumulation ring of ions for LHC (a feasibility study). Technical Report CERN-PS-93-62. CERN-LHC-Note-259, CERN, Geneva, Dec. 1993.

[MADa] MAD-X Homepage. MADX webpage. `http://madx.web.cern.ch/madx`. [Online; accessed 15-May-2012].

[MADb] MAD-X User's Guide. `http://madx.web.cern.ch/madx/madX/doc/usrguide/uguide.html`. [Online; accessed 15-Mar-2013].

[Mor01] A. Morsch. ALICE Luminosity and Beam Requirements. Technical report, ALICE-INT-2001-10, 2001.

[Par10] Particle Data Group. Review of Particle Physics, 2010-2011. Review of Particle Properties. *J. Phys. G*, 37(7A):075021, 2010.

[Rie12] W. Riegler. Beampipe, schedule, integration. Talk at ALICE Technical Board, 16/02/2012, 2012.

[RKL75] D.M. Ritchie, B.W. Kernighan, and M.E. Lesk. *The C programming language*. Bell Laboratories, 1975.

[S$^+$13] R. Schicker *et al.* Spectroscopy of Charmonia States in ALICE, 2013. Unpublished Note.

[Sch05] F. Schmidt. Mad-PTC Integration. In *Prodeedings of the Particle Accelerator Conference, 2005*, pages 1272–1274. IEEE, 2005.

[Sch12] R. Schicker, 2012. Private Communication.

[Sch13] R. Schicker. Tagging of forward protons and Pb-ions in ALICE. Talk at ALICE Upgrade Forum, Jan. 2013.

[Trä07] F. Träger. *Springer Handbook of Lasers and Optics.* Springer Verlag, Berlin Heidelberg, 2007.

[Tro04] M. Trott. *The Mathematica GuideBook for Programming.* Springer, 2004.

[TSC11] M. Trzebinski, R. Staszewski, and J. Chwastowski. LHC High β^* Runs: Transport and Unfolding Methods. *arXiv preprint arXiv:1107.2064*, 2011.

[Tur95] *CERN Accelerator School : 5th Advanced Accelerator Physics Course.* CERN, Geneva, 1995.

[VJ12] R. Versteegen and J. M. Jowett. Optics, crossing angle and aperture in p-Pb physics conditions in the LHC. Technical Report ATS-Note-2012-051 PERF, Jun 2012.

[Wie99] H. Wiedemann. *Particle accelerator physics I: basic principles and linear beam dynamics*, volume 1. Springer Verlag, 1999.

Danksagung

Selbstständigkeitserklärung

Hiermit erkläre ich, diese Arbeit selbstständig verfasst und keine anderen als die angegebenen Hilfsmittel benutzt zu haben.

Pascal Dominik Hermes